Numerical simulations of boundary layer transition over a concave surface : application to the design of Savonius-style vertical axis wind turbines

Margio González Méndez

Normandie Université

THÈSE

Pour obtenir le titre de
Docteur

Spécialité : *Mécanique des fluides*

Préparée au sein de l'Institut National des Sciences Appliquées (INSA) Rouen-Normandie

Simulations numériques de la transition de la couche limite sur une surface concave: Application à la conception des éoliennes à axe vertical de type Savonius

Présentée et soutenue par
Margio MÉNDEZ GONZÁLEZ

Thèse soutenue publiquement le 29 juin 2020 devant le jury composé de		
Arnab CHAUDHURI	Professeur, Université Métropolitaine d'Oslo, Norvège	Rapporteur
Ashwin CHINNAYYA	Professeur, ISAE-ENSMA, Institut P', France	Rapporteur
Antoine DUCOIN	Maître de Conférences (HDR), École Centrale de Nantes, France	Examinateur
Jorge PEIXINHO	Chargé de Recherches, PIMM, Arts et Metiers ParisTech, France	Examinateur
Luminita DANAILA	Professeur, Université de Rouen-Normandie, France	Examinateur
Olivier THOMINE	Ingénieur-Docteur, Centre de Recherche CEA Saclay, France	Membre Invité
Mostafa S. SHADLOO	Maître de Conférences, INSA de Rouen-Normandie, France	Co-encadrant
Abdellah HADJADJ	Professeur, INSA de Rouen-Normandie, France	Directeur de thèse

Thèse dirigée par Prof. Abdellah HADJADJ
Co-encadrée par Dr. Mostafa SAFDARI SHADLOO
Laboratoire CORIA UMR – 6614, CNRS

INSA ROUEN NORMANDIE

coria UMR 6614

ED PSIME

CONACYT

Normandie Université

DISSERTATION

Submitted in the partial fulfillment for the award of Doctor of Philosophy

Specialized in : *Fluid Mechanics*

For the work performed at the National Institute of Applied Sciences (INSA) Rouen-Normandie

Numerical simulations of boundary layer transition over a concave surface: Application to the design of Savonius-style vertical axis wind turbines

Presented and defended by

Margio MÉNDEZ GONZÁLEZ

Thesis defended publicly on the 29th June 2020 in front of the jury composed of		
Arnab CHAUDHURI	Professor, Oslo Metropolitan University, Norway	Reporter
Ashwin CHINNAYYA	Professor, ISAE-ENSMA, Institute P', France	Reporter
Antoine DUCOIN	Associate Professor (HDR), École Centrale de Nantes, France	Examiner
Jorge PEIXINHO	Research Scientist, PIMM, Arts et Metiers ParisTech, France	Examiner
Luminita DANAILA	Professor, University of Rouen-Normandie, France	Examiner
Olivier THOMINE	Engineer-Doctor, Research Center CEA Saclay, France	Invited Member
Mostafa S. SHADLOO	Associate Professor, INSA de Rouen-Normandie, France	Co-supervisor
Abdellah HADJADJ	Professor, INSA de Rouen-Normandie, France	Thesis Director

Thesis supervised by Prof. Abdellah HADJADJ
Co-supervised by Dr. Mostafa SAFDARI SHADLOO
CORIA Laboratory UMR – 6614, CNRS

INSA ROUEN NORMANDIE

CORIA UMR 6614

ED PSIME

CONACYT

Acknowledgements

I would like to thank my supervisors, Prof. Abdellah HADJADJ and Dr. Mostafa S. SHADLOO, for giving me the opportunity to perform my PhD studies in their research team and to work on this interesting research topic of boundary layer transition. I am also grateful to the reviewers of my thesis Prof. Arnab CHAUDHURI and Prof. Ashwin CHINNAYYA, and also to the jury members Dr. Antoine DUCOIN, Dr. Jorge PEIXINHO, Prof. Luminita DANAILA and Dr. Olivier THOMINE for investing their valuable time in evaluating this manuscript.

I would also like to thank my parents and my brother because they have always been there for me. They have supported me, encouraged me and cared about me throughout all these years. Therefore, I have to say that this accomplishment could not have been achieved without their moral and emotional support.

Furthermore, I would like to acknowledge the research and academic institutions who have helped to perform this doctoral study. The funding resources provided by the CONACYT-SENER sectoral fund for performing this research work are acknowledged. Furthermore, the access to High Performance Computing resources for carrying out the needed numerical simulations for this study, which was granted by the super-computing center CRIANN (Centre Régional Informatique et d'Applications Numériques de Normandie), is also acknowledged. Moreover, the research institute CORIA and the university INSA Rouen-Normandie are acknowledged for providing me with the necessary facilities to perform these research studies.

Abstract

English

Direct numerical simulations (DNS) are computed in order to study the complete laminar-to-turbulent transition process of a boundary layer developing over a concave surface. It is found that the flow passing through such geometry is prone to develop centrifugal instabilities in the form of Görtler vortices. Transition is triggered by means of wall-roughness elements that are also utilized to preset the spanwise wavelength of the Görtler vortices. The different regions encountered in the transition process, i.e. linear, nonlinear, transition, and fully turbulent, are identified and characterized. Primary and secondary (varicose and sinuous) instabilities are identified and analyzed as well. Parametric studies showing the effect of several physical parameters (radius of curvature, the vortices wavelength, the perturbation amplitude and streamwise location, and the wall-roughness perturbation geometry) on the transition starting point are presented. Furthermore, thermal analyses are conducted in order to study the modification of the thermal boundary layer due to the Görtler vortices swirl motion. The streamwise evolution of the surface heat transfer is investigated finding that it is considerably enhanced in the non-linear region surpassing the turbulence-region values. It is also found that the Reynolds analogy between streamwise-momentum and heat transfer is followed throughout the whole transition process.

Français

Des simulations numériques directes (DNS) sont calculées afin d'étudier le processus complet de transition laminaire-turbulent d'une couche limite qui se développe sur une surface concave. On constate que l'écoulement traversant une telle géométrie est susceptible de développer des instabilités centrifuges sous forme de tourbillons de Görtler. La transition est déclenchée au moyen d'éléments de rugosité de paroi qui sont également utilisés pour prédéfinir la longueur d'onde transversale des tourbillons de Gortler. Les différentes régions rencontrées dans le processus de transition, c'est-à-dire linéaire, non-linéaire, transition et completement turbulente, sont identifiées et caractérisées. Les instabilités primaires et secondaires (sinueux et variqueux) sont également identifiées et analysées. Des études paramétriques montrant l'effet de plusieurs paramètres physiques (le rayon de courbure, la longueur d'onde des tourbillons, l'amplitude et la localisation de la perturbation, et la géométrie des eléments de rugosité de paroi) sur le point de départ de la transition son presentées. De plus, des analyses thermiques sont menées afin d'étudier la modification de la couche limite thermique produite par le mouvement rotatif des tourbillons de Görtler. L'évolution du transfert thermique de la surface est étudiée et on constate qu'il est considérablement augmenté dans la région non-linéaire dépassant les valeurs de la région turbulente. On constate également que l'analogie de Reynolds entre la quantité de mouvement dans le sens de l'écoulement et le transfert de chaleur est suivie tout au long du processus de transition.

Contents

List of Symbols and Abbreviations

English Symbols

$\mathbf{A}$	SEM global stiffness matrix
A	Galerkin method stiffness matrix
B	Constant on the log-wall region formula
$\mathbf{C}$	SEM global convective operator matrix
C	Galerkin method convective operator matrix
C_f	Skin friction coefficient
C_p	Pressure coefficient
c	Convection velocity
c_p	Specific heat at constant pressure
CFL	Courant number
D_N	SEM differentiation matrix
E	Number of spectral elements
F	Dimensionless frequency
$\mathbf{f}$	Body forces vector
G_r	Grashof number
G_θ	Görtler number
$G_{\theta_{cr}}$	Critical Görtler number
H	Boundary layer shape factor
H_0^1	Sobolev space
H_o	Helmholtz operator
h	Wall-roughness element height
h_e	Length of a 1D SEM element
h_{conv}	Convection heat transfer coefficient
K	Vortex amplitude parameter
k	Turbulence kinetic energy
k_t	Time integration scheme order
k_{th}	Thermal conductivity
L_N	Legendre polynomial of order N
L_z	Computational domain spanwise length
L_η	Computational domain streamwise length
L_ξ	Computational domain wall-normal length
$\mathbf{M}$	SEM global mass matrix

M	Galerkin method mass matrix
N	Polynomial order of the SEM simulation
N_t	Total number of GLL nodal points
Nu	Nusselt number
n_z	Number of spectral elements in the spanwise direction
n_η	Number of spectral elements in the wall-normal direction
n_ξ	Number of spectral elements in the streamwise direction
p	Pressure
p_∞	Free-stream static pressure
p_0	Free-stream stagnation pressure
Pr	Prandtl number
Q_w	Heat transfer from the wall
q_{vol}	Volumetric heat sources
R	Radius of curvature
R_i	Computational domain inner radius
r	Radial coordinate for a curved geometry
Re	Reynolds number
Re_{cr}	Critical Reynolds number
Re_x	Reynolds number based on x
$Re_{x_{cr}}$	Critical Reynolds number based on x
$Re_{\delta^*}^{rgh}$	Reynolds number based on δ^* at the wall-roughness streamwise location
Re_θ	Reynolds number based on θ
Re_ξ	Reynolds number based on ξ
Re_ξ^{rgh}	Streamwise location, Re_ξ, of the wall-roughness perturbation
Re_τ	Reynolds number based on u_τ
Sc	Schmidt number
Sh	Sherwood number
St	Stanton number
T	Temperature
$\overline{T}$	Mean temperature
T_∞	Free-stream temperature
T_w	Wall temperature
t	Time
Tu	Free-stream turbulence intensity
Tu_{max}	Wall-normal maximum value of Tu
$\mathbf{U}$	Instantaneous velocity vector

U	Instantaneous streamwise velocity
$\overline{U}$	Mean streamwise velocity
$\overline{\mathbf{U}}$	Mean velocity vector
U^+	Streamwise velocity nondimensionalized with u_τ
U_∞	Free-stream velocity
$\mathbf{U_b}$	Basic flow velocity vector
U_b	Basic flow streamwise velocity
$\mathbf{u}$	Perturbation velocity vector
u	Streamwise perturbation velocity
$\widehat{u}$	Primary instability modes amplitude
$\mathbf{u}'$	Velocity temporal fluctuation vector
$\mathbf{u_{rms}^{max}}$	Wall-normal maximum of the rms in z of $\mathbf{u}$
u_{rms}^{max}	Wall-normal maximum of the rms in z of u
u'	Streamwise velocity temporal fluctuation
u_τ	Wall-friction velocity
V	Instantaneous wall-normal velocity
$\overline{V}$	Mean wall-normal velocity
V_b	Basic flow wall-normal velocity
v	Wall-normal perturbation velocity
v'	Wall-normal velocity temporal fluctuation
v_{rms}^{max}	Wall-normal maximum of the rms in z of v
v_f	Variational formulation test function
W	Instantaneous spanwise velocity
$\overline{W}$	Mean spanwise velocity
W_b	Basic flow spanwise velocity
w	Spanwise perturbation velocity
w'	Spanwise velocity temporal fluctuation
w_{rms}^{max}	Wall-normal maximum of the rms in z of w
x	Streamwise coordinate
x_r	Streamwise coordinate for the SEM reference element
y	Wall-normal coordinate
y^+	Wall-normal coordinate in wall-units
y_r	Wall-normal coordinate for the SEM reference element
z	Spanwise coordinate
z^+	Spanwise coordinate in wall-units
z_r	Spanwise coordinate for the SEM reference element

Greek Symbols

α	Görtler vortices spanwise wavenumber
α_{th}	Thermal diffusivity
β	Primary instabilities spatial growth rate
β_{Tu}	Secondary instabilities growth rate
Γ	Circulation
γ	Spanwise spatial frequencies of the primary instability modes
δ	Boundary layer thickness
δ^*	Boundary layer displacement thickness
$\delta_{Blasius}$	Theoretical Blasius boundary layer thickness
δ_{ij}	Identity matrix
δ_{in}	Boundary layer thickness at the domain inlet
δ_{th}	Thermal boundary layer thickness
$\delta_{th,Pr=1}$	Theoretical thermal boundary layer thickness for a fluid with $Pr = 1$
η	Wall-normal coordinate for a concave surface
η^+	Wall-normal coordinate in wall-units for a concave surface
Θ^+	Temperature in wall units
θ	Boundary layer momentum thickness
θ_{th}	Non-dimensional temperature
$\overline{\theta_{th}}$	Mean non-dimensional temperature
θ'_{th}	Non-dimensional temperature temporal fluctuation
θ_τ	Friction temperature
κ	Von Kármán constant
Λ	Görtler vortices nondimensional spanwise wavelength
λ	Görtler vortices spanwise wavelength
λ_2	Lambda-2 vortex criterion
λ_z	Λ-shaped vortices spanwise wavelength on a flat plate transition process
μ	Dynamic viscosity
ν	Kinematic viscosity
ξ	Streamwise coordinate for a concave surface
ξ^+	Streamwise coordinate in wall-units for a concave surface
ρ	Density
ρ_k	Gauss quadrature weight
τ	Viscous stress tensor
τ_w	Wall-shear stresses
$\overline{\tau}_w$	Mean wall-shear stresses

Φ	Computational domain arc length
ϕ	SEM basis function
ϕ_{loc}	Angular location in the computational domain
Ω	SEM global domain
Ω^e	SEM local domain
$\hat{\Omega}$	SEM reference element domain
ω_ξ	Vorticity component in the streamwise direction

Abbreviations

1D	One-Dimensional
2D	Two-Dimensional
3D	Three-Dimensional
BDF	Backward Differentiation Scheme
CEA	Commissariat à l'Énergie Atomique et aux Énergies Alternatives
CFD	Computational Fluid Dynamics
CRIANN	Centre Régional Informatique et d'Applications Numériques de Normandie
CORIA	Complexe de Recherche Interprofessionnel en Aérothermochimie
CONACYT	National Council of Science and Technology of Mexico
DNS	Direct Numerical Simulation
EXT	Extrapolation Scheme
FEM	Finite Element Method
GL	Gauss-Lobatto
GLL	Gauss-Lobatto-Legendre
SEM	Finite Element Method
IMEX	Implicit-Explicit Method
INSA	Institut National des Sciences Appliquées
LES	Large Eddy Simulation
LST	Linear Stability Theory
MPI	Message Passage Interface
PDE	Partial Differential Equation
PIMM	Procédés et Ingénierie en Mécanique et Matériaux
PSE	Parabolized Stability Equation
rms	Root-mean-squared
SEGOB	Secretariat of the Interior of Mexico
SEM	Spectral Element Method
SENER	Secretariat of Energy of Mexico
TKE	Turbulence Kinetic Energy

TS	Tollmien-Schlichting
URANS	Unsteady Reynolds-Averaged Navier-Stokes
VAWT	Vertical Axis Wind Turbine
WKB	Wentzel-Kramers-Brillouin

List of Figures

List of Tables

List of Publications

Peer-reviewed journals

1. **Méndez M.**, Shadloo M. S. & Hadjadj A. (2020), Heat-transfer analysis of a transitional boundary layer over a concave surface with Görtler vortices by means of direct numerical simulations, *Physics of Fluids (accepted with minor revisions).*

2. **Méndez M.**, Shadloo M. S., Hadjadj A. & Ducoin A. (2018), Boundary layer transition over a concave surface caused by centrifugal instabilities, *Computers and Fluids,* ***171****, 135-153.*

International conferences

1. **Méndez M.**, (2018), Boundary layer transition over a concave surface through DNS simulations, 7th CONACYT Scholars Symposium in Europe, 11-13 April 2018, Strasbourg, France.

2. **Méndez M.**, Shadloo M. S., Hadjadj A. & Ducoin A. (2017), Boundary-layer transition over concave surfaces caused by centrifugal forces, Euromech Symposium 591: 3-D Instability mechanisms in transitional and turbulent flows, 18-20 September 2017, Bari, Italy.

Chapter 1
Introduction

1.1 General context

This research project was funded by the Mexican CONACYT (National Council of Science and Technology) - SENER (Secretariat of Energy) sectoral fund of sustainable energy. The goal of this joint effort being the training of highly specialized human resources for facing the coming challenges of the energetic sector in Mexico. One of them is the sustainable development of the Mexican society that has to take care of the environment for the future generations. Under that context, Mexico has the objective of diversifying its energy sources in order to produce more electricity from clean and renewable sources. All these objectives are part of Mexico's Energy Reform of 2013 (SEGOB 2013).

This research study, apart from training human resources at the doctoral level, has also the objective of understanding the flow behavior when passing over a concave surface. From the renewable energetic sector point of view, this topic is quite relevant because this type of geometry can be found on the blades of the Savonius-style Vertical Axial Wind Turbines (VAWT), which have found some emerging interest, especially for off-grid applications, due to their technical and economic feasibility (Bortolini et al. 2014, Grieser et al. 2015). Consequently, the understanding of the flow development over such geometry, with the aid of a proper computational methodology, can help to improve their design, aerodynamic performance and energy conversion rate (Roy & Saha 2013).

This project has, therefore, the main objective of studying, analyzing and characterizing the complete laminar-to-turbulent transition process of a boundary layer passing over a concave surface by means of high-fidelity Direct Numerical Simulations (DNS); as it has been shown that these type of costly Computational Fluid Dynamics (CFD) simulations of basic geometries (flow passing over a concave surface) are required for completely capturing the transition phenomenon and computing its physical impact on the aerodynamic performance parameters of a Savonius-style VAWT blade (Ducoin et al. 2017). Subsequently, the numerical simulations were computed on the research super-computing center CRIANN (Centre Régional Informatique et d'Applications Numériques de Normandie) since this research study demands high-level of computational performance.

1.2 Motivation

The laminar-to-turbulent transition process of a boundary layer has always been a complex phenomenon of fundamental importance in the field of Fluid Mechanics. As the boundary layer evolves over a surface, the flow changes from a laminar state, that is characterized by

a smooth movement of well-ordered layers alongside each other, to a turbulent state, where this orderly flow is replaced by highly chaotic variations in the flow field properties (velocity and pressure) and strong mixing effects are noticed.

However, the transitional phase, along with the relevant parameters that have an effect on it, has not been completely understood and characterized. Moreover, compared to a flat plate, that has been largely studied, the transition process of a boundary layer developing over a concave surface occurs in a completely different manner. Over a concave wall, the curved motion of the flow is naturally unstable (Rayleigh 1917). And, it is highly susceptible to develop centrifugal instabilities when perturbations are introduced into the boundary layer (e.g. wall-roughness, free-stream turbulence intensity, etc.). These centrifugal instabilities, that initiate the transition process, have the from of steady streamwise-oriented counter-rotating vortex pairs and are known as Görtler vortices (Görtler 1940).

This transitional scenario is therefore quite particular for a concave surface and its understanding and characterization is utterly relevant for the numerous engineering applications where it can be found. Apart from the already mentioned wind turbines (Ducoin et al. 2016, 2017), this transition type can also be found in several engineering devices, such as turbomachinery blades (Han & Cox 1982, Wang et al. 2005), airfoils (Mangalam et al. 1985, Dagenhart & Mangalam 1986) and nozzles (Beckwith & Holley 1981, Chen et al. 1993). Furthermore, the presence of Görtler vortices significantly modifies and enhances the surface heat transfer, making their characterization relevant for thermal applications such as heat exchangers (McCormack et al. 1970) or jet engines with extremely hot conditions (Peerhossaini & Wesfreid 1988*a*, Toe et al. 2002). Moreover, the increase of wall-shear stresses produced by the Görtler vortices is capable of provoking erosion on the surface over which they develop (Kieffer & Sturtevant 1988, Hopfinger et al. 2004).

On this context, the main motivation of this project comes from the fact that the outcome of these research studies can help to better understand and clarify one of the most complex questions in the field of Fluid Mechanics, which is how and why the flow transitions from a laminar to a turbulent state. This can be done by characterizing the boundary layer over its different transitional phases and by analyzing the parameters that play a role on the triggering of the phenomenon. Moreover, the obtained results can also help to improve the performance and to better design several engineering devices that are utilized mainly in the renewable energies and aerospace sectors. Furthermore, the outcome results of the present investigation, performed using high-fidelity DNS, are expected to be considered as a benchmark test case for future studies and for turbulence model development.

1.3 Basic notes of the boundary layer

The concept of **boundary layer** was first introduced by Ludwig Prandtl in 1904 (Prandtl 1904). He suggested to divide a viscous flow into two regions; one thin region adjacent to the solid boundaries, where the viscosity effects are experienced by the flow, and another

one covering the rest of the flow, where the viscosity effects are negligible and the fluid can be considered as inviscid. Hence, the boundary layer is the confined region in between the wall and the inviscid outer free-stream flow. Inside it, the flow experiences a steep gradient of shearing stresses that is caused by a rapid change of the fluid velocity, in the wall-normal direction, that goes from zero at the wall (no-slip condition) up to the free-stream velocity at the boundary layer edge.

The boundary layer exists whether the flow is laminar or turbulent. On a laminar state, the boundary layer is formed by layers of fluid that slide over each other and the particles travel without crossing to the adjacent layers. On the other hand, on the turbulent case, the fluid particles move parallel and perpendicular to the flow direction and they do cross to the adjacent layers in a seemingly random manner. Consequently, due to the different degrees of fluid mixing in laminar and turbulent flows, the properties, characteristics and, therefore, the shape (velocity distribution) of the two boundary layers are different. The main descriptive characteristics of the boundary layer for both cases are defined in the following subsections.

1.3.1 Laminar boundary layer

For the **laminar boundary layer** over a flat plate, it was Heinrich Blasius (Blasius 1907) who analytically solved the Prandtl boundary layer equations and found a self-similar solution for the velocity profile of the laminar boundary layer, i.e., regardless of the streamwise position, x, the velocity profile will always keep the same velocity distribution. The **velocity profiles** of the streamwise and wall-normal velocity components (U and V, respectively) are shown in Figure 1.1. On the presented charts, the wall-normal space coordinate, y, is normalized with the boundary layer thickness, δ. The velocity U is normalized with the free-stream velocity, U_∞, whereas the velocity V is normalized with the product of U_∞ and the Reynolds number based on x, Re_x, to the power of $-1/2$.

This dimensionless number, Re_x, firstly proposed by Osborne Reynolds (Reynolds 1883), relates the inertial to the viscous forces and is used to assure a mechanical similarity of two flows passing through the same geometry. It is also useful for determining the streamwise location on the analyzed surface and is defined as:

$$Re_x = \frac{U_\infty x}{\nu}, \tag{1.1}$$

where ν is the fluid kinematic viscosity.

The boundary layer extent in the wall-normal direction, i.e. the **boundary layer thickness**, δ, is normally measured up to the point at which the streamwise velocity component has reached 99% of the outer free-stream velocity. δ increases during the development of the flow and, for the Blasius laminar case, follows the law:

$$\delta = \frac{5x}{\sqrt{Re_x}}. \tag{1.2}$$

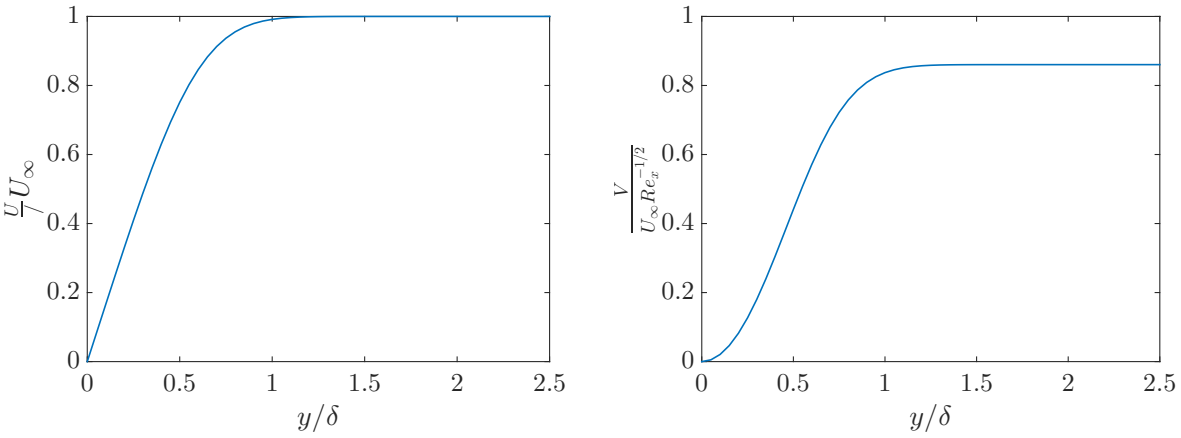

(a) (b)

Figure 1.1: Blasius velocity profiles. a) Streamwise component. b) Wall-normal component.

The viscosity reduces the mass flow rate of the flow passing next to a solid surface. In order to quantify this loss, the boundary layer **displacement thickness**, δ^*, can be used. It measures the distance by which the surface would have to be moved upward in its normal direction so that an inviscid flow with velocity U_∞ would have the same mass flow rate as the one that occurs through the viscous boundary layer flow. For an incompressible flow, it can be computed using the following integral over the wall-normal direction:

$$\delta^* = \int_0^\infty \left(1 - \frac{U(y)}{U_\infty}\right) dy. \tag{1.3}$$

The displacement thickness increases as the boundary layer evolves over the surface. For the flat plate laminar case, its value, according to its streamwise position, is given by:

$$\delta^* = \frac{1.721x}{\sqrt{Re_x}}. \tag{1.4}$$

Another relevant parameter is the boundary layer **momentum thickness**, θ. The momentum thickness serves to quantify the reduction of momentum on the boundary layer relative to that of a inviscid flow. In other words, it is the distance by which a surface would have to be moved upward in the wall-normal direction in an inviscid flow of velocity U_∞ so that it can have the same momentum as a real viscous flow. For an incompressible flow, it is computed with the following integral:

$$\theta = \int_0^\infty \frac{U(y)}{U_\infty}\left(1 - \frac{U(y)}{U_\infty}\right) dy. \tag{1.5}$$

For a laminar incompressible flow over a flat plate, the evolution of the boundary layer

momentum thickness is given by:

$$\theta = \frac{0.664x}{\sqrt{Re_x}}. \tag{1.6}$$

Another useful parameter is the boundary layer **shape factor**, H. It is used to determine the nature of the flow and its streamwise sudden change can help to determine the transition starting point or, rather, the transition region. It is obtained by computing the ratio of the two previous lengths:

$$H = \frac{\delta^*}{\theta}. \tag{1.7}$$

For a laminar boundary layer, it normally has the value of $H = 2.59$.

Next, the tangential friction forces per unit area exerted by the flow over the wall can be quantified with the **wall shear stress** parameter, τ_w. Its magnitude is proportional to the velocity gradient next to wall and it can be computed with the Newton's law of friction:

$$\tau_w(x) = \mu\left(\frac{\partial U}{\partial y}\right)_w. \tag{1.8}$$

where μ is the fluid dynamic viscosity. τ_w can also be quantified in a non-dimensional way with the **skin friction coefficient**, C_f, which is equal to:

$$C_f = \frac{\tau_w(x)}{\frac{1}{2}\rho U_\infty^2}, \tag{1.9}$$

where ρ is the fluid density.

For a laminar boundary layer over a flat plate, the skin friction coefficient evolves according to the following law:

$$C_f = \frac{0.664}{\sqrt{Re_x}}. \tag{1.10}$$

1.3.2 Turbulent boundary layer

Now that the main boundary layer parameters have been defined for the laminar case, they are going to be introduced for the **turbulent boundary layer**. For the turbulent case, a more intense mixing is responsible for steeper velocity gradients that will produce higher wall-shear stresses. Thus, the velocity profile is expected to be different from the laminar one. Besides, unlike the laminar case, the turbulent boundary layer is naturally unsteady and, therefore, time-averaged quantities, instead of instantaneous ones, are normally reported. Hence, we can introduce:

$$\mathbf{U} = \overline{\mathbf{U}} + \mathbf{u}', \tag{1.11}$$

where the instantaneous velocity field, $\mathbf{U}$, is decomposed in its time-averaged part, indicated by an overline, $\overline{\mathbf{U}}$, and its temporal fluctuation, indicated by the prime symbol, $\mathbf{u}'$.

Moreover, the turbulent boundary layer is normally analyzed using viscous scales (or wall-units). To that end, the characteristic velocity for turbulent flows at a given wall shear stress, i.e. the **wall friction velocity**, u_τ, is introduced:

$$u_\tau = \sqrt{\frac{\overline{\tau}_w(x)}{\rho}}. \tag{1.12}$$

With u_τ, the coordinates in wall-units can also be introduced. Thus, the wall-normal coordinate is given by:

$$y^+ = \frac{y u_\tau}{\nu}. \tag{1.13}$$

The velocity can also be non-dimensionalized with the aid of the friction velocity. The streamwise component is given by:

$$U^+ = \frac{\overline{U}}{u_\tau}. \tag{1.14}$$

It was Ludwig Prandtl (Prandtl 1925) who postulated that the **velocity profile** inside the turbulent boundary layer is determined by the viscous scales and that U^+ depends solely on y^+. It is important to remark that this velocity distribution, $U^+ = f(y^+)$, is universal in the sense that, for large Reynolds numbers, it can be found in almost all turbulent flows; as it has been largely verified experimentally and numerically for channel flows, pipe flows and flows over flat plates (Pope 2000).

A typical velocity profile of a turbulent boundary layer is shown in Figure 1.2. This presented profile was obtained experimentally, and also replicated numerically, by Schlatter et al. (2009) at a Reynolds number based on the momentum thickness of $Re_\theta = 2400$. Several regions can be differentiated from the velocity profile that are in accordance with the *universal law of the wall*. They are summarized in Table 1.1.

Region	Location	Properties
Viscous sublayer	$y^+ \leq 5$	$U^+ = y^+$
Buffer layer	$5 < y^+ \leq 30$	Region between the two other regions
Log-law region	$y^+ > 30$	$U^+ = \kappa^{-1} \log y^+ + B$

Table 1.1: Wall regions of the turbulent boundary layer.

The entire turbulent flow field can be divided into two regions; a turbulence free region that is outside the boundary layer (the free-stream) and the boundary layer itself that is characterized by random fluctuations of the flow field properties. At the same time, the turbulent boundary layer can also be divided into several regions.

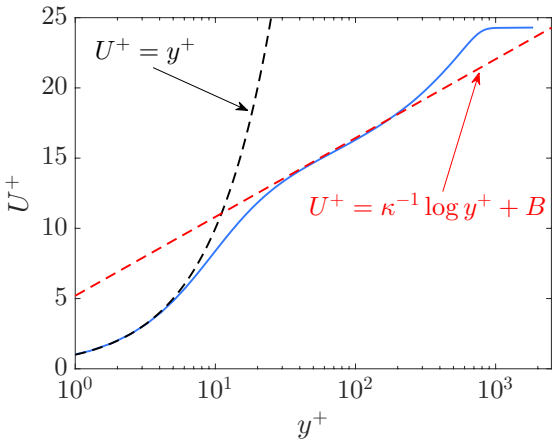

Figure 1.2: Velocity profile of a turbulent boundary layer in viscous units. (——) $U^+ = f(y^+)$ from Schlatter et al. (2009) at $Re_\theta = 2400$, (- - -) $U^+ = y^+$ and (- - -) $U^+ = \kappa^{-1} \log y^+ + B$; with $\kappa = 0.41$ and $B = 5.2$.

The region that is adjacent to the wall is called the *viscous sublayer* and it is the part of the boundary layer where the viscosity effects can be noticed. It is extended from the wall, $y^+ = 0$, up to $y^+ \leq 5$ and the streamwise velocity follows the law $U^+ = y^+$. Next, there is a transition region between the viscosity-dominated flow and the turbulence-dominated flow. It goes from $y^+ > 5$ to $y^+ \leq 30$ and it is called the *buffer region*.

Finally, from $y^+ > 30$, there is the *log-law region* where the effects of viscosity can be neglected and the flow is highly dominated by turbulent chaotic motion. It was Theodore von Kármán (von Kármán 1930) who first determined that, inside this region, the velocity follows the logarithmic law $U^+ = \kappa^{-1} \log y^+ + B$, where κ is the von Kármán constant and B is also a constant. This constants present some variations in the literature but they are normally within 5% of $\kappa = 0.41$ and $B = 5.2$ (Pope 2000).

Once that the turbulent boundary layer structure has been described, the different parameters that characterize it can be defined. The integral parameters can be defined with *Prandtl's one-seventh power law relationships* (Prandtl 1927) that have been proved to be in good agreement with turbulent flat plate experimental data (White 1991). Hence, the **boundary layer thickness**, **displacement thickness** and **momentum thickness** streamwise evolution are respectively given by:

$$\delta = \frac{0.16x}{Re_x^{1/7}}, \tag{1.15}$$

$$\delta^* = \frac{0.02x}{Re_x^{1/7}}, \tag{1.16}$$

and

$$\theta = \frac{0.016x}{Re_x^{1/7}}. \tag{1.17}$$

As seen, the turbulent boundary layer grows at a faster rate compared to the laminar case. Besides, with these relations, it is also possible to define a **shape factor** for the turbulent flat plate which has the value of $H = 1.25$.

Regarding the **wall-shear stresses**, they are also considerable higher due to the intense mixing inside the boundary layer that causes a greater velocity gradient next to the wall. Their streamwise evolution can also be obtained from Prandtl's relationships:

$$C_f = \frac{0.027}{Re_x^{1/7}}. \tag{1.18}$$

Even though Equation (1.18) produces a good estimation of C_f, a more exact relation for flat plate turbulent skin friction is presented by White (1991) and it is preferred to be used:

$$C_f = \frac{0.455}{\log^2(0.06Re_x)}. \tag{1.19}$$

The most general characteristics for a laminar and turbulent boundary layer evolving over a flat plate have been introduced and for further details the reader can consult the following references: Schlichting & Gersten (2017), Pope (2000) and White (1991).

1.4 Transition

Laminar and turbulent boundary layers have been briefly described in the previous sections and they have also been largely studied and characterized over the last centuries. However, the process through which the boundary layer changes from the laminar to the turbulent state, i.e. transition, is still not understood completely. Moreover, since this phenomenon can occur in practically every flow in nature, either internal (pipes, channels) or external (boundary layer development over a surface), its comprehension is utterly relevant for its numerous engineering applications in the Aerodynamics and Fluid Mechanics fields.

Laminar-to-turbulent transition has been observed experimentally for a long time. It was first visualized and documented by Osborne Reynolds (Reynolds 1883) on a fluid flowing through a straight pipe. He observed how the flow suddenly changed as the Reynolds number was increased. It went from a laminar state with well-ordered layers moving alongside each other to a turbulent state with strong mixing effects. He also introduced the concept of critical Reynolds number, Re_{cr}, which is the Re at which transition occurs. In other words, when $Re < Re_{cr}$, the flow is laminar and when $Re > Re_{cr}$ the flow is turbulent. For his pipe experiments, O. Reynolds found that $Re_{cr} = 2300$. However, it was later found that Re_{cr} varies and becomes larger as the disturbances at the pipe entrance become smaller. In general, it

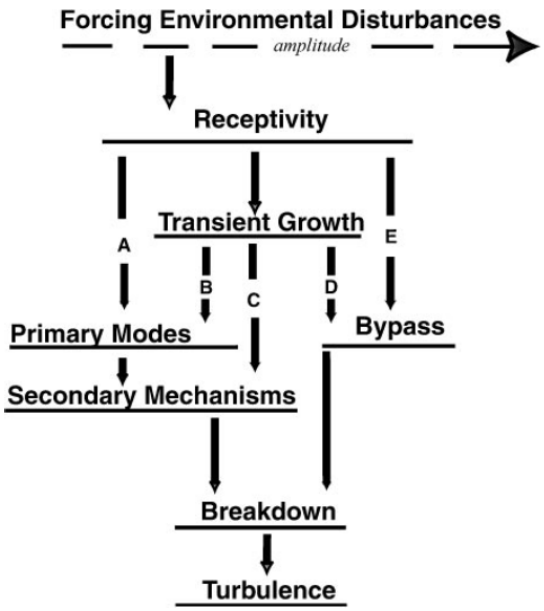

Figure 1.3: Different paths leading to turbulence (Morkovin 1994).

has been observed that the transition of a flow depends mainly on the Reynolds number, the pressure distribution, the wall roughness and the free-stream turbulence intensity.

1.4.1 Paths to turbulence

Even though the phenomenon has been observed for a long time, the transition mechanism itself is still not understood completely. In order to clarify the different possible mechanisms through which transition can occur, Morkovin (1994) proposed a map for the different transition paths, which is shown in Figure 1.3.

The first stage on the transition process is the *receptivity*. The receptivity, whose concept was firstly introduced by Morkovin (1969), is defined as the process through which external disturbances enter the boundary layer. These external perturbation can come from many sources, such as free-stream turbulence, wall-roughness or sound, and they provide the initial conditions (amplitude, frequency and phase) of the boundary layer instabilities that, depending on the flow characteristics, will either grow and cause transition or decay (and the flows stays in laminar state) (Saric et al. 2002).

Once that the disturbances have entered into the boundary layer, transition can occur by one of the five different paths shown in Figure 1.3. Path A is followed if weak disturbances enter to the boundary layer. The growth of the primary modes can be described with Linear Stability Theory (LST) (Reed et al. 1996), and it occurs over long streamwise distances. Later, secondary instabilities occurs in the form of three-dimensional nonlinear interactions

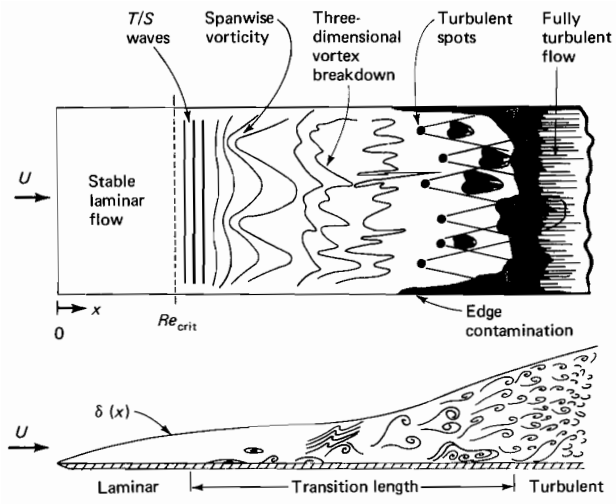

Figure 1.4: Sketch of the laminar-to-turbulent transition of a boundary layer over a flat plate (White 1991).

and the disturbances grow much faster followed by breakdown into turbulence. In this path, transition due to Tollmien-Schlichting (TS) waves can be categorized. Görtler vortices, which later evolve into secondary instabilities, also follow this path.

Sometimes the disturbances are so strong (high free-stream turbulence or roughness) that the growth of linear instabilities is bypassed (Morkovin 1993). In this case, Path E is followed and it is identified with the sudden appearance of turbulence spots or subcritical instabilities. Also, for this case, LST is not able to predict transition.

Finally, transient growth of the disturbances can also happen. It occurs when two, non-orthogonal, stable modes interact, undergo algebraic growth, and then decay exponentially (Saric et al. 2002). Depending of the initial conditions, large amplitudes can be achieved. Moreover, depending on these amplitudes, the disturbances can either follow path B, where spanwise modulations of two-dimensional waves occur, path C, where secondary instabilities or subcritical instabilities are generated, or path D, that bypasses primary and secondary instabilities.

1.4.2 Transition over a flat plate

Over a flat plate, the boundary layer is initially always laminar but after certain distance it becomes turbulent. Transition normally takes place at the critical Reynolds number based on the streamwise position of $Re_{x_{cr}} = 3.5 \times 10^5$ to 10^6 (Schlichting & Gersten 2017). Similar to the pipe case, $Re_{x_{cr}}$ is increased when the perturbations are small.

The overall transition process of an incompressible boundary layer past a flat surface is represented in Figure 1.4, which was depicted by White (1991). At first, transition starts with the introduction of disturbances to the laminar boundary layer, i.e. receptivity. As a

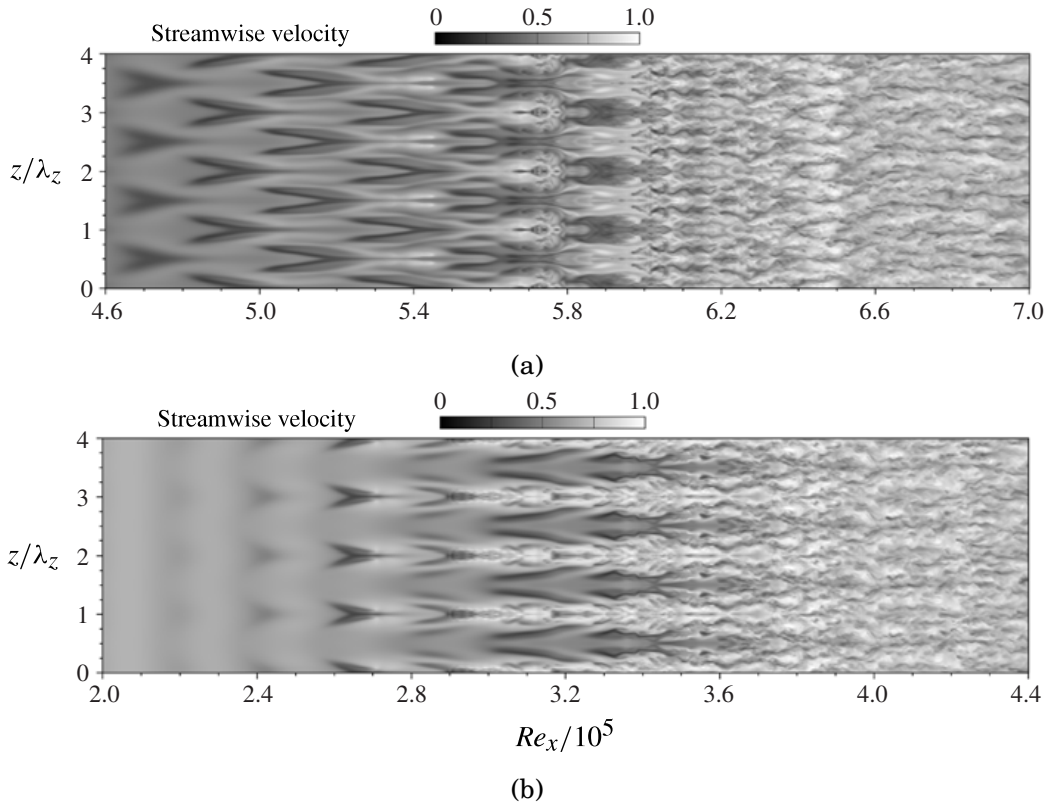

Figure 1.5: Contours of the instantaneous streamwise velocity, U/U_∞, on a flat-plate transition process. The different patterns of Λ-shaped vortices that are formed are shown. (a) H-type transition with staggered Λ structures. (b) K-type transition with aligned Λ structures. DNS results of Sayadi et al. (2013).

consequence of that, instabilities in the form of two-dimensional (2D) Tollmien-Schlichting waves (or TS waves) are generated. When they are initially formed, their amplitude is so small that they are not capable of triggering transition. However, as they travel in the streamwise direction, they amplify and eventually produce nonlinear effects, characteristics of the transition process (Duck et al. 1996). Transition due to TS waves were firstly seen experimentally and confirmed by Schubauer & Skramstad (1948). However, they had been investigated and predicted theoretically several years before by Tollmien (1931) and Schlichting (1933), who computed the first neutral stability curves for a flat plate by means of LST.

Downstream, the TS waves start to present some three-dimensional (3D) effects and spanwise variations become noticeable. Saric & Thomas (1984) visualized experimentally, by varying the amplitude and frequency of the vibrations of a ribbon, the growth process of the TS waves and observed two different types of breakdown scenarios. They both produced different patterns of Λ-shaped vortices, which are characterized for having two elongated legs

of oppositely signed streamwise vorticity and a tip of spanwise vorticity. The first pattern consisted in an in-line alignment (peak-following-peak) of the Λ vortices which were found to have the same wavelength as the TS waves (see Figure 1.5b). This transition scenario is called *K-type transition* after Klebanoff, who experimentally investigated it by triggering transition with a vibrating-ribbon technique (Klebanoff et al. 1962). The second observed pattern consisted in an staggered arrangement of the Λ vortices in a peak-following-valley structure with streamwise wavelength that is about two times the one of the TS waves (see Figure 1.5a). This type of transition is called *H-type transition* after Herbert, who provided the theoretical formulation for this secondary instability (Herbert 1988). Recently, the two transition scenarios have been investigated numerically by Sayadi et al. (2013), by means of DNS, finding that, even though transition is delayed for the H-type, both transition scenarios collapse after the skin friction coefficient maximum near $Re_\theta = 900$. Their computed transition scenarios are illustrated in Figure 1.5; where the spanwise coordinate, z, is non-dimensionalized with the spanwise wavelength of the Λ-shaped vortices, λ_z.

Later downstream, the Λ vortices begin to breakdown into smaller units, until the relevant frequencies and wavenumbers become random. Then, turbulence bursts locally and arbitrarily in time and space. These localized regions, which were first documented by Emmons (1951), are called *turbulence spots*. Later on, these turbulence spots start to merge into a region where they continually exist. This region marks the beginning of the *fully turbulent flow* and the culmination of the laminar-to-turbulent transition process over a flat plate.

The transition process, however, as explained previously, can follow another path when the external disturbances entering the boundary layer are high. When the free-stream turbulence intensity, Tu, is of the order of 1% or more, the Tollmien-Schlichting route is bypassed and the region of intermittent turbulent spots formation is reached directly. This transition scenario has been studied numerically by Jacobs & Durbin (2001) who triggered transition using a $Tu = 3.5\%$. They observed that once fully formed, the turbulence spots spread laterally and grow longitudinally. They maintain their upstream edge, which is a zone of juxtaposed laminar streaks and fully turbulent areas. Downstream, once the transition is over, the boundary layer is turbulent across its entire span. Wu & Moin (2009) triggered bypass transition, numerically, by inserting periodically short regions of free-stream turbulence. This method resulted in the generation of abundant packages of hairpin vortices which were responsible of the boundary layer breakdown to turbulence.

1.5 Transition over a concave surface

The transition of a boundary layer passing over a concave plate is very different from that of a flat plate. The curved motion of the flow creates a centrifugal force acting in the wall-normal direction that is balanced by a negative pressure gradient generated in the same direction. The resulting force field makes the boundary layer susceptible to develop centrifugal instabilities that can be easily triggered by a radial displacement of the fluid par-

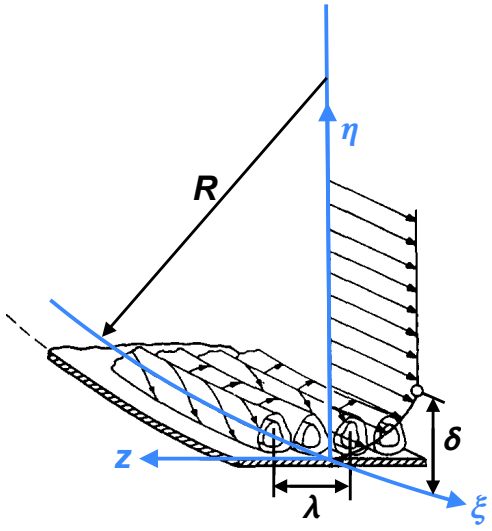

Figure 1.6: Sketch of the Görtler vortices developing over a concave surface (Saric 1994). The radius of curvature, R, and the Görtler vortices wavelength, λ, are indicated. The three-axis coordinate system (ξ,η,z) for a concave surface is also shown.

ticles which can be caused by different types of perturbations such as wall-roughness or free-stream turbulence intensity. These centrifugal instabilities, that initiate the transition process, have the form of steady streamwise-oriented counter-rotating vortex pairs and are known as **Görtler vortices**.

A sketch of these vortices developing over a concave surface is shown in Figure 1.6, which was depicted by Saric (1994); where R is the surface radius of curvature and λ is the Görtler vortices spanwise wavelength, that remains constant during their development. Moreover, the coordinate system (ξ,η,z) utilized for the flow analysis over a concave surface is also shown. ξ is the tangential streamwise coordinate, η the wall-normal coordinate and z the spanwise coordinate. Another helpful sketch can be found in Figure 1.7 which depicts the cross-section (η-z plane) of the Görtler flow. Basically, due to the swirl motion of the Görtler vortices, spanwise variations of the flow are generated where two particular regions can be distinguished: (i) a region where two vortices meet having an upward motion, which is called upwash, and, (ii) a region where two vortices meet having a downward motion, which is called downwash.

1.5.1 Some engineering applications

The study and characterization of the Görtler vortices is relevant because they are known to be the cause of transition in many flows of practical importance. Regarding aerodynamic applications, they can appear on the pressure side of an airfoil due to its concave geometry. Mangalam et al. (1985, 1987) experimentally visualized, by means of a chemical sublima-

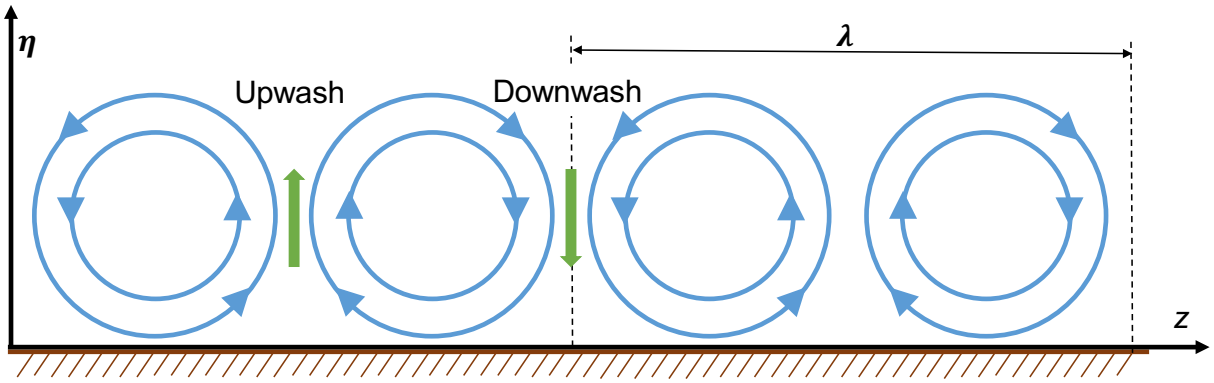

Figure 1.7: Sketch of the Görtler vortices on a cross-section η-z plane.

tion method, their development and evolution into secondary instabilities over a wing model developed at NASA Langley Research Center (see Figure 1.8). The authors suggested that the vortices may also play an important transition role on the modern supercritical laminar-flow-control wings which have concave regions near the leading and trailing edges of the pressure surfaces. Reed & Saric (2008) reviewed the transition mechanisms that can be encountered on a swept transport-aircraft wing; pointing out that Görtler vortices can develop, but can also be controlled by choosing an appropriate airfoil design. However, these vortices appear over supercritical airfoils for high subsonic transports since they have been designed with sharp leading edges requiring a concave surface to provide section thickness downstream. Pfenninger et al. (1980) studied the minimization of their growth in order to prevent transition and, hence, reduce drag over the wing. They suggested to deflect the flow towards areas of shorter concave curvature, combined with a boundary layer suction technique.

The development of Görtler vortices over the pressure side of a Savonius-style VAWT blade was investigated, by means of DNS, by Ducoin et al. (2016, 2017) (see Figure 1.19). They found that the vortices alter the blade aerodynamic performance by modifying the pressure and wall friction distribution which consequently alter the drag and lift forces. Moreover, they compared their DNS results with 3D Unsteady Reynolds-Averaged Navier-Stokes (URANS) simulations finding that the average C_f along the blade is two times higher when using DNS. This is due to the development and breakdown of the longitudinal vortices that cannot be observed in the URANS computations; which highlights the necessity of accurate data coming from DNS computations for such engineering geometry.

Görtler vortices development has also been reported over the pressure side of a gas turbine blade. These components have to withstand extremely high temperatures when placed at the exit of a combustion chamber and the components materials cannot cope with such hot environments. It is therefore quite relevant to understand the boundary layer development when formed over them in order to mitigate the frictional losses and increase the surface

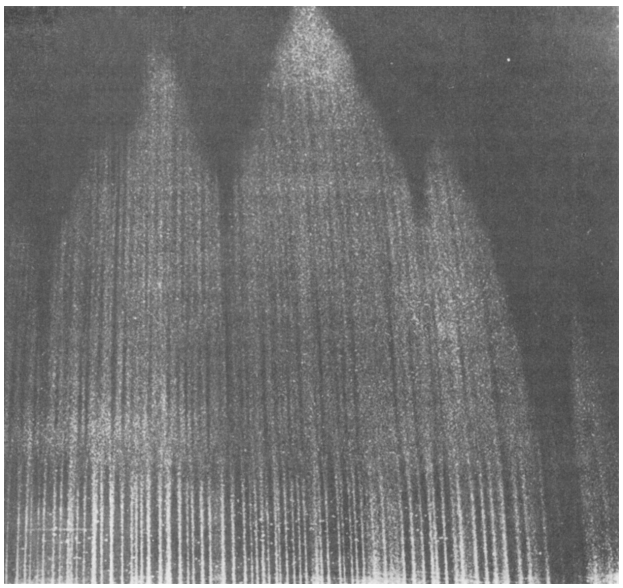

Figure 1.8: Görtler vortices developing over an aircraft wing designed at NASA Langley Research Center (Mangalam et al. 1985).

heat transfer. Han & Cox (1982) observed, experimentally, that the laminar-to-turbulent transition on the blade pressure side occurred due to an interaction between TS waves and Görtler vortices, that were originated by the blade high curvature. They also noticed that the Görtler vortices tend to modify the Karman vortices that are formed near the trailing edge and normally interact with a downstream turbine cascade as they are convected through the blade wake. Wang et al. (2005, 1999) found, experimentally, that, over the turbine blade pressure side, Görtler vortices were generated due to the blade leading edge roughness; which is normally formed during the component casting. They varied this wall-roughness observing that, when the disturbance is higher, stronger Görtler vortices appear enhancing significantly the mass transfer (up to 100% increase of the Sherwood number). Noticing that mass transfer rate is not as strongly enhanced by the free-stream turbulence as it is by the Görtler vortices. Cui et al. (2016) observed, by means of Large Eddy Simulations (LES), that the Görtler vortices are more likely to form, over the blade pressure side, when the turbulence intensity is low. This is due to the fact that the momentum thickness, which is a key parameter for their appearance, tends to be higher on this scenario. Morata et al. (2012) and Gourdain et al. (2011), also using LES, reported a clear raise on the wall heat transfer of up to 80%, on the blade pressure side, caused by the Görtler vortices that perturbed the thermal boundary layer.

Görtler vortices can also develop over the walls of a jet-engine nozzle due to its concave geometry. These devices are very noisy and an utilized control technique to reduce the noise levels is the boundary layer transition delay. Chen et al. (1985) and Beckwith & Holley (1981) observed experimentally that transition in the wall boundary layers of nozzles for

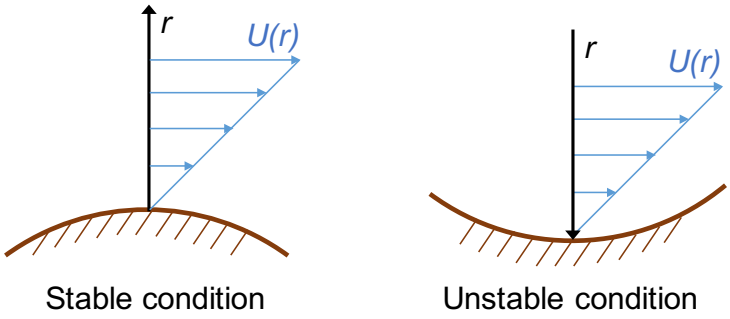

Figure 1.9: Examples of the Rayleigh circulation criterion.

Mach numbers from 3 to 5 was caused by the Görtler instability mechanism in the concave curvature regions rather than by TS waves. Based on these transition findings, Chen et al. (1993, 1992, 1990) proposed a quiet nozzle design, for supersonic and hypersonic velocities, with slower expansion rates that postponed the initiation and decreased the growth of the Görtler vortices so that lower noise levels could be reached.

1.5.2 Inviscid instability

The stability of an inviscid shear flow passing over a curved surface, either concave or convex, can be studied with the *Rayleigh circulation criterion* (Rayleigh 1917). This criterion analyses a velocity profile with a velocity vector: $U = U(r)$, $V = W = 0$; over a circular geometry with cylindrical coordinates (ξ, r, z), where ξ is the streamwise coordinate, r the radial coordinate and z the spanwise coordinate. It establishes that the sole condition for the existence of an inviscid instability is:

$$\frac{d(\Gamma^2)}{dr} < 0, \tag{1.20}$$

where Γ is the circulation defined as $\Gamma = rU$. Basically, the criterion was derived from an analysis of the angular momentum conservation of an inviscid fluid particle suffering a radial displacement product of a perturbation. When the instability condition (Eq. 1.20) is not met, the local pressure gradient is able to return the particle to its original position. On the other hand, when the condition (Eq. 1.20) is met, the local pressure gradient is not able to restrain the excess in angular momentum of the deflected particle and, therefore, its radial displacement is reinforced. The cases of the Rayleigh stability criterion for convex and concave walls are shown in Figure 1.9. Over a convex wall, the flow with $U = U(r)$ is naturally stable since $d(\Gamma^2)/dr > 0$. On the other hand, the flow over a concave surface is unstable since $d(\Gamma^2)/dr < 0$.

Centrifugal instabilities can occur in several types of flow where the Rayleigh circulation criterion is met. One of them is the Couette flow over two rotating coaxial cylinders which

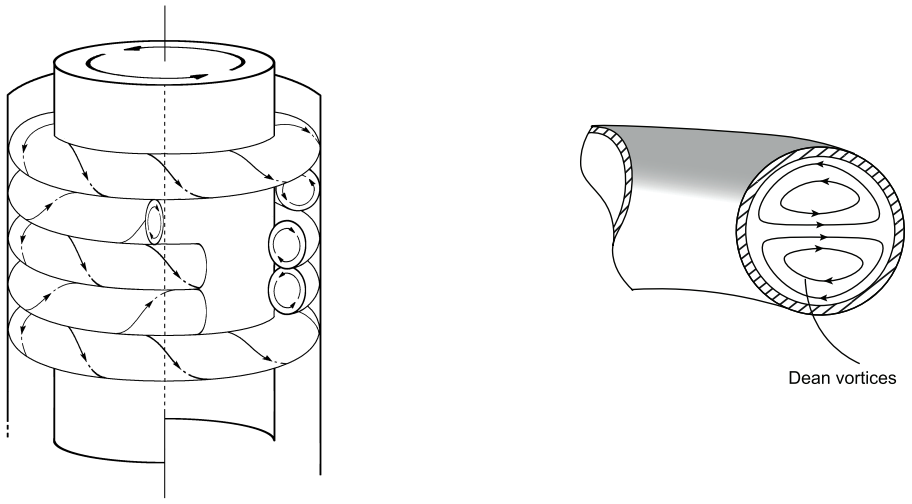

(a) (b)

Figure 1.10: Other types of counter-rotating streamwise vortices developing when the Rayleigh circulation criterion (Equation 1.20) is met. (a) Taylor vortices developing in the gap between two rotating cylinders (Lueptow 2009). (b) Dean vortices developing inside a curved pipe (Belligoli et al. 2017).

results in an instability in the form of counter-rotating toroidal vortices normally called *Taylor vortices* (Taylor 1923). This flow type is a *closed system* since the streamlines are closed on themselves and the instability appears in a confined system. Thus, a permanent feedback exists and the rolls are auto-regenerated by themselves (Petitjeans & Westfried 1996). Moreover, it is also a *parallel flow*, i.e. only the streamwise velocity component of the base flow is different from zero and, therefore, by solving the continuity equation, it does not depend on the streamwise coordinate. Centrifugal instabilities can also occur in curved pipes and channels. The resulting instabilities are the *Dean vortices* (Dean 1928) which have the form of streamwise oriented rolls. In this case, the flow is an *open system*, since it does not shape a loop, with a parallel basic state. An schematic representation of both types of secondary flows is illustrated in Figure 1.10.

Lastly, the Rayleigh instability criterion (Equation 1.20) can also be met when the flow is passing over a concave wall. In this case, the developing instabilities are called *Görtler vortices* (Görtler 1940), which are shown in Figure 1.6. This flow type is an open system in the sense that the flow is not closed on itself as in the in the Taylor instability. The Görtler problem is also a *nonparallel flow* since both the base flow and the perturbations are spatially inhomogeneous. It is thus the ensemble of the characteristics (open system, nonparallel flow, spatially-evolving) which make the Görtler flow quite unique and different from the other centrifugal instabilities, i.e. Taylor and Dean vortices.

Floryan (1986) developed another simple stability criterion in order to identify the shear

layers that are potentially unstable to develop centrifugal instabilities in the form of Görtler vortices. It was found that monotonic velocity profiles (such as the Blasius profile) are stable over a convex wall but unstable over a concave wall; and that non-monotonic profiles (such as a wall jet) are unstable over both convex and concave walls.

With respect to the development of Görtler vortices on convex walls due to wall jets, very little attention has been given to the subject and quite few studies can be found confirming their possible appearance by means of LST, which has been used to produce the neutral curves of the stability problem (Le Cunff & Zebib 1996, Wadey 1992, Floryan 1986, Kahawita 1975). Nevertheless, the appearance of Görtler vortices on convex walls, as well as their evolution into secondary instabilities, has been confirmed experimentally, through smoke visualization, by Matsson (1998); who also found that transition due to wall jets occurs further downstream on a convex wall compared to a concave wall.

1.5.3 Linear stage of the Görtler flow

As shown in the previous section, the flow developing over a concave wall is highly susceptible to develop centrifugal instabilities in the form of Görtler vortices. It was Henry Görtler (Görtler 1940) who proposed a non-dimensional parameter that determines the appearance of the longitudinal vortices in a boundary layer over a concave surface. This parameter, known as the *Görtler number* G_θ, is defined as:

$$G_\theta = \frac{U_\infty \theta}{\nu}\sqrt{\frac{\theta}{R}} = Re_\theta\sqrt{\frac{\theta}{R}}. \tag{1.21}$$

G_θ consists in the product of the Reynolds number and a curvature parameter. Therefore, it represents a ratio of the destabilizing inertial and centrifugal forces to the stabilizing viscous forces.

1.5.3.1 Linear stability theory

Most of the first theoretical studies of the Görtler vortices were focused in finding the existence of a unique critical Görtler number, $G_{\theta_{cr}}$, that would determine their onset. Those analysis were performed using linear stability theory and an extensive review can be found in the works of Saric (1994), Floryan (1991) and Hall (1990).

LST studies the growth, or decay, of a small perturbation superimposed to a basic flow. That way, the flow stability can be deduced and it can be determined whether transition will occur or not. The velocity flow field have thus the form:

$$\mathbf{U} = \mathbf{U_b} + \mathbf{u}, \tag{1.22}$$

where $\mathbf{U_b}$ is the basic-flow velocity vector and $\mathbf{u}$ is the perturbation velocity vector. Later, Eq. (1.22) is inserted into the Navier-Stokes equations which are linearized by assuming that all quadratic terms of the perturbation are small and can be neglected.

For the Görtler problem, it has been largely seen experimentally that, during the streamwise development of the longitudinal vortices, the disturbance velocities grow while their spanwise wavelength, λ, remains constant; which have led to the conclusion that the vortices can be described by a single spanwise Fourier mode (Saric 1994). Hence, the LST equations can be obtained by superimposing small, steady, spanwise disturbances to the basic flow. The disturbance velocity vector has then the form of:

$$\mathbf{u} = [u(\xi,\eta), v(\xi,\eta), w(\xi,\eta)]\cos(\alpha z), \tag{1.23}$$

where (u,v,w) are the components in the streamwise, ξ, wall-normal, η, and spanwise, z, directions, respectively. α is the spanwise wavenumber which is defined as: $\alpha = 2\pi/\lambda$. The Görtler flow disturbance equations can be then obtained. They can be found in the work of Floryan & Saric (1982), who proposed their correct form for the first time. The authors obtained the equations by using optimal curvilinear coordinates, by introducing two different scales for the disturbance velocities in order to capture the weakness of the vortex motion, and, by considering only spatial LST since the disturbances evolve spatially rather than temporally.

Once that the disturbance equations are formulated, they can be solved by one of two approaches. One of them is the so-called *normal-mode method*, or local approximation, which let the disturbances take the form:

$$\mathbf{u} = [u(\eta), v(\eta), w(\eta)]\cos(\alpha z)\exp(\beta\xi), \tag{1.24}$$

where β is the spatial growth rate. This leads to an exponential approximation of the disturbances streamwise growth and to an eigenvalue problem of the form $F(G_\theta, \alpha, \beta) = 0$. The solution of Floryan & Saric (1982) disturbances equations, by using the normal-mode method, is shown in Figure 1.11 where curves of constant amplification rate, β, are plotted. Figure 1.11a plots the Görtler number, G_θ, versus the wavenumber, α; whereas Figure 1.11b plots G_θ versus the nondimensional spanwise wavelength, Λ, which is defined as:

$$\Lambda = \frac{U_\infty \lambda}{\nu}\sqrt{\frac{\lambda}{R}}. \tag{1.25}$$

Some interesting remarks can be obtained from the LST diagrams. One of them is that the curve of maximum amplification for a given Görtler number occurs in the range of $\Lambda = 190$ to 260 for the range of $G_\theta = 1$ to 20. Also, the presented experimental points preserve their wavelength, Λ, during their development. Moreover, a neutral stability curve ($\beta = 0$) can be obtained, above which the flow is unstable, and can breakdown into turbulence, since the disturbances will grow ($\beta > 0$). Additionally, based on these LST diagrams, Floryan & Saric (1984) studied the wavelength selection mechanism suggesting that if vortices are not established until at least $G_\theta \simeq 2$, then the vortices of $\Lambda \simeq 200$ should have the highest growth rates and should dominate the instability. Nevertheless, since the minima of the curves of

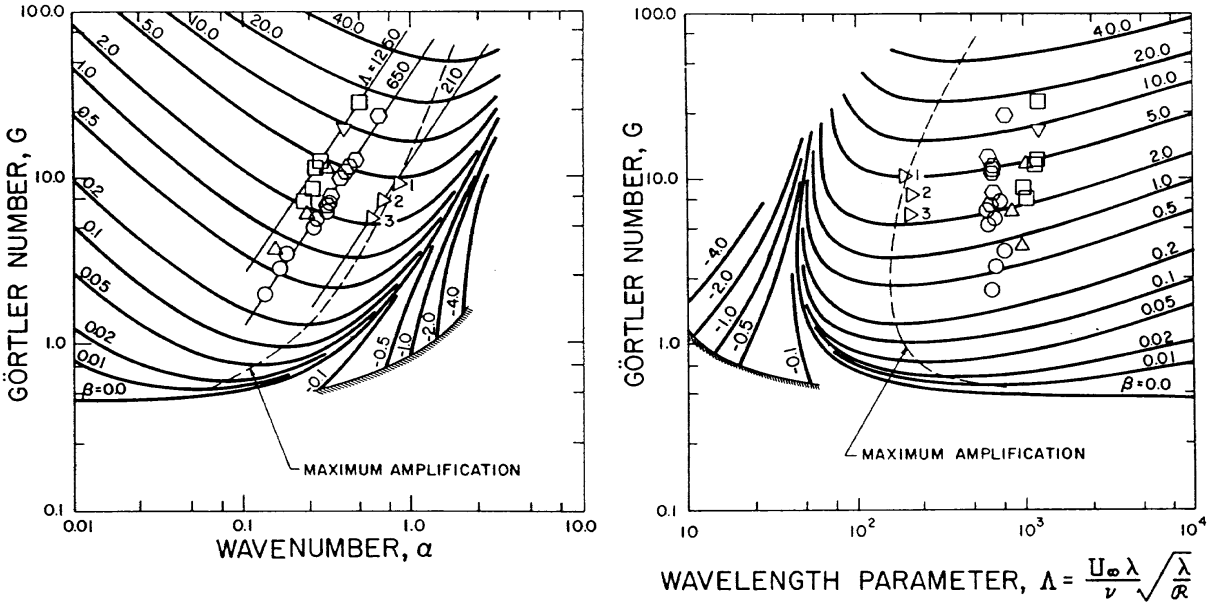

(a) (b)

Figure 1.11: Linear stability diagrams of the Görtler problem showing lines of constant amplification rate β from Floryan & Saric (1982). (a) G_θ versus α. (b) G_θ versus Λ. Experimental points, ○,□,△,▽, from Tani & Sakagami (1962); and, ▷, from Bippes (1972).

constant growth rate in Figure 1.11b are relatively flat, a whole band of wavelengths may be equally predestined to emerge.

However, there is an issue when solving the LST Görtler problem. It comes from the fact that the normal-mode solution utilizes a separation of variable method where the flow dependence on the streamwise coordinate is lost and results in the wrong assumption of parallel flow. However, in the linear stage, nonparallel effects completely govern the disturbances growth and parallel flow theories do not capture correctly the vortices development. Hence, LST studies use the parallel flow assumption that disregards the streamwise dependence of the disturbance velocity field and results in the generation of incorrect neutral stability curves (Hall 1990). Nevertheless, Floryan (1991) argues that the normal-mode method can be seen as a local approximation analysis.

It was thus Hall (1982, 1983) who showed, by solving numerically the Görtler problem perturbation equations using a *marching solution*, that the position of the neutral stability curve depends on the boundary layer receptivity, i.e., the location and character of the initial disturbances. Hence, the concept of a unique critical number, so familiar in hydrodynamic-stability theory, is not suitable in the Görtler flow, except for asymptotically small wavelengths. Therefore, it was concluded that the most appropriate approach for solving the Görtler instability analysis is the *numerical integration* of the governing hydrodynamic equations, rather than using LST, which needs to use the normal-mode method.

Day et al. (1990) compared both methods, the normal-mode method and the marching solution. They found that, when the perturbation initial conditions are provided from the local theory eigenfunctions, the normal method tends to overestimate the growth rates by modest amounts and that, with some corrections, the LST diagrams can be used for engineering studies. However, they agree with Hall (1983) in the fact that the small wavenumber part of the neutral stability curve cannot be estimated since it depends on the receptivity. Later on, Bottaro & Luchini (1999) showed that nonparallel effects can be accounted for, on local analysis, by using a WKB (Wentzel-Kramers-Brillouin) expansion method. This method is used for finding approximate solutions to linear differential equations with spatially varying coefficients. The highest derivative is multiplied by a small parameter, which was taken as the inverse of the Görtler number, and the solution is derived in the form of an asymptotic series expansion continuable to all orders. The authors computed the growth rate of several wavelegths, Λ, and showed that their method produces a perfect match with the marching solution, except for $G_\theta \lesssim 7$. Above this value, there is an asymptotic behavior independent of the initial stage. Below it, the influence of the inlet condition is felt which supports Hall's argument that a unique neutral curve cannot be defined.

1.5.4 Early studies and visual evidence

Several experimental studies have been performed in order to visualize and characterize the development of the Görtler boundary layer. Among the most relevant early experimental studies, the work of Tani (1962) can be mentioned. He analyzed a concave surface model inside a wind tunnel with $Tu < 0.3\%$ and confirmed the appearance of the streamwise-aligned vortices predicted by LST by measuring the spanwise periodic variation of the streamwise velocity. Moreover, he noticed that this wavelength, Λ, remains constant as the vortices develop (as shown in Figure 1.11). He was also able to compute the growth rate of the vortices which was slightly smaller compared to LST prediction. Bippes (1972) and Bippes & Görtler (1972) provided one of the first detailed observations of the Görtler vortices development by means of the hydrogen-bubble visualization technique. They utilized a water towing tank that allowed them to work with a low turbulence intensity flow. They introduced isotropic disturbances by placing screens ahead of the test section in order to measure the most dominant wavelengths, along with their growth rates, which were found to be in the range of $\Lambda = 195$ to 212 (see Figure 1.11). Moreover, they preset the spanwise periodicity by placing longitudinally oriented heating wires and observed the growth, or damping, of several wavelengths which allowed them to generate a neutral stability curve for high wavenumbers, α. This curve was found to be slightly shifted to right compared to the one generated by LST in the (α,G_θ) diagram. They also studied qualitatively the effect of the wall curvature and observed that transition occurs faster on more strongly curved surfaces since the Görtler number is higher.

Several experimental studies have been focused in the visualization of the phenomenon. Mangalam et al. (1985) visualized the emergence of Görtler vortices over the concave re-

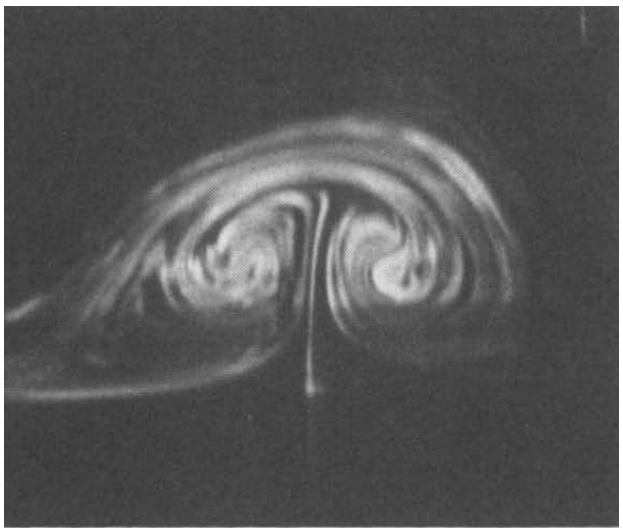

Figure 1.12: Mushroom-like structure which is formed by a pair of Görtler rolls (Peerhossaini & Wesfreid 1988*b*).

gion of a wing prototype designed at the NASA Langley Research Center (see Figure 1.8). The wing black surface was covered with white biphenyl whose rate of sublimation is proportional to the surface shear stress. Later, the chemical sublimated on the downwash locations and the authors were able to visualize a pattern of streamwise streaks with fixed uniform spanwise spacing. This occurred because the Görtler instability increases the shear stresses at the downwash regions and decreases them at the upwash regions (see Figure 1.7). Peerhossaini & Wesfreid (1988*b*,*c*) carried out some water experiments and presented some dye visualization results. They captured the emergence of a mushroom-like structure, which is formed by a pair of Görtler rolls and is typically present in the Görtler flow (Figure 1.12). Basically, due to the swirl action of the vortices, the injected dye is pushed away of the wall at the upwash and then forced downwards at the downwash to form the contour of the Görtler rolls. As G_θ increased, they observed lateral oscillations of this structure which they related to the appearance of a secondary instability. The spectra of the observed oscillations showed a peak at a frequency between 0.2 and 0.275 Hz. Downstream, the flow became turbulent and they reported an intermittent presence of the Görtler rolls.

1.5.5 Receptivity and wavelength selection mechanism

It is recognized that the onset and development of the Görtler instability is influenced by the character and location of the of the initial disturbances, and that receptivity plays an important role in the resulting flow structure (Hall 1983). Regarding the wavelength, Λ, of the Görtler vortices that is preserved along their streamwise development, several values have been observed experimentally and it seems that there is no natural wavelength selection mechanism. According to LST, vortices of $\Lambda \simeq 200$ should have the highest growth rates

and should dominate the linear regime of the transition process (Floryan & Saric 1984). Guo & Finlay (1994) studied the wavelength selection mechanism and determined that the growth rate of the primary instability does not vary significantly from $\Lambda = 175$ to 400. Therefore, if the perturbations near the leading edge are dominated by a wavelength within this widen wavelength range, this wavelength will have a better chance to develop into dominant vortices. Moreover, if all wavelengths in the perturbation have equal energy, wavelengths near $\Lambda = 210$ are more likely to be observed due to their slightly higher growth rate. Kottke (1988) studied the effect of the test upstream facilities on the wavelength selection mechanism. The author demonstrated that the amplified wavelength is imposed by the upstream disturbance promoters such as screens, grids or honeycombs. He was able to manipulate the free-stream disturbance characteristics (amplitude and wavelength), by varying the mesh size and the distance of the screen to the leading edge, which excited Görtler vortices of different scale and strength. This is considered to be the reason of the results differences of various experimental studies.

Several types of perturbations can disturb the boundary layer and trigger the inception of the Görtler vortices. Relevant and realizable disturbances include surface wall-roughness and free-stream turbulence. The receptivity of the Görtler vortices to these disturbances was reviewed by Bassom & Seddougui (1995), who acknowledged the fact that very few attention has been given to the Görtler receptivity problem and only sparse results can be found in the literature. They pointed out that the importance of each mechanism depends on Λ. For small wavelengths, wall-roughness is an extremely poor mechanism because large vortices would be provoked by free-stream variations long before wall-roughness generated modes could be noticed. However, for $O(1)$ wavelength modes, the relative importance of the free-stream/roughness disturbances is largely determined by the form of the wall imperfection. An isolated roughness patch appears to be less important than the free-stream disturbance but a distributed roughness can often prove to be the dominant mechanism. Luchini & Bottaro (1998) computed Green's functions, for different boundary layer perturbations, which can be multiplied by the external disturbances in order to yield the downstream amplitude of the excited Görtler vortices. For free-stream fluctuations, they found that the receptivity is mostly governed by the spanwise wavenumber and it is maximum for the range of the most unstable Görtler vortices ($\Lambda = 220$ to 270) combined with a zero wall-normal wavenumber. Regarding wall disturbances, maximum receptivity occurs when they are placed at the leading edge with zero streamwise wavenumber and Λ also in the most unstable range.

Denier et al. (1991), whose work was later corrected by Bassom & Hall (1994), studied the excitation of the vortices due to wall-roughness. They showed that, for the case of $O(1)$ wavelength vortices, streamwise distributed roughness is much more efficient to generate vortices than isolated roughness or free-stream disturbances. Moreover, they predicted that in the absence of distributed roughness, isolated roughness elements would have a prevailing role in triggering vortices only in an environment virtually free of free-stream disturbances. Bottaro & Zebib (1997) studied numerically the receptivity to wall-roughness of a

boundary layer over a concave surface. They showed that ribleted surfaces of sufficiently large Λ are extremely efficient in triggering Görtler vortices whereas small wavelength riblets ($\Lambda < 50$) do not promote the vortex development. Besides, they observed that a spanwise thin strip of localized roughness is more efficient to excite the vortices compared to a wall completely covered of random roughness elements. Furthermore, they found that under a broad-band distribution of spanwise roughness wavenumbers, Görtler vortices of average wavelength close to that of largest growth predicted by LST ($\Lambda = 210$) develop. Sescu & Thompson (2015) studied numerically the effect of several roughness geometrical parameters (shape, height, diameter and spanwise separation) on the excitation of Görtler vortices. They found that bell-shaped distributed roughness elements are more likely to excite the Görtler instabilities than the cylindrical ones. Also, the increase of the roughness height produces an increases in the amplitude and size of the vortices for both roughness shapes. Additionally, by increasing the roughness diameter, the bell-shaped roughness elements are able to excite stronger vortices but the inverse effect is observed for the cylindrical elements.

As explained, the characteristics of free-stream turbulence influence the onset location and the amplitude of the Görtler vortices (Kottke 1988). Free-stream turbulence consists of acoustic, vortical and entropy modes of which free-stream vortical disturbances are considered to be the most significant. The excitation of Görtler vortices by free-stream vortical disturbances has been studied by Wu et al. (2011). Their numerical results showed that there is a critical value for Λ over which the induced perturbation exhibits exponential growth and under which it decays. Over the critical value, the perturbation acquires the modal shape of Görtler vortices rather quickly, and its growth rate approaches that predicted by local instability theories farther downstream. Moreover, the amplitude of the excited Görtler vortices is found to decrease as the frequency increases, with steady vortices being dominant. Similar conclusions were obtained by Schrader et al. (2011) who found that the boundary layer is most receptive to zero and low-frequency free-stream vortices which excite steady and slowly traveling Görtler modes and that this receptivity mechanism is linear. They also observed that vortical modes are more efficient at generating Görtler vortices than localized roughness.

1.5.6 Görtler vortices growth and nonlinear development

The Görtler vortices do not cause transition directly; instead, they distort the original flow field in such a way that it becomes unstable to secondary instabilities that breakdown into turbulence.

During the linear growth of the vortices, a 3D boundary layer with a spanwise periodic variation is generated due to their rotating motion. Mitsudharmadi et al. (2004) and Winoto et al. (2005) presented a quite vast experimental visual study that reveals this behavior. They forced the spanwise wavelength of the Görtler vortices by placing vertical wires equally spaced at the inlet of a concave surface. They plotted the velocity contours at several streamwise positions in order to observe the evolution of the Görtler vortices. A wavy

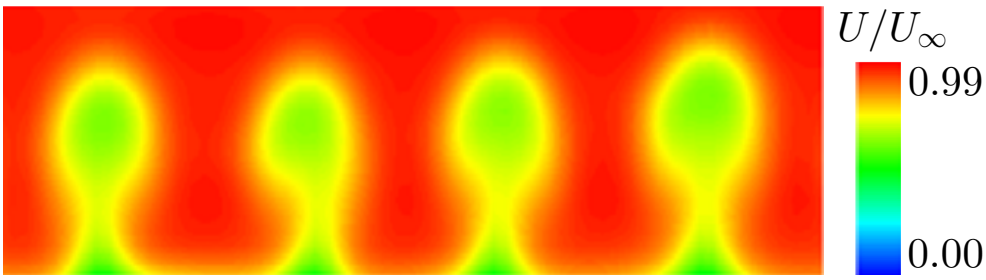

Figure 1.13: Streamwise velocity contours at a η-z plane showing the development of mushroom-like structures (Winoto et al. 2005).

spanwise variation of the streamwise velocity caused by the swirl motion of the vortices was captured and the upwash and downwash regions were identified. In the upwash region, the upward movement of the vortices pushes low velocity flow close to wall towards the boundary layer edge; on the other hand, in the downwash region, the vortices downward movement pushes high velocity flow from the free-stream towards the wall. As the flow develops, the nonlinear region of the transition process was reached and the inception of a mushroom-like structure was observed (see Figure 1.13). Later, this region was followed by lateral oscillations of the vortices indicating the presence of secondary instabilities.

The region where the mushroom-like structures (Figure 1.12 and Figure 1.13) dominate the flow was studied by Lee & Liu (1992) by means of nonlinear marching computations. They studied the Görtler vortices development from the linear region to the fully nonlinear region just prior to the development of secondary instabilities. They found that these coherent structures are caused by strong nonlinearities created in the η-z plane, rather than in the streamwise direction. Downstream, the mushroom-like structures are destroyed due to development of secondary instabilities as well as the appearance of fine-scale turbulence. The authors also measured the perturbation energy of the primary instability realizing that when nonlinearities become significant its exponential growth stabilizes, i.e. it saturates.

The distortion of the flow also results in velocity profiles with high shear layers that become unstable due to the inflection point instability (Tollmien 1935) which eventually cause the flow to transition. These unstable profiles were documented by Ito (1980, 1987) who provided experimental measurements of the distribution $U(\eta)$ and $U(z)$ at several streamwise locations. The profile $U(\eta)$ was measured at downwash and upwash regions realizing that on the upwash the boundary layer thickness grows faster and an inflection point is acquired because low speed flow is riding over high speed flow. This behavior generates an S-shape distribution which is highly unstable and subject to the Kelvin-Helmholtz (von Helmholtz 1868) instability. On the other hand, the downwash velocity profile becomes fuller and more stable. At the same time, the spanwise distribution $U(z)$ generates high shear layers due to the spanwise wavy pattern of the flow which are also unstable and subject to the Rayleigh instability.

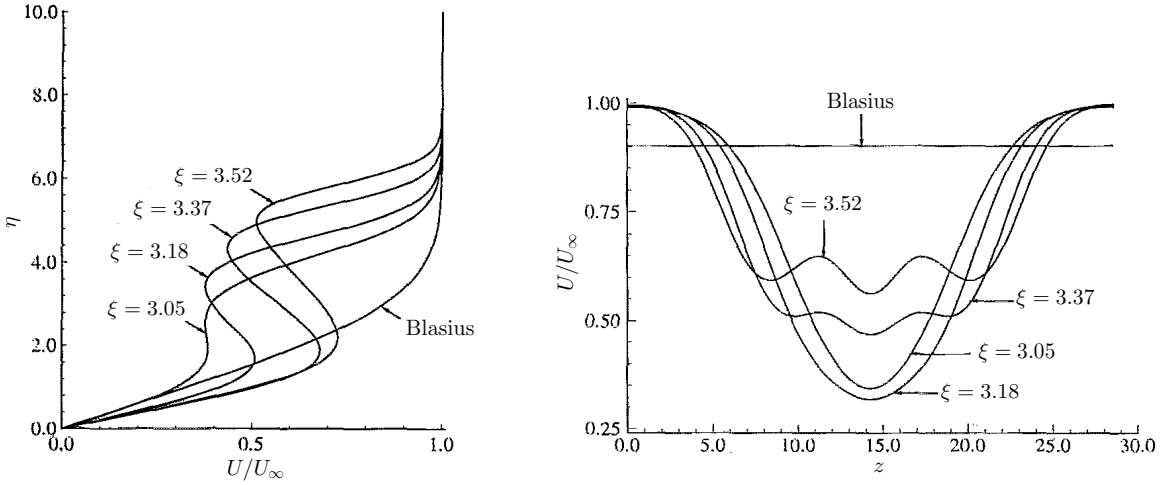

Figure 1.14: Distortion of the streamwise velocity distribution resulting in unstable inflectional profiles (Benmalek & Saric 1994). (a) $U(\eta)$ at the upwash. (b) $U(z)$.

Nonlinear marching computations have also been used to observe the development of the unstable inflectional profiles. Hall (1988) computed the highly inflectional $U(\eta)$ upwash profile and suggested that the distorted velocity distribution makes the flow highly receptive to rapidly growing secondary instabilities. Benmalek & Saric (1994) computed both unstable inflectional profiles, $U(\eta)$ and $U(z)$. Their evolution is shown in Figure 1.14. Moreover, the authors studied the stabilization of the inflectional profiles by changing the concave curvature downstream of their generation. By placing a convex curvature, the inflection points from spanwise and wall-normal profiles were eliminated and, therefore, the onset of secondary instabilities was prevented. A slower stabilization of the Görtler flow was also observed by placing a flat surface after the generation of the inflectional profiles.

Another important aspect of the nonlinear stage of the Görtler flow is the saturation of the disturbance growth. Several formulas for measuring the perturbation amplitude and its growth have been proposed (Petitjeans et al. 1990); and, even though some differences can be expected on the computed growth rate value, all of them lead to the same conclusion regarding the perturbation growth behavior and its eventual saturation. Finnis & Brown (1989, 1997) measured the vortex growth by proposing a perturbation amplitude parameter: $K(\eta) = (U_{down}(\eta) - U_{up}(\eta))/2U_\infty$; where U_{down} and U_{up} are the streamwise velocities at the downwash and upwash locations, respectively. By plotting the streamwise evolution of the maximum disturbance, K_{max}, they observed its exponential growth which followed a law of the type: $K_{max}(\xi) = Ae^{\beta\xi}$, where β is the spatial growth rate. They utilized a concave surface with $R = 3m$ and experimentally produced naturally developing vortices of several wavelengths finding a growth rate of $\beta = 3.7m^{-1}$. However, the surface streamwise length did not allow to reach the nonlinear stage. The streamwise evolution of K_{max} has also been studied experimentally by Mitsudharmadi et al. (2004) and by Tandiono et al. (2008). Both studies

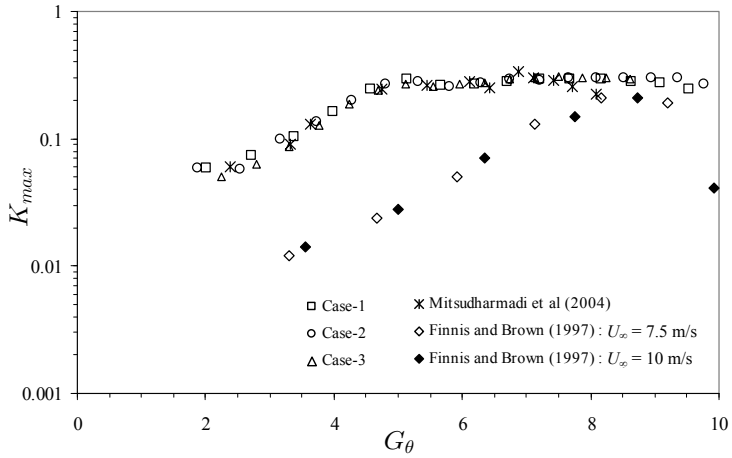

Figure 1.15: Comparison of the disturbances amplitude streamwise evolution. It is shown that Görtler vortices with the same wavelength, Λ, have the same growth rate and saturate at the same point (Tandiono et al. 2008). Case-1: $\Lambda = 250$ ($\lambda = 12$ mm, $U_\infty = 2.85$ m/s, $R = 1$ m). Case-2: $\Lambda = 250$ ($\lambda = 15$ mm, $U_\infty = 2.1$ m/s, $R = 1$ m). Case-3: $\Lambda = 250$ ($\lambda = 20$ mm, $U_\infty = 1.33$ m/s, $R = 1$ m). Mitsudharmadi et al. (2004): $\Lambda = 249$ ($\lambda = 15$ mm, $U_\infty = 3.0$ m/s, $R = 2$ m). Finnis & Brown (1997): natural developing vortices of several wavelengths, Λ ($U_\infty = 7.5$ m/s and 10 m/s, $R = 3$ m).

analyzed vortices with $\Lambda = 250$ but different growth rates in the linear stage were found due to the radius of curvature of their experimental setup. Mitsudharmadi et al. (2004), who utilized a $R = 2m$, obtained a growth rate of $\beta = 4.7m^{-1}$; whereas Tandiono et al. (2008), who utilized a $R = 1m$, obtained $\beta = 7.0m^{-1}$. As expected, higher curvatures resulted in higher growth rates. However, Tandiono et al. (2008) found that the growth rates of vortices with same Λ collapse when K_{max} is plotted vs. G_θ (see Figure 1.15). Mitsudharmadi et al. (2004) was also able to identify three regions in the plot of K_{max} vs. G_θ: (i) a linear region, where K_{max} grows exponentially and β is higher; (ii) a nonlinear region, where the growth rate is much more moderate and the finite amplitude of the disturbance is reached; and, (iii) a mushroom-decay region, where K_{max} decreases exponentially indicating the saturation of the disturbance amplitude.

Benmalek & Saric (1994) utilized a numerical marching solution, in which they included ten Fourier modes, for studying the disturbances growth. For all of the modes, they observed an initial linear growth followed by a saturation state product of the modes nonlinear interaction which was also associated to the appearance of the mushroom-like structure. Later, Peerhossaini & Bahri (1998), by performing spectral analyses on their experimental streamwise velocity profiles in the spanwise direction, showed that seven Fourier modes suffice to describe the velocity field in the nonlinear regime.

1.5.7 Secondary instabilities

As explained, the distorted flow field, product of the Görtler vortices growth, becomes susceptible to develop secondary instabilities. Swearingen & Blackwelder (1987) provided one of the most relevant works for the clarification of the secondary instabilities development and their breakdown into turbulence. They studied experimentally the natural development of the vortices which had a wavenumber of $\Lambda \sim 670$. They observed that the generated inflectional velocity profiles (Figure 1.14) develop some temporal fluctuations that grow quite rapidly and, thus, the breakdown into turbulence occurs within a short timescale. Prior to turbulence breakdown, they distinguished two different modes of secondary instability: (i) a sinuous mode, which is identified with the meandering motion of the vortices, and, (ii) a varicose mode, which is recognized by the emergence of horseshoe vortices. Their main finding was the association of the secondary instability with high shears in the spanwise direction rather than with those in the wall-normal direction; which was deduced by noticing that high turbulence intensity peaks correlate better with high dU/dz regions. Moreover, by comparing the streamwise growth rate of the temporal velocity fluctuations, Tu, with the growth rate of the primary instability amplitude, they found that secondary instabilities grow ~ 2.5 times faster. This finding agrees with the experimental results of Mitsudharmadi et al. (2005) who observed a growth rates ratio of 6.5:1.

The two secondary modes occur due to the high shears in the inflectional profiles. The sinuous mode, which was the predominant one in the Swearingen & Blackwelder (1987) observations, is associated to the Rayleigh instability originated by high shear dU/dz regions. This mode was also observed by Bippes (1972) (Figure 1.16) who documented an oscillatory motion of the vortices. This movement is explained due to the generation of the low-velocity mushroom-like structures that block the path of the high speed fluid which therefore must change direction (Floryan 1991). On the other hand, the varicose mode is linked to the Kelvin-Helmholtz instability originated by high shear $dU/d\eta$ regions. Basically, the high shear layers located on the upwash generate spanwise vortices which are then bent towards the wall by the streamwise Görtler vortices. This motion results in the generation of horseshoe vortices (Floryan 1991). This type of secondary instability was also observed by Aihara et al. (1985) (Figure 1.17).

The development of secondary instabilities has also been studied by means of numerical marching computations. Yu & Liu (1991) used the distorted nonlinear flow product of the Görtler vortices as the basic flow to which they added perturbations in the form of the sinuous and varicose modes. Flow conditions (Reynolds number, streamwise and spanwise wavenumbers) were supplied according to the experimental observations of Swearingen & Blackwelder (1987), finding that the sinuous mode grows faster and prevails over the varicose one. Similar results were obtained by Hall & Horseman (1991) who identified the 2D odd and even eigenfunctions that, respectively, represent the sinuous and varicose modes. They showed that the odd mode growth rate is twice as large as that of the even mode. Yu &

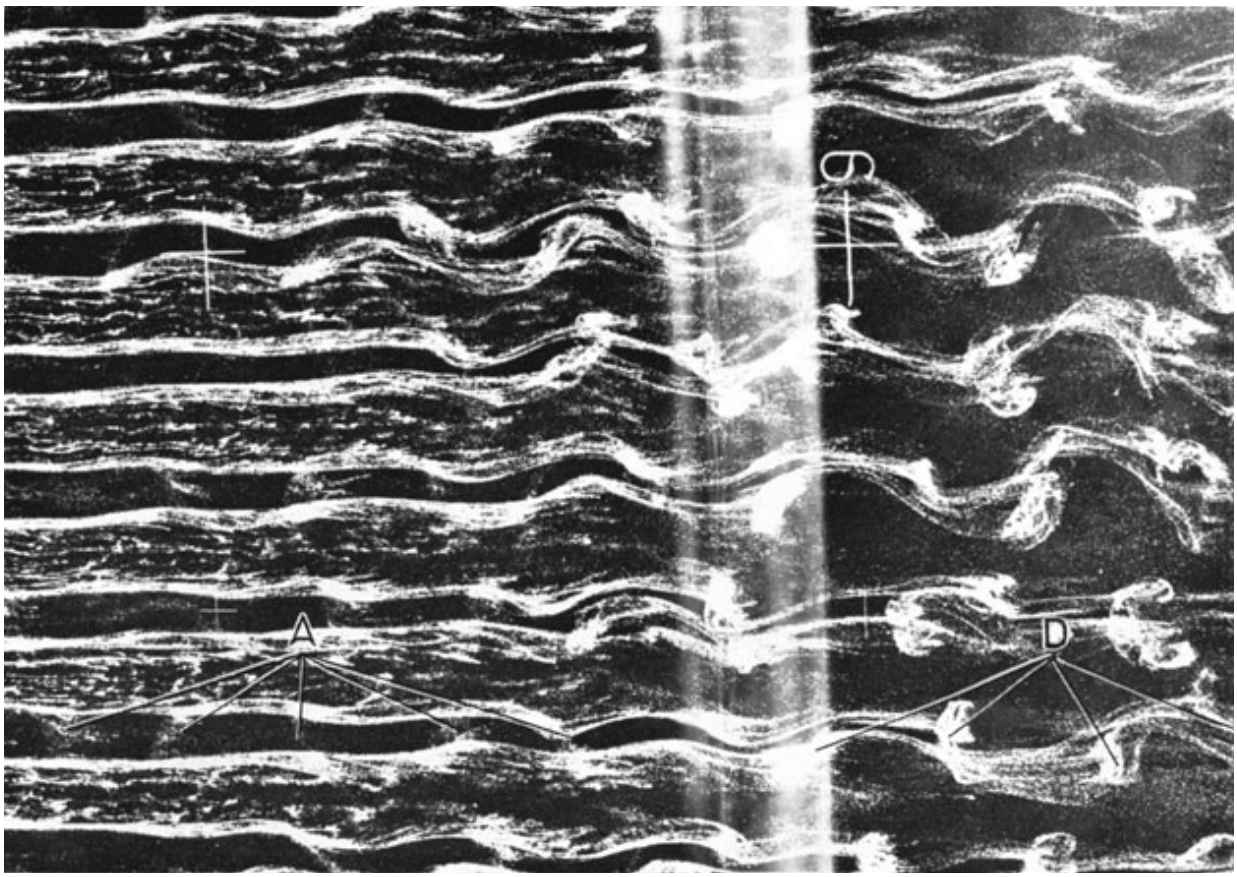

Figure 1.16: Secondary instability in the form of sinuous mode (Bippes 1972).

Liu (1994) arrived to the same conclusion by means of a global energy balance that showed that the sinuous mode is the dominant one. By performing a kinetic energy balance of the secondary perturbations, they showed that, for the sinuous mode, the energy-conversion mechanism from the primary motion to the secondary instabilities is mainly dominated by the dU/dz rate of shear strain, whereas of less importance is the effect of $dU/d\eta$. On the other hand, the varicose mode is more attributable to the energy-conversion mechanism associated with $dU/d\eta$. Viscous dissipation, though not large enough to overcome the production mechanisms, is nevertheless prominent in the global balance.

The development of secondary instabilities was also studied numerically by Li & Malik (1995). They realized that the odd mode is initially more unstable; however, the even mode has higher growth rates further downstream. They showed that the relative significance of these two secondary modes depends on the Görtler vortices wavelength, Λ, in such a way that the even mode is predominant for large wavelengths whereas the odd mode is predominant for short wavelengths. This conclusion explains why sometimes the Görtler vortices break down to turbulence through a meandering motion and sometimes by developing horseshoe vortices. Bottaro & Klingmann (1996) showed that the secondary instability is of

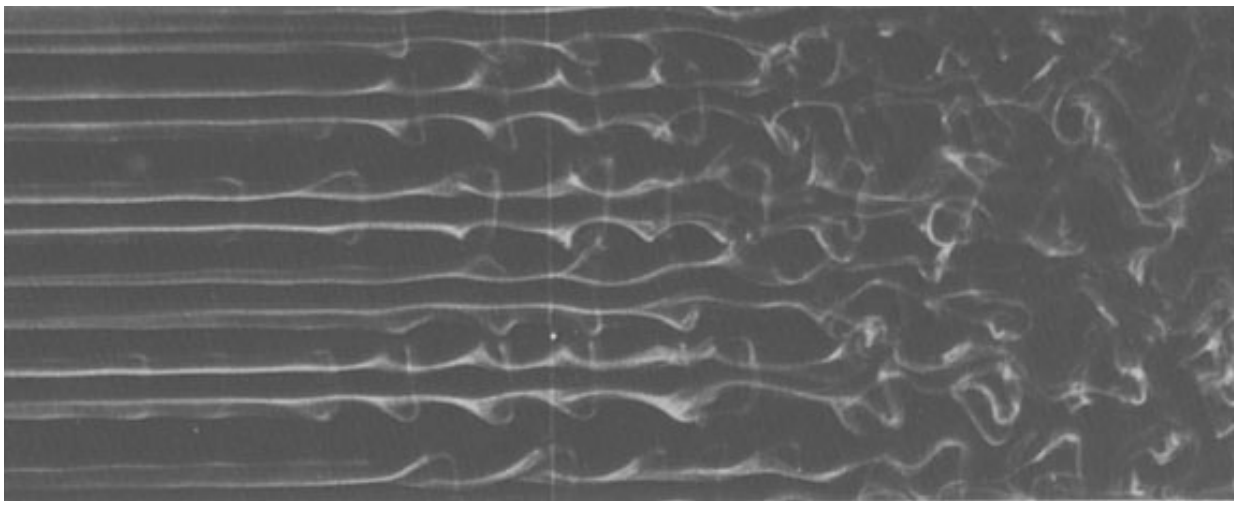

Figure 1.17: Secondary instability in the form of varicose mode (Aihara et al. 1985).

sinuous type at the onset, independently of the spanwise wavenumber. The onset coincides with the development of mushroom-like structures or more precisely with the appearance of an inflection point in the spawise-averaged velocity distribution. They also found out that the varicose mode rapidly acquires importance and may dominate the instability development when the spanwise wavenumber is large enough. This is due to the intensification of vertical shear close to the mushroom head. They also observed that the Reynolds number, Re, has only a minor influence on the sinuous mode, which implies that this secondary instability mechanism is mainly inviscid. On the other hand, for small spanwise wavelengths, the varicose mode becomes more unstable as Re progresses.

1.5.8 Streamwise development of the wall-shear stresses

As explained before, the initial basic flow, in the form of a 2D Blasius boundary layer, is clearly modified during the laminar-to-turbulent transition process. The Görtler vortices generate a wavy boundary layer in the spanwise direction resulting in thicker velocity profiles at the upwash location and thinner ones at the downwash location. This distorted flow also has an impact on the wall-shear stresses. Tandiono et al. (2009) measured experimentally the skin friction coefficient, C_f, at upwash and downwash locations and identified three regions based on its streamwise development, namely linear, nonlinear and transition to turbulence regions (see Figure 1.18). At first, C_f follows the Blasius solution but, after certain distance, the onset of the nonlinear region takes place and C_f departs from the laminar solution in such a way that it decreases at the upwash location (up to 59% of the Blasius value) and increases at the downwash location. Finally, in the third region, which is marked by the decay of the mushroom-like structure, C_f tends to converge to the same spanwise value. The same downstream evolution was observed experimentally by Swearin-

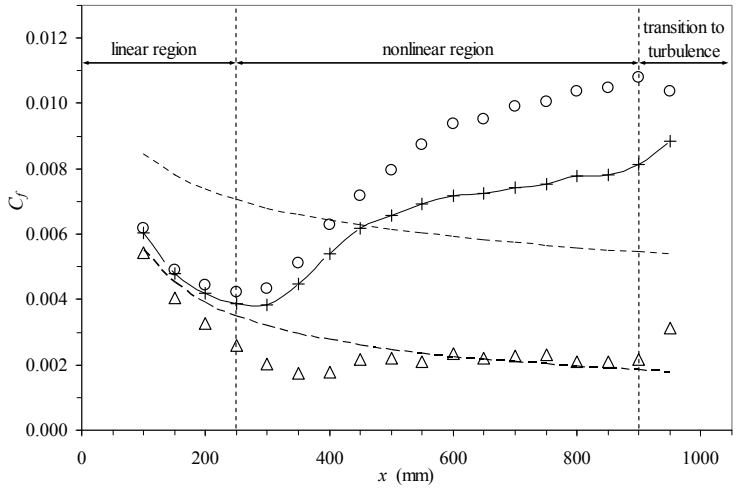

Figure 1.18: Streamwise evolution of the wall-shear stresses (Tandiono et al. 2009). Downwash (◯), upwash (△) and spanwise-average (+).

gen & Blackwelder (1987). Girgis & Liu (2006), by means of marching computations, studied the increase of skin friction caused by the Reynolds stresses of the secondary instabilities that modify the basic steady flow. They split their flow computation into a time independent mean flow and the time-dependent secondary instabilities that could be switched on and off. They showed that in the absence of the secondary instabilities, the spanwise-averaged skin friction due to the nonlinear steady Görtler flow can nearly bridge the transition from the laminar skin friction values to that of turbulent skin friction. On the other hand, when the secondary instabilities are included in the computation, an overshoot of C_f can be observed which increases well beyond the local turbulent values. This overshoot surpassing the theoretical turbulent flat-plate C_f values was also observed experimentally by Tandiono et al. (2009).

1.5.9 DNS of the transition process

There are two types of direct numerical simulations (DNS) of a transitional boundary layer: the spatial one and the temporal one. The spatial approach is the closest realization of a transition experiment, however, it is significantly more expensive than the temporal approach. Temporal DNS employ a local parallel flow assumption and the inflow/outflow boundary conditions are replaced by periodic boundary conditions. In order to study the effect of a growing boundary layer on transition, the computational box is allowed to move downstream at a speed close to the group speed of the instability waves, and the boundary layer grows in time. Temporal DNS has, thus, the main drawback of being unable to take into account the flow nonparallel effects (Guo et al. 1994).

A study of the Görtler flow development by means of temporal DNS can be found in the

work of Liu & Domaradzki (1993). They used the experimental parameters of Swearingen & Blackwelder (1987). However, they recognize that, with temporal DNS, the experimental results cannot be reproduced exactly because there is no one-to-one correspondence between their simulated temporally evolving flow and the experimental spatially evolving flow and also because of the parallel-mean-flow assumption. They observed the growth of the vortices and the development of the strong inflectional profiles which resulted in the development of secondary instabilities of sinuous and varicose types. Moreover, they performed a kinetic energy balance analysis finding that most of the production of perturbation energy at the start of the transition stage occurs in the large spanwise shear regions which reinforces the importance of high dU/dz regions in the transition process.

Very few spatial DNS studies of the Görtler flow development have been reported in the literature. The first spatial DNS study was recently reported by Schrader et al. (2011). They investigated the receptivity of the Görtler vortices to bump-dimple wall-roughness structures and to free-stream vortical modes. They found that receptivity is linear for both disturbances but free-stream vortical modes are more effective for generating high-amplitude Görtler modes. In a second part, the authors forced transition by generating free-stream turbulent intensity. This method set a flow field where steady Görtler vortices of several wavelengths (with average of $\Lambda = 273$) grew and merged among them before they broke down to turbulence. They also observed that transition can be speed-up by concentrating the turbulence intensity in the low-frequency range due to the excitation of travelling Görtler modes which saturate and break down before the steady Görtler rolls. For a detailed study of the unsteady travelling Görtler vortices, the reader can be referred to Boiko et al. (2010). However, Schrader et al. (2011) pointed out the fact that the most energetic turbulent eddies do not normally occur in the low-frequency range that excites travelling Görtler modes. Therefore, transition due to steady Görtler rolls is more likely to occur and normally prevails in experimental conditions.

Spatial DNS studies of the Görtler flow also include the work of Ducoin et al. (2017). The authors investigated the transition to turbulence occurring on the blade pressure side of a Savonius-style VAWT in static condition. In their study, the flow is disturbed using inlet random perturbations, which are convected through a semi-circular domain that is representative of a Savonius-blade geometry. They observed inception and development of Görtler vortices, which eventually cause the flow to transition (Figure 1.19 depicts the observed complete transition process). Furthermore, they compared their DNS results with URANS simulations finding that the average C_f along the domain was two times higher when computing the flow with DNS simulations. This is due to the development and breakdown of the longitudinal streaks that cannot be observed in the URANS computations; which highlights the necessity of accurate data coming from DNS computations of such geometry. Souza (2017) investigated the effect of imposing multi-frequency unsteady disturbances (pulses) on the development of secondary instabilities. An in-phase configuration excites the even (varicose) mode, whereas a phase shift of 90° excites the odd (sinuous) mode. Moreover,

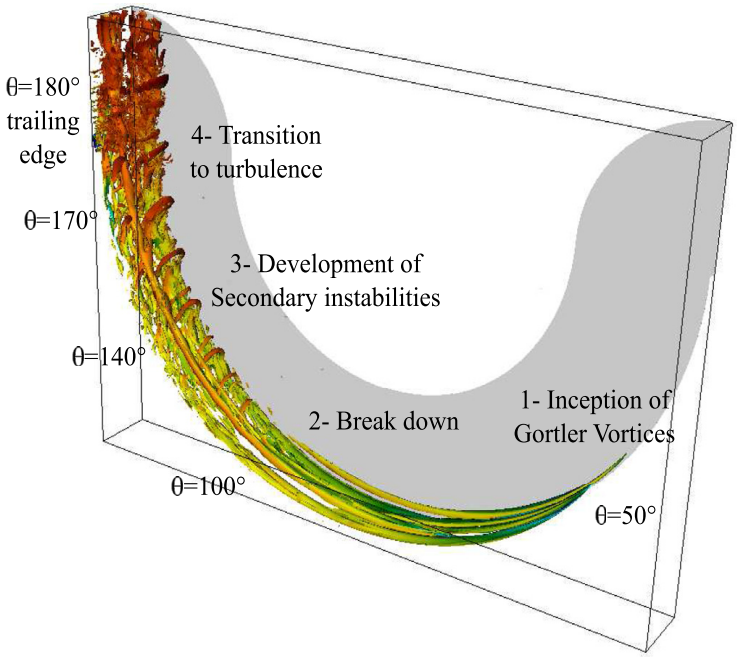

Figure 1.19: Vortical coherent structures observed during the transition process over the blade pressure side of a Savonius-style VAWT. Direct Numerical Simulation of Ducoin et al. (2017).

they observed that a phase shift of 45° excites both modes but the odd mode grows first and dominates the transition process. Sharma & Ducoin (2018) investigated the effect of inlet isotropic turbulence on the triggering of Görtler vortices. They observed that transition occurs earlier as the turbulence intensity increases ($Tu = 1\%$) and that a more random longitudinal-streak distribution in the spanwise direction occurs. On the other hand, a decreased turbulence intensity ($Tu = 0.1\%$) leads to a more uniform distribution of the streaks and to a larger transitional region. Malatesta et al. (2013, 2015) studied the influence of the Görtler vortices development on surface heat transfer by means of DNS. The authors observed that in the downwash region, where the boundary layer is compressed towards the wall, there is an increase in the heat transfer rate; whereas the opposite occurs in the upwash. Moreover, on the nonlinear region, the upwash region becomes narrow and, because of that, the spanwise-average heat transfer rate is higher than that for a Blasius boundary layer. They also found that they primary instability increases the spanwise average heat transfer to values above the turbulent ones, i.e. the spanwise-averaged Stanton number was reported to be 20% higher than the theoretical flat plate turbulent value. However, during the development of secondary instabilities, the heat transfer high rates are kept only in a short region before they decay to turbulent values downstream.

1.5.10 Fully turbulent flow

The fully turbulent is also subject to centrifugal effects, which can alter the turbulence structure as well as the flow statistical properties. These turbulence structure changes can be induced either by the wall curvature itself or by secondary flows that are generated in the form of longitudinal vortices (Görtler vortices). A review of the generation of Görtler vortices on the fully turbulent regime can be found on the work of Floryan (1991). From his review, the author concludes that the Görtler vortices are triggered from the most energetic eddies with motion consistent with the instability mechanism, that are normally present in the turbulent boundary layer, which are amplified as they convect downstream. A random distribution of the eddies leads to spanwise uniform turbulent statistics; however, upstream disturbances, such as screens, can lead to time-average spanwise variations because some vortex locations can become more probable than others. Also, the spanwise wavelength is usually two-times the boundary layer thickness; however, the spacing and amplitude are influenced by the initial disturbances. Another review of the turbulent boundary layer over a concave surface was performed by Piquet (2013). The author concluded that the concave curvature has a destabilizing effect which increases the levels of Reynolds shear stresses and of turbulence kinetic energy (TKE). Also, turbulence mixing is enhanced. Regarding the velocity profile, the author points out that it is fuller, compared to the flat plate case, and it tends to drop under the log-law and to remain below it. This feature is associated to the increased turbulence scale.

Jeans & Johnston (1983) studied experimentally the turbulent boundary layer over a concave curvature. In their experiment, the authors did not observe stationary roll-cells; instead, they observed that the vortices appear, wander about, merge, separate and disappear in a seemingly random manner without causing spanwise periodicity in the mean flow. Moreover, as the flow developed downstream, the author observed some effects of the longitudinal vortices. The mean velocity profile became fuller due to an increased mixing caused by the vortices. Besides, it was observed that the log-law region migrate away from the wall as the flow develops. Furthermore, turbulence intensity profiles indicated that additional turbulence is produced in the outer flow region. Similar conclusions were presented by Barlow & Johnston (1988). The authors observed an enhanced mixing across the boundary layer (compared to the flat plate case), bringing high-momentum fluid closer to the wall and causing a significant increase in the wall shear stresses. Besides, they measured increases in turbulence intensity, in the Reynolds shear stresses and in triple products across the outer layer, which were associated with the more energetic large-scale eddy structure. Furthermore, they observed that the triggered vortices have a strong influence on the flow structure in the near-wall region. However, when the local friction velocity is used for scaling, the Reynolds-averaged profiles show minor differences between the flat and concave cases. The authors included a visualization study of the randomly-appearing roll cells by means of the laser-induced-fluorescence technique. This structures could be seen with 2-

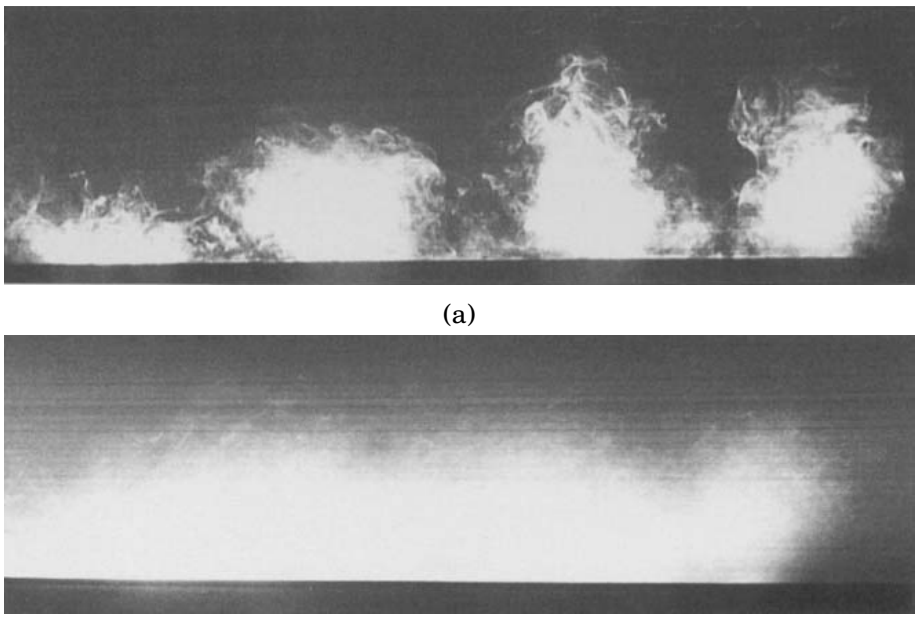

(a)

(b)

Figure 1.20: Laser-induced-fluorescence flow visualization of a turbulent boundary layer over a concave plate on a $\eta - z$ plane (Barlow & Johnston 1988). (a) 2-second exposure showing the random appearance of the transitory roll cells. (b) 60-second exposure showing a relative uniform distribution of the dye.

second exposure pictures (Figure 1.20a). However, with 60-second exposure pictures (Figure 1.20b), a more uniform distribution of the dye was observed because the vortices appear randomly in space and time covering completely the span. Barlow & Johnston (1985) observed that the spanwise-average skin friction coefficient of a turbulent boundary layer over a concave surface is 40% higher than that over a flat plate. The same increase was seen with naturally developing flow (with roll cells appearing randomly) or with the utilization of vortex generators that lock the spanwise location of the roll cells. Similar results were obtained by Meroney & Bradshaw (1975) who observed an increase of 20% in the spanwise-average skin friction coefficient of the concave surface turbulent boundary layer. Hoffmann et al. (1985) pointed out that a convex curvature has a stabilizing effect because it attenuates the pre-existing turbulence; on the other hand, a concave curvature has a destabilizing effect because it can lead to the generation of longitudinal (Görtler) vortices. Moreover, they presented vast turbulence measurements and showed that significant changes in the turbulence structure are induced both directly by the curvature and indirectly by the vortices. However, they deduced that the wall curvature effect is more important than the one of the vortices. This deduction led them to conclude that calculation methods representing the curvature effect, with spanwise averages to eliminate the vortex spanwise variations effects, may be quite satisfactory for engineering purposes.

Numerically, the turbulent boundary layer over a concave surface has been studied by

Moser & Moin (1987). They simulated a turbulent channel flow at $Re_x = 2990$ utilizing an incompressible DNS code with periodic boundary conditions in the streamwise and spanwise directions. They compared the convex and concave surfaces of the channel observing that many of the turbulence statistics of interest (turbulence intensities and root-mean-squared vorticity fluctuations) are the same on both sides of the channel when scaled in local wall variables. However, the most significant differences are in the Reynolds shear stress (with enhanced peaks for the concave side) and in their budget equation terms; skewness and flatness factors were also affected. Moreover, the authors attributed partially the turbulence structure difference to the appearance of Görtler vortices on the concave side which were considered to modify the wall-shear stresses as well. LES have also been used to study the fully turbulent regime. Lund & Moin (1996) simulated a spatially evolving incompressible turbulent boundary layer with $Re_\theta = 1300$ at the inlet in order to match the experimental conditions of Barlow & Johnston (1988). They found a good agreement with the experimental results on the velocity profiles which were found to become fuller due to the concave effect that enhances the mixing. However, for the Reynolds shear stress profiles, the simulation was only able to replicate qualitatively the experimental concave effects since the profiles peaks were slightly under-predicted. The authors related the difference to the sensitivity to the applied turbulent inflow conditions since a better agreement was obtained by using an inflow boundary condition with higher fluctuations and with artificially enhanced streamwise coherence. Formation of Görtler vortices was also visualized. Another LES study of a spatially developing turbulent boundary layer was presented by Arolla & Durbin (2015). A boundary layer with $Re_\theta = 1520$ at the inlet was imposed. The authors presented profiles of mean velocity and of turbulence statistics at different streamwise locations. They found that the effect of the concave curvature is largest on the wall-normal component of the Reynolds stress. The budget of the wall-normal Reynolds stress also confirmed this observation since an increase of the production term was clearly noticed as the flow moves farther into the concave curvature. Finally, they observed that the curvature effect is also large on the turbulent transport term of the turbulent-kinetic-energy budget, which is in agreement with earliest DNS observations (Moser & Moin 1987).

1.5.11 Surface heat transfer

Surface heat transfer and Görtler vortices are coupled phenomena in the sense that the evolution of the Görtler vortices is affected by the buoyancy forces while the additional flow motion related to the Görtler vortices also modifies the surface heat transfer.

The first mechanism, which is the buoyancy effect on the Görtler vortices development, was theoretically studied using LST by Garg & DiPrima (1984). The authors studied the effect of wall heating and cooling by extending the iso-thermal non-parallel LST study of Hall (1982); finding that, for the short-wavelength Görtler instability, the vortices can be significantly accelerated (the neutral stability curve occurs at a lower Görtler number) by heating the plate while the reverse occurs when cooling it. This destabilizing effect of heat-

ing on the Görtler instability was studied experimentally by Kamotani et al. (1985). The authors showed that the vortices amplitude increases with ΔT (where $\Delta T = T_w - T_\infty$; with T_w and T_∞ being the wall and free-stream temperatures, respectively) and, in terms of dimensionless numbers, the strength (or amplitude) increases with the ratio G_r/G_θ^2 (where G_r is the Grashof number, that is proportional to ΔT). Furthermore, they found that the vortices grow exponentially with the combined parameter $(G_\theta^2 + fG_r)^{1/2}$, where f is a constant, until the nonlinear effects become important. Regarding the temperature distribution, the authors observed that it follows a sinusoidal periodicity in the spanwise direction similar to the one of the velocity. Moreover, temperature profiles on the nonlinear region were measured finding similar distributions compared to the velocity ones, a fuller profile developed in the downwash while an inflectional S-shape developed in the upwash.

In fact, Liu & Sabry (1991) showed theoretically the similarity between heat, mass and streamwise-momentum for the nonlinear Görtler problem; which results in an analogy (i.e. equality) between the dimensionless temperature and concentration profiles and the dimensionless streamwise velocity profile, for Prandtl (Pr) and Schmidt (Sc) numbers of unity. This analogy also allows to draw conclusions about the local and spanwise averaged surface heat and mass transfer rates directly from the momentum problem results (i.e. the Nusselt number, Nu, and the Sherwood number, Sh, follow the same behavior as the skin friction coefficient). Later, Liu (2008, 2007) extended the analogy analysis for a flow with secondary instabilities and Prandtl number of unity showing that $St = C_f/2$, where St is the Stanton number. This implies that, similar to the C_f analysis of Girgis & Liu (2006), the nonlinear steady Görtler flow can nearly bridge the laminar St values with the higher turbulent ones. Also, that an overshoot beyond the turbulent St values occur due to an intensified heat transfer coming from the eddy heat flux effect of the secondary instabilities.

The second mechanism of the coupled phenomena, which is the effect of the swirl flow motion produced by the Görtler vortices on the surface heat transfer, has also been studied. McCormack et al. (1970) performed one of the first experimental analysis on the subject. They demonstrated that over a concave surface with presence of the vortices there is a significant increase of Nu of ~ 110% compared to a flat plate. Crane & Sabzvari (1989) experimentally studied the spanwise variations of the heat transfer coefficient finding that St at the downwash exceeds the value at the upwash by a factor as much as two to three. Moreover, the spanwise-averaged St was found to exceed the flat-plate value only after the nonlinear stage has set in. The authors related this heat transfer enhancement to the fact that the downwash region, where a local thinning of the boundary layer occurs, occupies a greater part of the span in the nonlinear phase. Later, Toe et al. (2002) distinguished three zones in the streamwise evolution of St: (i) a first zone where the Görtler vortices are weak and St follows the laminar solution; (ii) a second zone where St is constant (it does not vary with G_θ) and the Görtler vortices develop, amplify and saturate; and, (iii) a third zone, where St increases rapidly reaching values slightly higher than those of a flat plate turbulent boundary layer. Liu & Lee (1995) studied the heat transfer problem by means of

marching computations for Prandtl numbers different from unity. The case with $Pr = 0.72$, that simulates air in standard conditions, shows no significant differences from the $Pr = 1$ situation presenting less diffused mushroom-like structures in the iso-thermal plots. On the other hand, for the case with $Pr = 7.07$, that simulates water at standard conditions, the iso-temperature structures develop into thin, palm-tree-like structures. Moreover, it was found that the heat transfer rate, i.e. Nu, is significantly enhanced in both cases; about 400% higher than the flat-plate laminar value for $Pr = 7.07$ and about 340% for $Pr = 0.72$. It was also shown that the inlet velocity perturbation is an important controlling parameter for heat transfer enhancement. Momayez et al. (2004*a*,*b*) experimentally studied the effect of the Görtler vortices wavelength, Λ, on heat transfer enhancement by measuring St. They found that when Λ is closer to the zone of maximum linear amplification in the stability diagram, heat-transfer amplification is higher. Later, Momayez et al. (2009) analyzed the experimental data of the Stanton number streamwise evolution for several wavelengths, Λ, and free-stream velocities realizing that, when St is plotted against G_θ or Re_x, the curves do not collapse showing certain dispersion. Hence, the authors utilized a genetic algorithm in order to find a proper relation for the St streamwise evolution which was found to be of the form: $St = a(Re_\theta)^b(x/R)^c(\lambda/\theta)^d$, where a, b, c and d are correlation constants that depend on the streamwise transition region (linear, nonlinear, transition, turbulent).

The surface heat transfer enhancement caused by the Görtler vortices has also been studied by means of DNS, as it was explained in the section 1.5.9. Malatesta et al. (2013, 2015) found that the primary instability increases the spanwise average heat transfer to values above the turbulent ones (i.e. the spanwise-averaged St was 20% higher than the flat plate turbulent value). However, during the development of secondary instabilities, the heat transfer high rates are kept only in a short region before they decay to turbulent values downstream.

1.6 Scope of the present study

After discussing the existing literature on the subject, it is clear that, although comprehensive research investigations have been performed regarding the boundary layer development over a concave surface, there are still fundamental questions concerning the impact of various physical parameters on the onset of transition. Furthermore, the transition process role on the surface heat transfer enhancement has not been completely understood. Moreover, as pointed out previously, studies utilizing high-fidelity DNS, performed to completely characterize and analyze the transition phenomenon, are very scarce on the literature. Therefore, the present work mainly aims at numerically investigate, by means of DNS, the boundary layer transition over a concave surface in the presence of Görtler vortices and the physical parameters that play a role on it. Besides, the transition mechanisms that modify the thermal boundary layer and modify the heat transfer rate are also investigated. To that end, the following specific objectives have been defined:

1. To study and characterize the momentum boundary layer modification due the inception and growth of Görtler vortices throughout the different transition stages (linear, nonlinear and transition to turbulence).
2. To understand the local effect of the Görtler vortices on the streamwise evolution of the wall-shear stresses and on the boundary layer thicknesses at upwash and downwash locations, where the parameters present maxima and minima.
3. To study the effect of several physical parameters that can play a role on the onset of transition such as the radius of curvature, the vortices wavelength, the perturbation amplitude and streamwise location, and the wall-roughness perturbation geometry.
4. To analyse the thermal boundary layer modification due to the Görtler vortices swirl motion as well as the resultant surface heat transfer enhancement.
5. To study the Reynolds analogy between the streamwise-momentum and heat transfer problems for a flow over a concave plate with $Pr = 1$ throughout the whole transition process.
6. To analyse and characterize the fully turbulent regime (momentum and thermal boundary layers) product of the transition initiated by the Görtler vortices.

The present study will focus on the development of Görtler vortices with maximum amplification according to LST ($\Lambda = 250$). To that end, wall-roughness elements equally distributed in the spanwise direction are utilized in order to trigger the inception of Görtler vortices and to pre-set their spanwise wavenumber. Moreover, this excitation method allows to obtain a clear spanwise characterization of the streamwise streaks development and their breakdown into turbulence. Furthermore, for the thermal analyses, three different Prandtl numbers are considered ($Pr = 0.72$, $Pr = 1$ and $Pr = 7.07$) and the temperature is treated as a passive scalar.

1.7 Outline of the dissertation

In this doctoral thesis, the numerical results and the performed analyses of the laminar-to-turbulent transition of a boundary layer passing over a concave surface together with the parameters that play a role on its onset are documented. This documentation is organized as following:

Chapter 1: In this chapter, the general context and motivation that drove the present investigation are described. Moreover, an extensive literature review of the different aspects of the laminar to-turbulent transition of a boundary layer over a concave surface caused by the growth of Görtler vortices is presented. Furthermore, the scope and objectives of the present investigation are also described.

Chapter 2: This chapter elaborately describes the Fluid Mechanics governing equations as well as the numerical method (Spectral Element Method) employed by the utilized DNS code (NEK5000). The validation of the DNS solver and of the utilized numerical set-up (i.e. computational domain, boundary conditions, grid refinement and perturbation method) for a transitional flow over a concave surface is also presented.

Chapter 3: In this chapter, an extensive analysis and characterization of the complete laminar to-turbulent transition process over a concave surface using DNS is presented. The flow modification due to the Görtler vortices growth, evolution into secondary instabilities and the turbulence break-down of these, is also studied. The different regions encountered in the transition process, i.e., linear, nonlinear, transition and fully turbulent, are identified and characterized. Additionally, parametric studies showing the effect of several physical parameters (radius of curvature, the vortices wavelength, the perturbation amplitude and streamwise location, and the wall-roughness perturbation geometry) on the transition onset are presented. These results are published in: *Computers and Fluids* (Méndez et al. 2018).

Chapter 4: In this chapter, the thermal boundary layer development during the transition process is analyzed by treating the temperature as a passive scalar. Three different Prandtl numbers are studied: (i) $Pr = 1$, in order to verify the Reynolds analogy between heat and streamwise-velocity, (ii) $Pr = 0.72$, which corresponds to air at standard conditions, and (iii) $Pr = 7.07$, which corresponds to water at standard condition. The sudden increase of the surface heat transfer due the Görtler vortex swirl motion is analyzed. Furthermore, the characterization of a turbulent thermal boundary layer over a concave surface is presented.

Chapter 5: The summary of the performed research work along with the concluding remarks are given in this chapter. Moreover, for the future continuation of this research work, some possible points that can be addressed in the direction of better understanding the transition process over a concave surface are proposed.

Chapter 2
Numerical methodology and validation

2.1 Governing equations

The motion of a three-dimensional unsteady viscous flow is governed by a set of equations known as the **Navier-Stokes equations**. This set of coupled partial differential equations, that express conservation laws for mass, momentum and energy, describe how the flow velocity, pressure, temperature and density are related. For the current studies, their full incompressible form is utilized. A fluid is said to be incompressible when its density is constant (that is the case for low-velocity flows with Mach number lower than 0.3 since the density variation is less than 5%).

Using the incompressible assumption, the continuity (Eq. 2.1) and momentum (Eq. 2.2) equations become uncoupled from the energy equation (Eq. 2.4) and they are sufficient to determine the velocity and pressure fields. The incompressible Navier-Stokes equations in their dimensional form are, then, the following ones:

$$\nabla \cdot \mathbf{U} = 0, \tag{2.1}$$

$$\rho(\partial_t \mathbf{U} + \nabla \cdot \nabla \mathbf{U}) = -\nabla p + \nabla \cdot \tau + \rho \mathbf{f}, \tag{2.2}$$

where t is the time, p is the pressure, $\mathbf{f}$ accounts for the body forces such as gravity and τ is the viscous stress tensor, which is given by:

$$\tau = \mu[\nabla \mathbf{U} + \nabla \mathbf{U}^T]. \tag{2.3}$$

As mentioned, a computing advantage of the Navier-Stokes incompressible formulation is that the energy equation can be decoupled. This approach enables to solve the energy equation as complementary equation. This means that its solution is not necessarily needed to advance the flow and the temperature can be treated as a passive scalar. Therefore, after solving for the velocity, $\mathbf{U}$, and the pressure, p, fields using Equations (2.1) and (2.2), the temperature, T, field can be obtained by computing the conservation of energy equation:

$$\rho c_p(\partial_t T + \mathbf{U} \cdot \nabla T) = \nabla \cdot (k_{th} \nabla T) + q_{vol}, \tag{2.4}$$

where c_p is the fluid specific heat at constant pressure, k_{th} is the thermal conductivity and q_{vol} accounts for the volumetric heat sources.

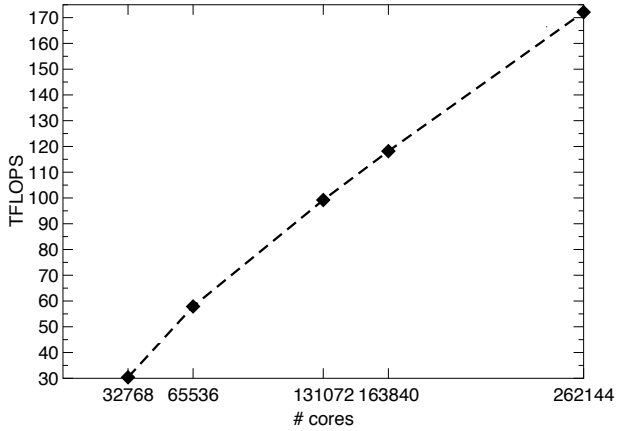

Figure 2.1: NEK5000 scaling study performed on Julich Supercomputing Centre's Blue Gene/P system (Mohr & Frings 2010). The plot shows a strong scaling (over 71% parallel efficiency) from 32,768 cores to 262,144 cores. The simulation was performed with 7.1 billion gridpoints.

2.2 Numerical solver (NEK5000)

In the current study, the full incompressible Navier-Stokes equations are solved using NEK5000, an open-source DNS code developed and maintained by Fischer et al. (2008), at the Argonne National Laboratory. This CFD solver was designed to simulate laminar, transitional, and turbulent incompressible or low Mach-number flows with the capacity of including heat transfer and species transport. As NEK5000 was developed to performed DNS, it is a well-suited code for performing scientific research and it is therefore used by several institutions world-wide in a broad range of applications, including the study of thermal hydraulics in nuclear reactor cores, the modeling of ocean currents, the simulation of combustion in mechanical engines and the analysis of transition to turbulence in vascular flows.

The NEK5000 solver consists of 100,000 lines of code that are mainly written in Fortran77 (70,000 lines of code), with the exception of the communication library written in C (30,0000 lines of code). Via Fortran programming, it allows to create user-defined modules and functions as well as to access and modify the code intrinsics. NEK5000 is optimized for parallel computing on distributed memory supercomputers by using a Message Passage Interface (MPI) programming model and domain decomposition. The code scales extremely effectively and an excellent scalability (higher than 70%) has been demonstrated on up to 262,144 processors producing more than 170TFlops, with problem sizes exceeding 7 billion grid-points (Mohr & Frings 2010) (see Figure 2.1). Moreover, the code won a Gordon Bell prize in 1999 for its algorithmic quality and outstanding sustained parallel performance.

2.2.1 NEK5000 spatial discretization

The Navier-Stokes equations are partial differential equations (PDE) that need to be spatially discretized to be solved numerically. NEK5000 employs a spatial discretization based on the Spectral Element Method (SEM), which was proposed by Patera (1984). The objective of using this method is to combine the best aspects of high-order spectral methods with finite element methods (FEM). SEM can thus benefit from the geometrical flexibility of the FEM, by splitting the computational domain into a series of smaller sub-domains (called spectral elements), along with the accuracy and exponential convergence of the spectral methods.

Using the SEM, NEK5000 divides the domain in a finite number E of hexahedral (brick) elements. Inside each element the solution and data are approximated by Nth-order tensor-product polynomials. Typical discretizations involve $E = 100$ to $10,000$ elements of order $N = 7$ to 15 (corresponding to 512 to 4096 nodal points per element). Within each spectral element, a local cartesian mesh is constructed that corresponds to $(N+1)^3$ Gauss-Lobatto-Legendre (GLL) collocation points where the Lagangre polynomial interpolants are defined (Figure 2.2 shows the GLL points distribution for two 2D cases with $N = 7$ and $N = 9$). The field dependent variables ($\mathbf{U}$, p, T) are expanded in terms of these Lagrangian interpolants through the GLL points; for instance, for the temperature, T, we have:

$$T^e(x_r, y_r, z_r) = \sum_{i=0}^{N} \sum_{j=0}^{N} \sum_{k=0}^{N} T^e_{ijk} \phi_i(x_r) \phi_j(y_r) \phi_k(z_r), \tag{2.5}$$

where the ϕ functions are the Nth-order Lagrangian interpolants, known as nodal basis functions. (x_r, y_r, z_r) are the coordinates of the reference element ($(x_r, y_r, z_r) \in [-1,1]^3$) onto which each spectral element e is mapped; and, T^e_{ijk} is the nodal spectral temperature coefficient. The spatial discretization is based on the weak form of the governing equations and follows the formulation $\mathbb{P}_N - \mathbb{P}_{N-2}$, proposed by Maday & Patera (1989), in which the pressure is solved in Gauss-Lobatto (GL) staggered points (with respect to the GLL points) and the pressure grid is of order $N-2$.

Regarding solution convergence, it can be reached by two methods. The first one is the p-refinement in which the SEM ensures exponential convergence for problems with smooth solutions as the mesh is refined by increasing the order of the polynomial N. An example of the p-refinement by increasing the polynomial order (which increases the number of GLL points per element) can be seen in Figure 2.2. The second strategy is the h-refinement in which the number of spectral elements E is increased. In this case the error is decreased algebraically like E^{-N}. Important is to notice that this second refinement type also allows for localized and adaptive refining of the computational domain (Feng & Mavriplis 2002). Moreover, the particular effect on the computational cost of each convergence refinement technique should be taken into account since the cost of a SEM 3D simulation is estimated to be of the order $O(EN^4)$ (Tufo & Fischer 1999).

For a detailed explanation of the SEM implementation in the NEK5000 DNS code, the

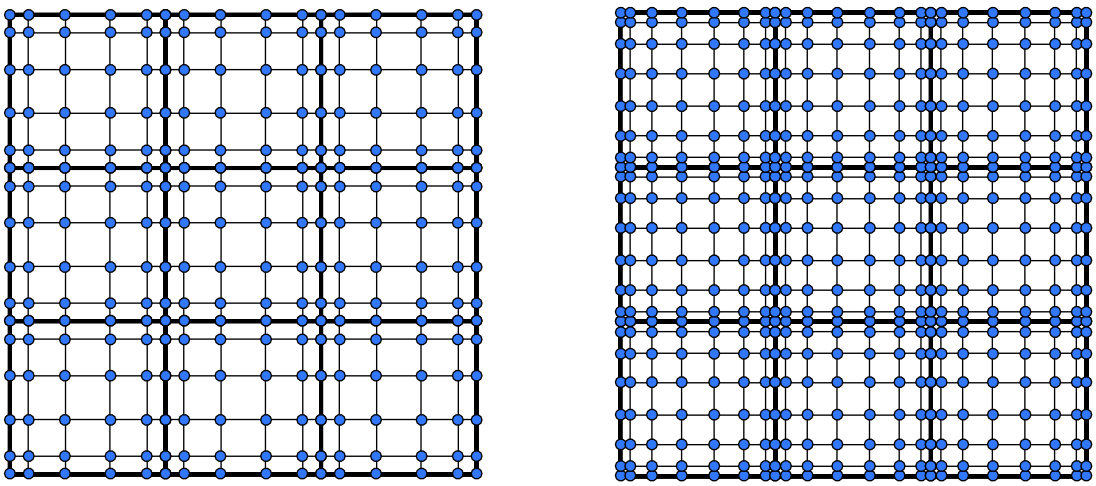

(a) (b)

Figure 2.2: Distribution of the GLL nodal points for a 2D mesh with 3×3 spectral elements, for two Nth order polynomials. (a) $N = 5$ with 36 GLL points per element. (b) $N = 7$ with 64 GLL points per element.

reader can be referred to the NEK50000 manuals and documentation, which can be found in Fischer et al. (2008).

2.3 Spectral element method theory

2.3.1 Galerkin method

The spectral element method is part of a family of approximation schemes based on the Galerkin method, or weighted residual method, for numerically solving PDEs. Other methods included in this family are the finite element method and the spectral method. PDEs discretized using this method have to be solved in what is known as the *weak form* or variational form.

2.3.1.1 Variational formulation

To introduce the Galerkin method, it will be applied to the simplest and most famous elliptic PDE, which is the Poisson equation. We have then that the one-dimensional (1D) Poisson problem subject to Dirichlet boundary conditions is:

$$\begin{aligned} -\nabla^2 u &= f \quad \text{in } \Omega, \\ u &= 0 \quad \text{in } \partial\Omega. \end{aligned} \tag{2.6}$$

The domain considered is $\Omega := x \in [a,b]$. Equation (2.6) is called the *strong form* of the Poisson equation. To obtain the weak form, the product of the strong form and a test function v_f belonging to a Sobolev space H_0^1 has to be integrated over the domain. We have then that:

$$-\int_\Omega v_f \nabla^2 u dx = \int_\Omega v_f f dx. \tag{2.7}$$

Integrating by parts the left hand side of Equation (2.7), we have that:

$$\int_\Omega \nabla v_f \cdot \nabla u dx - \int_{d\Omega} v_f \frac{du}{dn} \nabla u ds = \int_\Omega v_f f dx. \tag{2.8}$$

Since the boundary integral vanishes because of the Dirichlet boundary conditions, the Galerkin formulation reads: find $u \in H_0^1$, such that

$$\int_\Omega \nabla v_f \cdot \nabla u dx = \int_\Omega v_f f dx. \tag{2.9}$$

It can be noticed that the integration by parts helps to reduce the continuity requirements on u. A u that is once differentiable has to be found; which means that u has to be continuous but not necessarily ∇u.

2.3.1.2 Obtaining a set of equations

Once that the weak form (Eq. 2.9) has been obtained, we can start to discretize the problem and derive a system of equations. For that, we can now consider a set of $N+1$ basis functions $\phi_i(x)$ such that:

$$\begin{aligned} v_f &= \sum_{i=0}^{N} \phi_i(x) v_{f_i}, \\ u &= \sum_{j=0}^{N} \phi_j(x) u_j. \end{aligned} \tag{2.10}$$

Introducing these expansions of u and v_f into the weak formulation of the Poisson equation (2.9), we have that:

$$\sum_{i=0}^{N} \sum_{j=0}^{N} v_{f_i} \left(\int_\Omega \nabla \phi_i \cdot \nabla \phi_j dx \right) u_j = \sum_{i=0}^{N} v_{f_i} \int_\Omega \phi_i f dx. \tag{2.11}$$

Next, we can define the following parameters:

$$A_{ij} := \int_\Omega \nabla \phi_i \cdot \nabla \phi_j dx, \tag{2.12}$$

$$b_i := \int_\Omega \phi_i f dx, \tag{2.13}$$

$$\underline{v_f} := (v_{f_0}, v_{f_1}, ..., v_{f_N})^T, \tag{2.14}$$

$$\underline{u} := (u_0, u_1, ..., u_N)^T. \tag{2.15}$$

Using these parameters, the discrete Galerkin formulation reads: find $\underline{u} \in \mathbb{R}^{N+1}$, such that

$$\sum_{i=0}^{N}\sum_{j=0}^{N} v_{f_i} A_{ij} u_j =: \underline{v_f}^T A \underline{u} = \underline{v_f}^T \underline{b}, \tag{2.16}$$

which is equivalent to:

$$A\underline{u} = \underline{b}. \tag{2.17}$$

This is the system of linear equations that has to be solved for the basis coefficients, u_j, with A being an invertible matrix. The Galerkin method is basically a method of undetermined coefficients where there are $N+1$ unknown basis coefficients $[u_0, u_1, ..., u_N]$ and $N+1$ equations are generated by successively choosing the basis functions $[\phi_0, \phi_1, ..., \phi_N]$.

2.3.1.3 Extension to more complex PDEs

The Galerkin method is relatively straightforward to derive and it can be extended to more complex systems of PDEs. For instance, for a 1D non-linear convection-diffusion equation:

$$\frac{\partial u}{\partial t} + c\frac{\partial u}{\partial x} = \nu \frac{\partial^2 u}{\partial x^2}, \tag{2.18}$$

where c is a constant convection velocity, the procedure given above leads to the following system of equations:

$$M\frac{\partial \underline{u}}{\partial t} + cC\underline{u} + \nu A\underline{u} = 0, \tag{2.19}$$

where M is the mass matrix, C the convective operator and A is the stiffness matrix. M and C are defined as:

$$M_{ij} := \int_\Omega \phi_i \cdot \phi_j dx, \tag{2.20}$$

$$C_{ij} := \int_\Omega \phi_i \cdot \nabla\phi_j dx. \tag{2.21}$$

To this point, any method of the Galerkin family should follow the same derivation procedure. Hence, Equation (2.19) (or also Eq. 2.17 for a simpler system of PDEs) is the point of departure for the finite element, spectral element, and spectral formulations. These methods mainly vary in the choice of the basis functions ϕ_i and the way in which the integrals are solved. Noting that these choices influence the computational cost of the given problem.

2.3.2 Spectral element method

The main specific characteristics of the SEM are the utilization of orthogonal polynomials and of the Gauss quadrature method (a numerical approximation of the integral of a function). Orthogonality between basis functions is where the SEM greatly differs from the FEM. It will be assured due to the topological (local extension) and analytical nature of the chosen basis functions, ϕ.

The second specificity of the SEM is that the inner products appearing of the integrals of the stiffness (Eq. 2.12), mass (Eq. 2.20) and convective (Eq. 2.21) matrices are performed using Gauss quadrature. For SEMs, two implementations have been utilized which are based on Chebyshev and on Legendre polynomials. In both cases Lagrangian interpolation is used over a GLL quadrature grid for ensuring continuity of the solution. Chebyshev polynomials present the advantage of using fast transform techniques and the expected exponential accuracy on the solution for smooth problems has been proved. However, they have been abandoned and currently Legendre polynomials are more utilized due to their straightforward implementation. The basis functions ϕ_i utilized on NEK5000 are also based on Legendre polynomials; therefore, we will focus on them.

2.3.2.1 Domain decomposition and reference element

The method starts by partitioning the global integration domain $\Omega := [a,b]$ into several smaller E elements. Let Δ_E denote a partition of $[a,b]$:

$$\Delta_E : a = x_0 < x_1 < x_2 < ... < x_{E-1} < x_E = b. \tag{2.22}$$

We can define the local (element) domain by $\Omega^e := [x; x_{e-1} < x < x_e]$ with $1 \leq e \leq E$. Next, we can define a reference (or parent) element, with domain $\hat{\Omega} := [x_r; -1 \leq x_r \leq 1]$, onto which each spectral element Ω^e can be mapped. This mapping can be done using the following coordinate transformation:

$$x = x_{e-1} + \frac{h_e}{2}(x_r + 1), \tag{2.23}$$

where $h_e = x_e - x_{e-1}$ is the length of the element e.

The SEM procedure follows by introducing polynomial basis functions at the level of the reference element that will be later on mapped onto each interval Ω^e of Δ_E. The reference element basis functions are then the building blocks that will be then assembled together on Δ_E, element by element, to form a global basis.

2.3.2.2 Legendre polynomial and spectral basis

As mentioned, the spectral basis functions will be first defined on the reference element domain $\hat{\Omega} := [x_r; -1 \leq x_r \leq 1]$ onto which each spectral element Ω^e will be mapped later. Inside

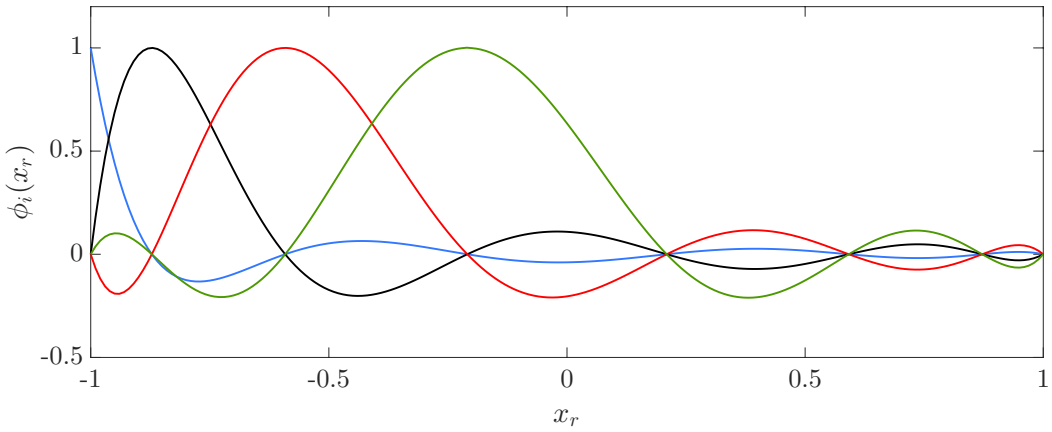

Figure 2.3: Example of the first four Legendre-spectral element basis functions for $N = 7$ ($L_7 = \frac{1}{16}(429x_r^7 - 693x_r^5 + 315x_r^3 - 35x_r)$). (—) ϕ_0, (—) ϕ_1, (—) ϕ_2 and (—) ϕ_3.

the reference domain $\hat{\Omega}$, we define the ordered set of $N+1$ GLL quadrature points as $\Xi_{N+1} = [x_{r_0}, x_{r_1}, ..., x_{r_N}]$. These nodal points are the roots of the following equation:

$$(1 - x_r^2)L'_N(x_r) = 0, \tag{2.24}$$

where L'_N is the derivative of the Legendre polynomial of degree N. The Lagrange interpolation polynomial of any function $u(x_r)$ on the GLL quadrature points is given by:

$$I_N u(x_r) = \sum_{j=0}^{N} u(x_{r_j})\phi_j(x_r), \tag{2.25}$$

where $[\phi_j(x_r)]_{j=0}^N$ is the associated interpolation spectral basis of degree N; with the basis elements given by:

$$\phi_j(x_r) = \frac{-1}{N(N+1)} \frac{(1 - x_r^2)L'_N(x_r)}{(x_r - x_{r_j})L_N(x_r)}, \quad 0 \le j \le N. \tag{2.26}$$

As an example, in Figure 2.3, the first four basis functions (Eq. 2.26) for a Legendre polynomial of degree $N = 7$ are plotted in the GLL quadrature points.

Based on the computed basis, $\phi_j(x_r)$, the spectral element approximation $u_N^e(x)$ of degree N in Ω^e can be mapped onto the reference element $\hat{\Omega}$:

$$u_N^e(x_r) = \sum_{j=0}^{N} u_j^e \phi_j(x_r), \tag{2.27}$$

where $(u_j^e)_{j=0}^N$ are nodal values of the unknown vector field u in Ω^e.

2.3.2.3 Gauss quadrature and local spectral element matrices

Next, using the mapping shown in Equations (2.23) and (2.27), it is possible to obtain local matrices for the stiffness (Eq. 2.12), mass (Eq. 2.20) and convective operator (Eq. 2.21) by mapping them from Ω^e onto the reference element $\hat{\Omega}$:

$$M^e_{ij} := \int_{\Omega^e} \phi_i(x) \cdot \phi_j(x) dx = \frac{h_e}{2} \int_{-1}^{1} \phi_i(x_r) \cdot \phi_j(x_r) dx_r, \tag{2.28}$$

$$A^e_{ij} := \int_{\Omega^e} \nabla\phi(x)_i \cdot \nabla\phi(x)_j dx = \frac{h_e}{2} \int_{-1}^{1} \nabla\phi(x_r)_i \cdot \nabla\phi(x_r)_j dx_r, \tag{2.29}$$

$$C^e_{ij} := \int_{\Omega^e} \phi(x)_i \cdot \nabla\phi(x)_j dx = \frac{h_e}{2} \int_{-1}^{1} \phi(x_r)_i \cdot \nabla\phi(x_r)_j dx_r. \tag{2.30}$$

Once that the matrices have been mapped onto the reference element, their integrals can be evaluated using the Gauss quadrature method. This is an exact method of a quadrature for a polynomial of degree $2N-1$ or less; with $N+1$ number of points over which the integral is evaluated. Hence, for a function $f(x)$ we have:

$$\int_{-1}^{1} f(x) dx \equiv \sum_{k=0}^{N} \rho_k f(x_{r_k}), \tag{2.31}$$

where $(x_{r_k})_{k=0}^{N}$ denotes the roots of an orthogonal polynomial which in this case is the derivative of a Legendre polynomial L'_N (whose roots are obtained with Eq. 2.24). ρ_k are the quadrature weights given by:

$$\rho_k = \frac{2}{N(N+1)} \frac{1}{[L_N(x_{r_k})]^2}. \tag{2.32}$$

Due to the use of GLL points, the Gauss quadrature can thus assure exact integration (up to machine precision) of the integrals presented on the mass (Eq. 2.28), stiffness (Eq. 2.29), and convective operator matrices (Eq. 2.30). Hence, applying Gauss quadrature, for the mass matrix we have that:

$$M^e_{N,ij} := \frac{h_e}{2} \sum_{k=0}^{N} \rho_k \phi_i(x_{r_k}) \cdot \phi_j(x_{r_k}) = \frac{h_e}{2} \rho_i \delta_{ij}, \tag{2.33}$$

since $\phi_i(x_r) \cdot \phi_j(x_r) = \delta_{ij}$; where δ_{ij} is the identity matrix. The mass matrix is then a diagonal matrix which holds the weights of the quadrature rule on the diagonal. For the stiffness matrix, we have that:

$$A^e_{N,ij} := \frac{h_e}{2} \sum_{k=0}^{N} \rho_k \nabla\phi(x_{r_k})_i \cdot \nabla\phi(x_{r_k})_j = \frac{h_e}{2} \sum_{k=0}^{N} \rho_k D_{N,ki} D_{N,kj}, \tag{2.34}$$

where $D_{N,ij}$ is the differentiation matrix given by:

$$D_{N,ij} := \left.\frac{d\phi_j}{dx_r}\right|_{x_r=x_{r_i}} \begin{cases} \dfrac{L_N(x_{r_i})}{L_N(x_{r_j})}\dfrac{1}{x_{r_i}-x_{r_j}}, & i \neq j, \\ -\dfrac{(N+1)N}{4} & i=j=0, \\ \dfrac{(N+1)N}{4} & i=j=N, \\ 0 & \text{otherwise.} \end{cases} \tag{2.35}$$

The elements of $D_{N,ij}$ are the nodal values of the first derivative of the GLL interpolation polynomials (Eq. 2.26). For the convective operator matrix, we have that:

$$C^e_{N,ij} := \frac{h_e}{2}\sum_{k=0}^{N}\rho_k\phi(x_r)_i\cdot\nabla\phi(x_r)_j = \frac{h_e}{2}\sum_{k=0}^{N}\rho_k\phi(x_r)_i D_{N,kj}. \tag{2.36}$$

2.3.2.4 Assembly of the global matrices

Once that the local matrices have been obtained, it is possible to assemble the contribution of all the elements Ω^e to the global matrices through the application of the *direct stiffness summation method*. This is an element-by-element process of fetching and summing where the individual contributions are entered into the appropriate components of the global matrices and continuity between the adjacent elements is ensured. The details of the method are outside of the scope of this SEM introduction and the reader can be referred to Deville et al. (2002) for further details. Applying this method, we can obtain the algebraic system of equations that governs the spectral-element solution:

$$\mathbf{M}\frac{\partial \underline{\mathbf{u}}}{\partial t} + c\mathbf{C}\underline{\mathbf{u}} + \nu\mathbf{A}\underline{\mathbf{u}} = 0. \tag{2.37}$$

In this system of equations, $\underline{\mathbf{u}}$, which is composed of $EN+1$ components, has to be found. The structure of the global stiffness $\mathbf{A}$ and mass $\mathbf{M}$ matrices (for a partition into three spectral elements with $N = 7$) resulting from the direct stiffness summation method is shown in Figure 2.4. As seen, the stiffness matrix $\mathbf{A}$ exhibits a block-diagonal structure, whereas the mass matrix $\mathbf{M}$ presents a diagonal structure resulting from the Gaussian quadrature integration method.

Once that the algebraic system of equations has been derived by assembling the global matrices, it can be solved in order to find the unknown vector $\underline{\mathbf{u}}$ and the SEM procedure can be considered to end up at this point. The main characteristics of the spectral element method, together with their utilized mathematical tools (Galerkin method, Gauss quadrature, etc.), have been presented here. In order to thoroughly review the details of the SEM, the reader can be referred to Deville et al. (2002) and to the SEM and Galerkin method documentation for the NEK5000 code found in Fischer et al. (2008).

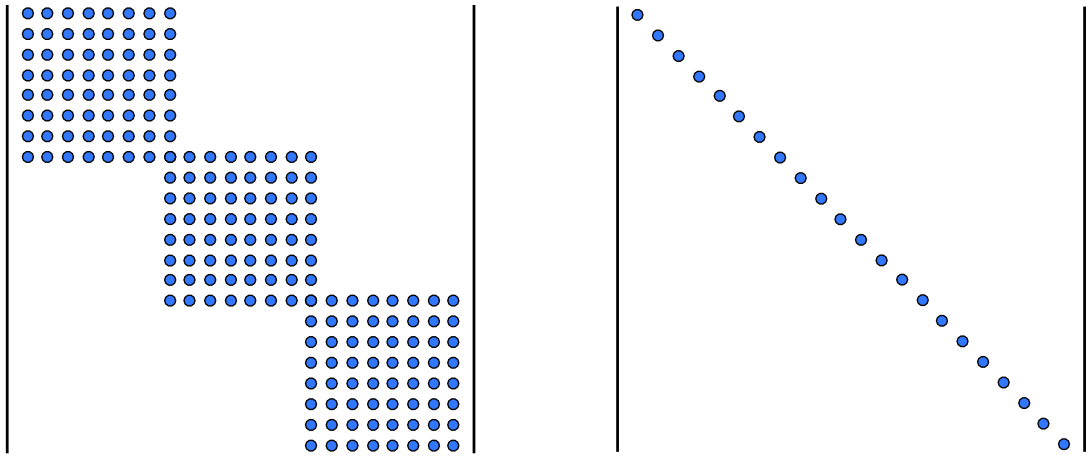

(a) (b)

Figure 2.4: Structure of the global matrices for $E = 3$ and $N = 7$. (a) Stiffness matrix $\mathbf{A}$. (b) Mass matrix $\mathbf{M}$.

2.4 Time integration

In order to compute the flow field at a later time step in NEK5000, the time integration is done using an implicit-explicit method (IMEX). The convective terms are computed explicitly (i.e. only data from the current time steps is used) by using a third-order extrapolation scheme (EXT) whereas the diffusion terms are treated implicitly (i.e. data from both the current and the later time step are used) with a third-order backward differentiation scheme (BDF).

Considering thus the convection-diffusion equation obtained from the SEM approach:

$$M \left.\frac{\partial u}{\partial t}\right|_{t^{n+1}} + cC\, u|_{t^{n+1}} + \nu A\, u|_{t^{n+1}} = 0, \tag{2.38}$$

where the superscript $n+1$ indicates the new time-level (e.g. t^{n+1}). By discretizing with the IMEX method, we have that:

$$\sum_{j=0}^{k_t} \frac{b_j}{\Delta t} M u^{n+1-j} + \sum_{j=1}^{k_t} a_j c C u^{n+1-j} + \nu A u^{n+1} = 0, \tag{2.39}$$

where Δt is the time step, k_t the order of the EXT and BDF schemes; and, a_j and b_j the schemes coefficients. Next, the first coefficient of the BDF scheme, b_0, is taken out of the

summation. This leads to:

$$\frac{b_0}{\Delta t}Mu^{n+1} + \nu Au^{n+1} = -\sum_{j=1}^{k_t} a_j cCu^{n+1-j} - \sum_{j=1}^{k_t} \frac{b_j}{\Delta t}Mu^{n+1-j}. \tag{2.40}$$

The equation can be further simplified to:

$$H_o u^{n+1} = -\Delta t cC \sum_{j=1}^{k_t} a_j u^{n+1-j} - M \sum_{j=1}^{k_t} b_j u^{n+1-j}, \tag{2.41}$$

where we have introduced the Helmholtz operator $H_o := b_0 M + \Delta t \nu A$; and the system can now be solved for the flow field at the new-time level u^{n+1}. For the third-order scheme case ($k_t = 3$):

$$H_o u^{n+1} = -\Delta t cC(3u^n - 3u^{n-1} + u^{n-2}) - M\frac{-18u^n + 9u^{n-1} - 2u^{n-2}}{6}, \tag{2.42}$$

with $H_o = \frac{11}{6}M + \Delta t \nu A$.

The truncation error of using this BDF/EXT scheme is of the order $O(\Delta t^3)$. The reason of choosing an explicit scheme for treating the convective terms is the fact that it avoids the solution of a non-linear non-symmetric system of equations every time step. However, it enforces a temporal constraint that limits the size of Δt in order to obtain stability. This stability restriction (Courant condition) reads:

$$\Delta t < CFL \cdot \min\left\{\frac{\Delta x}{u}, \frac{\Delta y}{v}, \frac{\Delta z}{w}\right\}, \tag{2.43}$$

where CFL is the Courant number (also known as the Courant-Friedrichs-Lewy number); which is set to $CFL \approx 0.5$ in NEK5000 in order to ensure stability.

For further details about the time integration method used in NEK5000, the reader is referred to its documentation (Fischer et al. 2008).

2.5 Validation

2.5.1 Previous validation studies of NEK5000

As previously mentioned, NEK5000 is a well-validated DNS code that is used for a large range of applications. As such, it has been widely used and validated for the case of flow undergoing laminar-to-turbulent transition as well as in fully turbulent regime for the three canonical flows, namely: flat plate, channel and pipe flow.

The transitional boundary layer over a flat plate has been investigated by several authors who have also validated the NEK5000 code results. Fischer & Choudhari (2004) validated the code for this test case by exciting TS waves (at a dimensionless frequency $F = 70 \times 10^{-6}$ with a suction-blowing strip at $Re_x = 0.5 \times 10^6$) and comparing their propagation with the one predicted theoretically with LST obtaining a perfect agreement (see Figure 2.5). More-

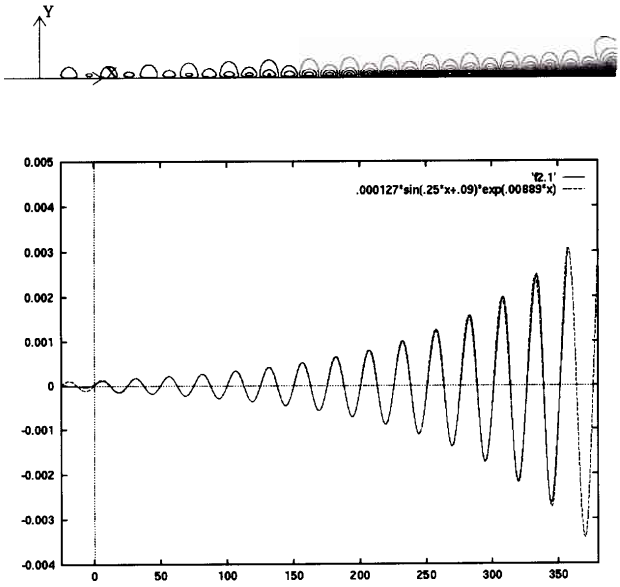

Figure 2.5: Validation of the spectral element code NEK5000 for Tollmien-Schlichting wave propagation ($F = 70 \times 10^6$). Top: contours of v downstream of source (an unsteady suction-blowing strip at $Re_x = 0.5 \times 10^6$). Bottom: Magnitude of v versus x at $y = 1$, compared with linear stability theory (dashed line). Study performed by Fischer & Choudhari (2004).

over, the transient growth induced by roughness elements was studied and the results were compared with experimental ones (White & Ergin 2003). Good agreement was found for the root-mean-squared (rms) disturbance amplitudes as well as for the evolution of the modal energy on the dominant Fourier components. Schrader et al. (2010) studied the receptivity to free-stream vorticity of flow past a flat plate. The authors validated their simulations by comparing some of their results with a parabolized stability equations (PSE) theoretical model, which was developed (and validated by comparing with experimental results) by Bertolotti & Kendall (1997). A comparison of the growth and decay of an excited TS wave (with frequency $F = 96$) was done finding a good agreement in terms of streamwise rms disturbance amplitude. Besides, the disturbance modal evolution of a perturbed boundary layer (excited with axial free-stream vorticity at $F = 0$) was compared finding also a good match. Shahriari et al. (2016) studied the receptivity to acoustic waves of flow past a flat plate finding an excellent agreement of the computed receptivity coefficients with previous DNS results (Murdock 1980) as well as with theoretical results (Giannetti & Luchini 2006, Turner 2012).

The turbulent channel flow has also been investigated and validated using NEK5000. Sprague et al. (2010) performed a code validation by comparing the computed turbulence statistics with previous DNS results (Kim et al. 1987) at $Re = 2800$ (based on the mean center-line velocity, U_m, and the channel half-width). Using a polynomial order $N = 7$, excellent agreement was found for the time-average streamwise velocity profile (with normalized

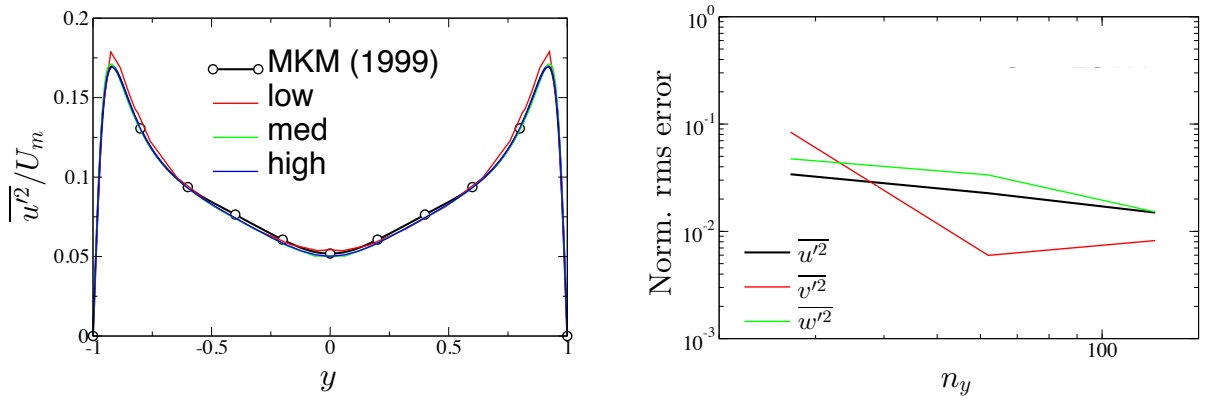

(a) (b)

Figure 2.6: Mesh convergence study for a fully turbulent channel flow at $Re = 2800$ using NEK5000 performed by Sprague et al. (2010). (a) Profile of the Reynolds stress $\overline{u'^2}$ for three meshes with different resolution (low: $n_y = 29$; med: $n_y = 64$; high: $n_y = 127$; where n_y is the number of nodal points in the wall-normal direction). They are compared with the DNS benchmark results of Moser et al. (1999). (b) Decrease of the normalized rms error for the Reynolds stresses ($\overline{u'^2}$, $\overline{v'^2}$, $\overline{w'^2}$) as n_y is increased.

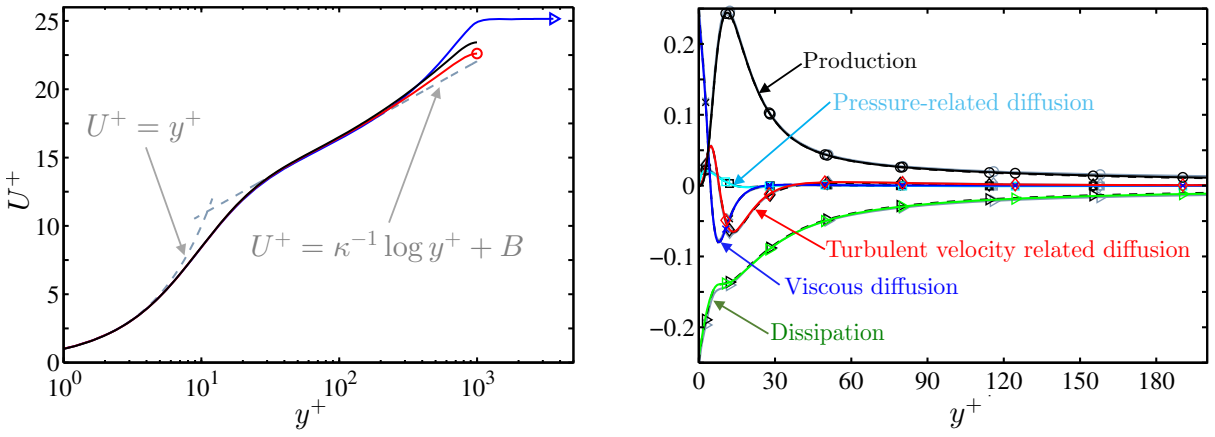

(a) (b)

Figure 2.7: Validation of the fully turbulent flow inside a pipe at $Re_\tau = 1000$ using NEK5000 performed by El Khoury et al. (2013). The results are compared with previous DNS studies of a turbulent channel flow (Lenaers et al. 2012) and a turbulent boundary layer over a flat plate (Schlatter & Örlü 2010). (a) Profile of mean streamwise velocity, U^+. (——) Pipe (El Khoury et al. 2013), (——) channel (Lenaers et al. 2012), (——) flat-plate (Schlatter & Örlü 2010). (b) TKE budget normalized by u_τ^4/ν. The profiles of the three cases collapse and are indistinguishable. (——) Pipe (El Khoury et al. 2013), (- - -) channel (Lenaers et al. 2012), (——) flat-plate (Schlatter & Örlü 2010).

rms error of order $O(10^{-3})$) as well as for the Reynolds stresses profiles (normalized rms error of order $O(10^{-2})$). Some of the results are shown in Figure 2.6. A similar study was done by Ohlsson et al. (2011) who compared their turbulent channel simulations at $Re_\tau = 180$ with previous DNS results of Moser et al. (1999). Re_τ being the Reynolds number based on the channel half-width and on the wall-friction velocity, u_τ. Using $N = 7$ and a h-type refinement technique in which the spectral elements number is increased, the authors found that, when grid convergence is reached, an excellent agreement of velocity profiles, Reynolds stresses and pressure fluctuations is obtained.

Furthermore, the turbulent pipe flow has also been studied using NEK5000. El Khoury et al. (2013) simulated the flow at $Re_\tau = 180, 360, 550$ and 1000 in order to compare the mean statistics with previous DNS studies (Lenaers et al. 2012, Schlatter & Örlü 2010). Using $N = 7$, the mean velocity profile collapsed well in both the viscous sub-layer and the log-law region. Moreover, the TKE budget was also compared finding out that at $Re_\tau = 1000$ the budgets of the three canonical cases (boundary layer, channel and pipe flows) are indistinguishable. The results are shown in Figure 2.7.

These previous studies lead to conclude that NEK5000 is well validated for the canonical flow cases under transitional and fully turbulent conditions. Moreover, the transitional flow over a concave plate has also been studied using NEK5000. Schrader et al. (2011) utilized it to compute receptivity coefficients for wall-roughness and free-stream vorticity perturbations. Ducoin et al. (2017) studied the transition over the geometry of a Savonius-style VAWT which resembles a concave surface geometry (with some differences such as the blunt leading and trailing edges) by perturbing the flow with free-stream turbulence intensity. Moreover, Sharma & Ducoin (2018) studied the effect of high and low free-stream turbulence intensity on the transition onset over a concave plate.

For the validation study of the current work (Section 2.5.3), some of the obtained results of the transitional boundary layer over a concave surface will be compared with the DNS reference data of Schrader et al. (2011) due to the fact that the same perturbation method (wall-roughness) was employed.

2.5.2 Simulation set-up

Flow properties and computational domain

The development of a boundary layer over a concave surface is investigated using the DNS SEM code NEK5000. The flow is considered to be incompressible (constant density) and it is simulated with a free-stream velocity of $U_\infty = 2.85$ m/s and kinematic viscosity $\nu = 1.5 \times 10^{-5}$ m^2/s in order to match both the numerical conditions of Schrader et al. (2011) and the experimental set up of Tandiono et al. (2009). To that end, a 3D computational domain (shown in Figures 2.8 and 2.9) is designed with an outer radius of $R = 1$ m, an inner radius $R_i = 0.9$ m, an arc length of $\Phi = 180°$ and a spanlength $L_z = 0.048$ m. Compared to the reference study (Schrader et al. 2011), the current domain is 4 and 2.67 times larger in the

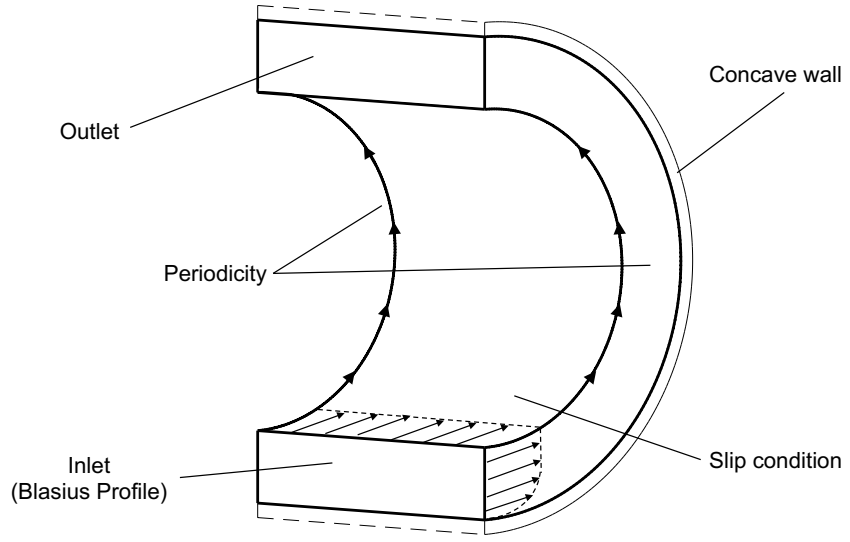

Figure 2.8: Sketch of the computational domain together with the utilized boundary conditions.

spanwise and streamwise directions, respectively. This allows to compute three more pairs of Görtler vortices (four in total) and helps characterizing how they transition and break down into turbulence. Besides, since the boundary layer thickness at the inlet is $\delta_{in} = 3 \times 10^{-3}$ m, the domain dimensions are $L_\xi/\delta_{in} = 1054.1$, $L_\eta/\delta_{in} = 33.6$ and $L_z/\delta_{in} = 16.1$; where L_ξ, L_η and L_z are the lengths in the streamwise ξ, wall-normal η and spanwise z directions, respectively.

Boundary and initial conditions

Regarding the boundary conditions, a laminar Blasius profile with $Re_\xi = 1.33 \times 10^4$ is imposed at the inlet. At the outer radius surface, a wall boundary condition is imposed (no slip condition, $\mathbf{U} = 0$), whereas, at the inner radius, a tangential velocity, U, equal to the free-stream velocity, U_∞, is imposed. At the exit, an outflow boundary condition was prescribed, where the normal stresses are zero. Moreover, the computational domain is considered to be periodic in the spanwise direction. Regarding the initial condition ($t = 0$), the two-dimensional Blasius flow solution is computed and imposed along the concave plate.

Domain discretization

With respect to the grid, the results presented in the current study have been obtained using a polynomial order $N = 7$ and a total number of spectral elements of $E = 43200$ which resulted in a total number of GLL nodal points of $N_t \approx 1.5 \times 10^7$. The spectral elements were distributed as $n_\xi \times n_\eta \times n_z = 240 \times 15 \times 12$, where n is the number of elements in each axial direction (ξ, η, z). This corresponds to an average space resolution of $\Delta\xi^+ \times \Delta\eta^+ \times \Delta z^+ = 19.1 \times 0.55 \times 5.8$ in viscous units of the next-to-wall GLL nodes at the inflow. A two-dimensional cut-view (near the inlet) of the numerical domain used for the current studies is shown in

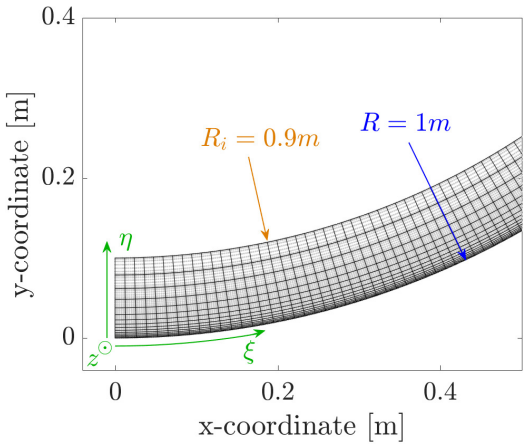

Figure 2.9: 2D cut-view of the numerical domain showing the spectral element distribution: $n_\xi \times n_\eta \times n_z = 240 \times 15 \times 12$; as well as the GLL nodal points for $N = 7$. Here the axes, ξ, η and z are oriented in the streamwise, wall-normal and spanwise directions, respectively.

Figure 2.9. The spectral element distribution and the polynomial order employed are based on the reference study (Schrader et al. 2011).

Perturbation method

In order to excite the Görtler vortices, and to break down the laminar inherence of the imposed Blasius flow, a perturbation is needed. For this study, the flow perturbation is imposed by means of wall-roughness elements equally distributed along the spanwise direction and located close to the inlet. The spanwise of the roughness elements presets the Görtler vortices wavelength λ and is selected for obtaining a normalized wavelength parameter $\Lambda = 250$, where Λ was defined in Eq. (1.25): $\Lambda = \frac{U_\infty \lambda}{\nu}\sqrt{\frac{\lambda}{R}}$.

The value of $\Lambda = 250$ is selected in order to trigger the Görtler vortices with maximum growth rate; which, according to linear stability theory, occurs when Λ is in the range of $200 - 270$ (see Section 1.5.3.1 and 1.5.5). Additionally, a non-dimensional wavelength of $\Lambda = 250$ has also been preset in the experimental studies of Mitsudharmadi et al. (2004) and Tandiono et al. (2008, 2009) as well as in the numerical receptivity studies of Schrader et al. (2011).

Four bump-dimple elements with a smooth sinusoidal shape have been placed on the concave plate with their center located at the streamwise location $\xi = 0.02618$ m, which corresponds to an angular location of $\phi_{loc} = 1.5°$ from the inlet. Regarding the wall-roughness elements height, h, the baseline case utilized for the transition analysis uses a series of bump-dimple structures with $h = 0.01\delta^*$, where δ^* is the boundary layer displacement thickness at the center location of the wall-roughness elements. The geometry of one spanwise wavelength of the wall-roughness elements is shown in Figure 2.10.

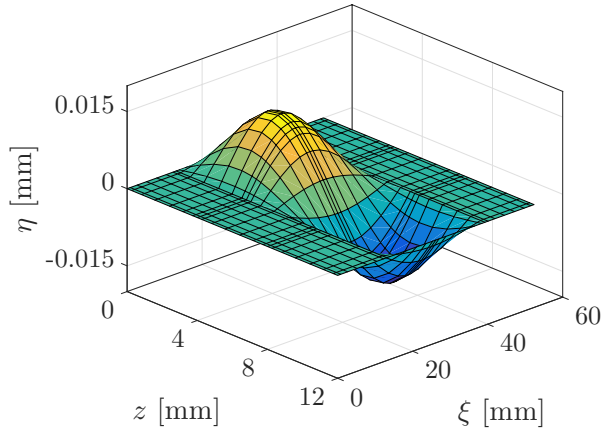

Figure 2.10: Roughness element utilized for the excitation of the Görtler vortices with a height of $h = 0.01\delta^*$.

2.5.3 Validation of the results

Since the code has been largely validated for the transitional and turbulent flow, this section is mostly based on verifying the correctness of the utilized grid, domain and boundary conditions. For that, a mesh convergence study is performed by comparing the results of three grids constructed with a different polynomial order (N = 5, 7 and 9). The characteristics of the tested meshes are shown in Table 2.1.

Grid	N	$n_\xi \times n_\eta \times n_z$	N_t	$\Delta\xi^+ \times \Delta\eta^+ \times \Delta z^+$
A	5	$240 \times 15 \times 12$	5.57×10^6	$26.7 \times 1.00 \times 8.1$
B	7	$240 \times 15 \times 12$	1.51×10^7	$19.1 \times 0.55 \times 5.8$
C	9	$240 \times 15 \times 12$	3.20×10^7	$14.5 \times 0.34 \times 4.5$

Table 2.1: Characteristics of the SEM grids used for the validation and mesh convergence studies. N is the polynomial order; $n_\xi \times n_\eta \times n_z$ are the number of spectral elements in each axial direction (ξ, η, z); $N_t = (n_\xi N + 1)(n_\eta N + 1)(n_z N + 1)$ is the total number of GLL points; and, $\Delta\xi^+ \times \Delta\eta^+ \times \Delta z^+$ is the average space resolution in viscous units at the inflow.

For comparing the results of the different meshes, two different validation studies are performed. In the first one, the base flow is computed (no perturbation is used) and the obtained results are compared with the theoretical Blasius solution. In the second one, the boundary layer response to localized wall-roughness elements with $h = 0.01\delta^*$ is computed and compared with the reference DNS data of Schrader et al. (2011).

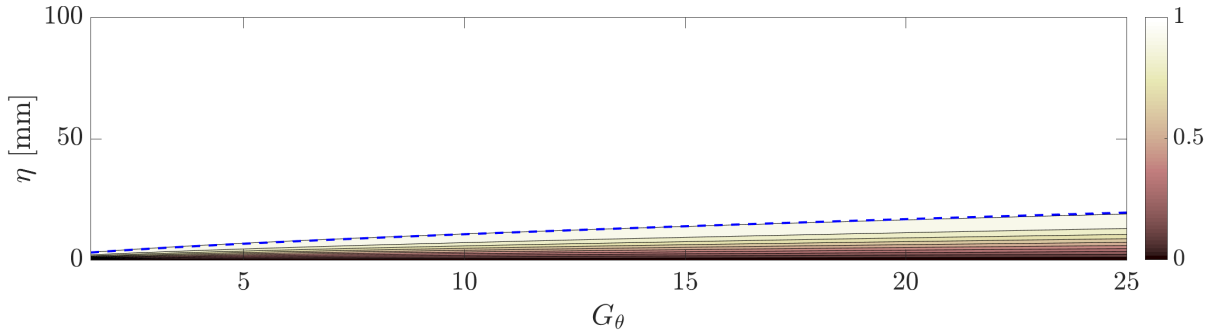

Figure 2.11: Velocity contours of U_b/U_∞ showing its evolution as G_θ progresses for the base-line case without perturbation (result of grid B). To note is that the highest contour line has the value $U_b/U_\infty = 0.99$, which represents the boundary layer thickness, δ. (- - -) Theoretical Blasius boundary layer thickness, $\delta_{Blasius}$.

2.5.3.1 Simulating the base flow

Before simulating the transitional flow, we would like to check whether the solver is capable of computing correctly the base flow without any perturbation, i.e. the laminar case. This simple test case allows to verify very basic but important parameters such as the correctness of the imposed boundary conditions, the utilized domain dimensions and the grid refinement. In the case of computing an incorrect base flow with the proposed set-up parameters, the generated results would not be physically significant.

First, we recall Eq. (1.22): $\mathbf{U} = \mathbf{U_b} + \mathbf{u}$; where the velocity flow field, $\mathbf{U}$, is decomposed into a velocity basic flow, $\mathbf{U_b}$, and a perturbation velocity field, $\mathbf{u}$. This test case aims thus at computing $\mathbf{U_b}$. Figure 2.11 shows the computed spanwise-averaged U_b for the grid B (with $N = 7$); results for grid A and C are not shown since no differences were found. This plot shows the streamwise evolution of the boundary layer as G_θ progresses. As seen, the computed boundary layer thickness, δ, follows very well the Blasius solution, $\delta_{Blasius}$.

Next, the displacement and momentum thicknesses obtained with the three constructed meshes (see Table 2.1) are shown in Figure 2.12a. As it can be seen, the three meshes are capable of producing the same results regardless of the polynomial order N. Besides, the computed results collapse with the Blasius theoretical solution. The same conclusions can be drawn for the computed wall-shear stresses which are plotted in Figure 2.12b. The computed velocity profile was also compared with the Blasius solution in Figure 2.12c and it was shown that the three meshes are capable of computing the self-similar Blasius profile all along the domain. In this chart, the profile at $G_\theta = 20$ ($Re_\xi = 4.07 \times 10^5$) was plotted.

Finally, as mentioned before, a particularity of the flow over a concave surface is that the curved motion tends to generate a negative pressure gradient in the wall-normal direction. In Figure 2.12d, the non-dimensional pressure profile at the inlet was plotted and compared with the DNS reference data of Schrader et al. (2011) showing that the same pressure distri-

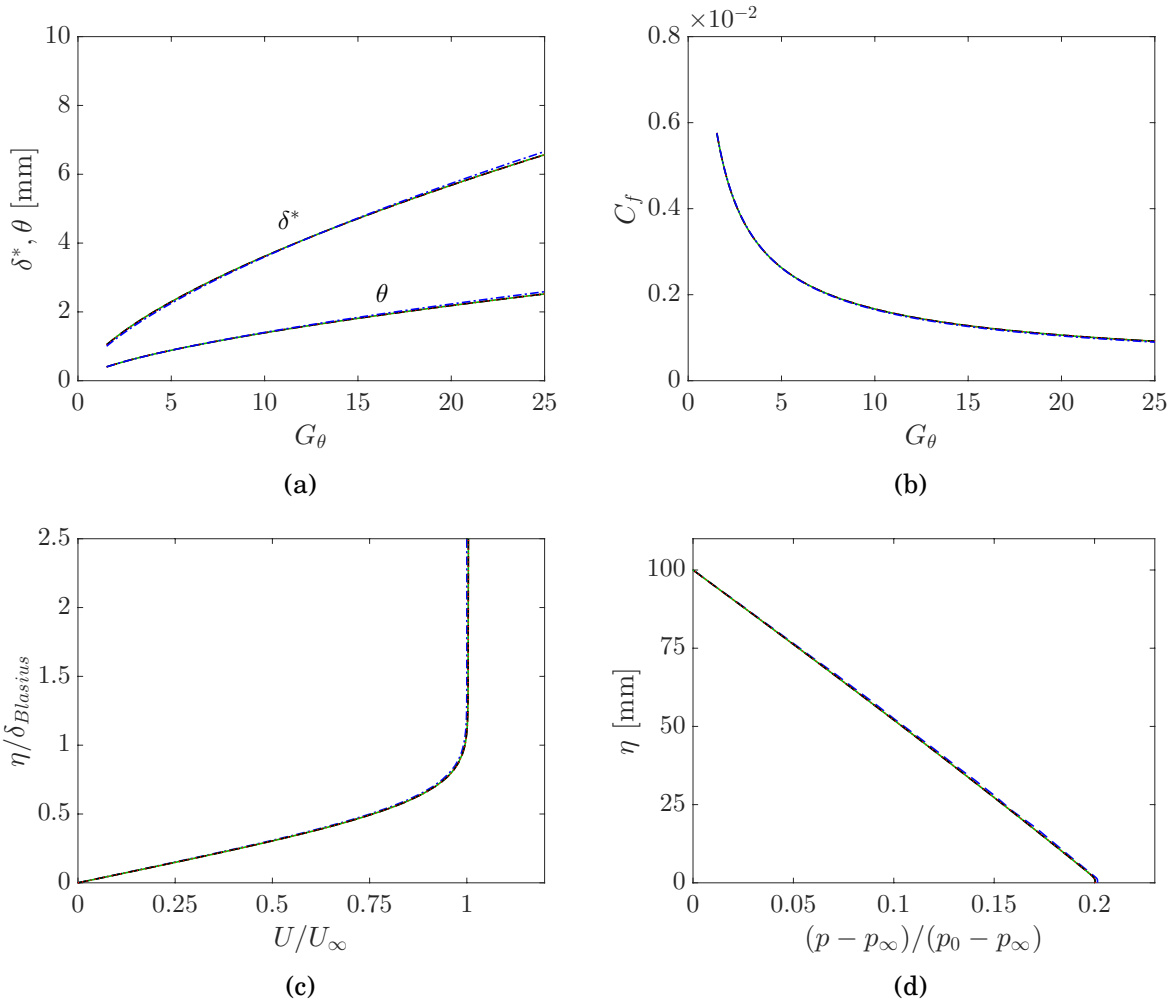

Figure 2.12: Comparison of the computed base flow using the three different grids. (a) Displacement and momentum thicknesses (δ^*,θ). (b) Skin-friction coefficient. (c) Boundary layer profile U/U_∞ at $G_\theta = 20$ ($Re_\xi = 4.07 \times 10^5$). (d) Wall-normal pressure profile all along the inlet at $G_\theta = 1.5$ ($Re_\xi = 1.33 \times 10^4$). Figures (a), (b) and (c) are compared with the Blasius theoretical solution; whereas, Figure (d) is compared with the DNS reference data (Schrader et al. 2011). (——) Grid A ($N = 5$), (- - -) grid B ($N = 7$), (·····) grid C ($N = 9$), (-·-·-) Blasius solution, and (- - -) Schrader et al. (2011).

bution is obtained. Here, p is the local static pressure, p_∞ is the free-stream static pressure and p_0 is the free-stream stagnation pressure.

In conclusion, all these results verify the correct computation of the laminar flow over a concave surface. In fact, it has been demonstrated theoretically (Floryan & Saric 1982) that the base flow is not affected by the curvature as $Re_\xi \to \infty$ and, therefore, it should follow the Blasius theoretical solution.

2.5.3.2 Response to wall-roughness perturbation

Once that the basic flow field has been correctly computed, the correct computation of the boundary layer response to localized wall-roughness is verified. For that, four bump-dimple wall-roughness elements with $h = 0.01\delta^*$ are used to perturb the boundary layer and the computed solution is compared with the DNS reference data of Schrader et al. (2011). This second test case will allow to determine whether a correct transitional Görtler flow over a concave surface can be computed with the set-up parameters and proposed grid refinement.

For this test case, the correct computation of the disturbance velocity field, $\mathbf{u}$, is checked ($\mathbf{u} = \mathbf{U} - \mathbf{U_b}$). The computed field of u/U_∞, using grid B ($N = 7$), is illustrated in Figure 2.13. Two different streamwise positions are shown; they correspond to a region where the primary instability is in its linear growth phase ($G_\theta = 4$, in Figure 2.13a) and to a region where the primary instability has saturated ($G_\theta = 12$, in Figure 2.13b), as it will be explained subsequently. As seen, the disturbance flow field is wavy and periodic in the spanwise direction, which makes it is amenable to be deconstructed in Fourier modes. This test will be then focused in computing the amplitude growth of each component of $\mathbf{u}$ and in computing the growth of the harmonics that compose the disturbance streamwise velocity, u.

For that, the disturbance velocity rms (root-mean-square) in the spanwise direction is computed in order to observe the evolution of their wall-normal maximum value (u_{rms}^{max}, v_{rms}^{max}, w_{rms}^{max}) at each streamwise position. This evolution can be seen as the growth of the spatial disturbances caused by the primary instability. For the streamwise disturbance component, u, we have for each streamwise location:

$$u_{rms}^{max} = \max(u_{rms}(\eta)) = \max\left(\sqrt{\frac{1}{Z}\int_0^Z [u(\eta,z)]^2 dz}\right). \tag{2.44}$$

The two other components, v_{rms}^{max} and w_{rms}^{max}, are computed similarly. The streamwise evolution of the three components is plotted in Figure 2.14a. As seen, the behavior of the perturbation velocity components does not change by increasing the polynomial order and the results match the ones obtained numerically by Schrader et al. (2011), who also used a grid with $N = 7$. Moreover, the primary instability growth rate is the same and its saturation occurs at the same streamwise position. The perturbation mostly affects the streamwise velocity component and a clear modification of the original laminar state of the flow can be noticed, which can be explained due to the inception of the Görtler vortices.

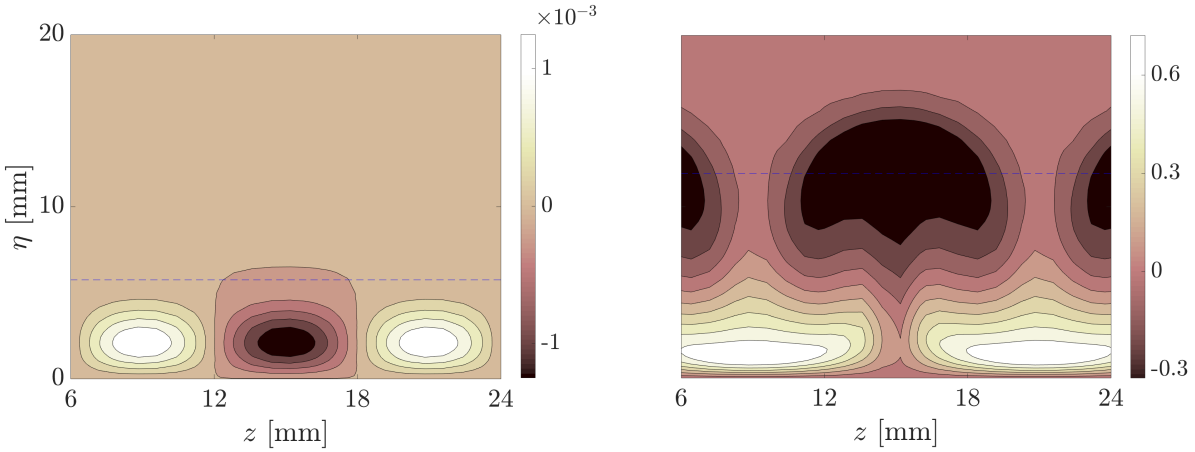

(a) (b)

Figure 2.13: Contour plots of the disturbance streamwise velocity, u/U_∞, computed with grid B ($N = 7$). (a) $G_\theta = 4$. (b) $G_\theta = 12$. (- - -) $\delta_{Blasius}$

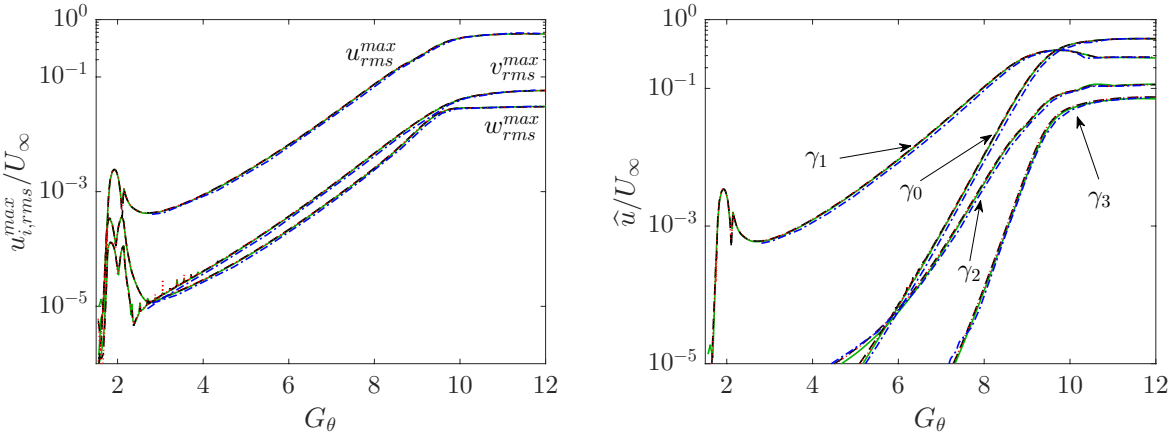

(a) (b)

Figure 2.14: Comparison of the boundary layer response to localized wall-roughness with reference DNS data (Schrader et al. 2011). (a) Streamwise evolution of $\mathbf{u}^{\mathbf{max}}_{\mathbf{rms}}$ for different polynomial orders. (b) Streamwise evolution of the first four Fourier modes of the streamwise disturbance velocity, u. Spanwise spatial frequencies of the plotted modes: $\gamma_0 = 0$, $\gamma_1 = 1/\lambda$, $\gamma_2 = 2/\lambda$ and $\gamma_3 = 3/\lambda$. $N = 5$ (——), $N = 7$ (- - -), $N = 9$ (·····) and Schrader et al. (2011) (-·-·-).

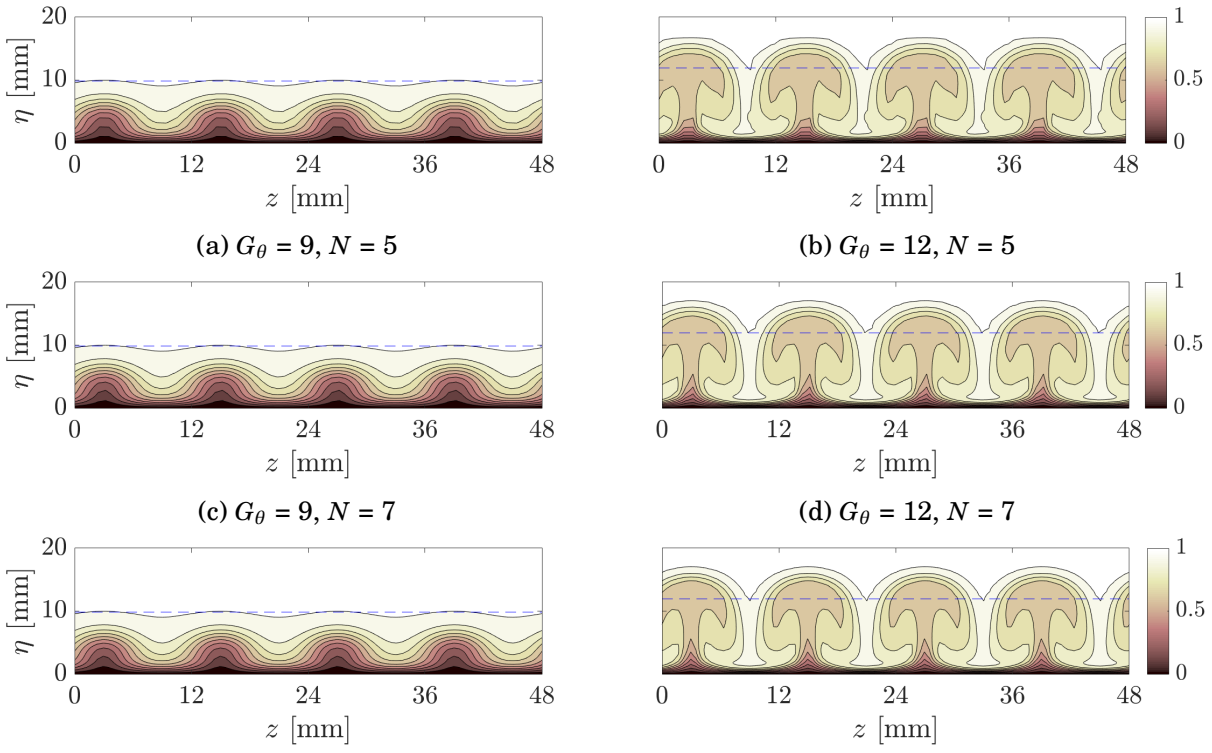

(a) $G_\theta = 9$, $N = 5$ (b) $G_\theta = 12$, $N = 5$

(c) $G_\theta = 9$, $N = 7$ (d) $G_\theta = 12$, $N = 7$

(e) $G_\theta = 9$, $N = 9$ (f) $G_\theta = 12$, $N = 9$

Figure 2.15: Velocity contours of U/U_∞ at $G_\theta = 9$ and 12 for $N = 5$, 7 and 9. (- - -) $\delta_{Blasius}$.

Next, the disturbance flow field is decomposed in several Fourier modes, where the higher harmonics start to appear as the flow becomes nonlinear. The growth, as well as the saturation, of the first four modes (with spanwise spatial frequencies $\gamma_0 = 0$, $\gamma_1 = 1/\lambda$, $\gamma_2 = 2/\lambda$ and $\gamma_3 = 3/\lambda$) of the streamwise disturbance velocity, u, is plotted in Figure 2.14b. To note is that only the wall-normal maximum value at each streamwise position is plotted. In the chart, $\widehat{u}$ indicates the modes amplitude. Once again, it is shown that the results obtained with the three polynomial orders match the reference DNS data of Schrader et al. (2011). In conclusion, these two results are able to verify the correct computation of the transitional flow over a concave surface, with Görtler vortices developing, with the three proposed meshes.

Next, the streamwise velocity contours computed with different polynomial orders are shown in Figure 2.15. At $G_\theta = 9$, the flow starts to have a wavy shape in the spanwise direction with a lower boundary layer thickness at the downwash regions and a higher one at the upwash regions. Downstream, at $G_\theta = 12$, a mushroom-like structure, which is inherent to the Görtler flow, appears in the upwash regions to exceed the theoretical Blasius boundary layer thickness. The mushroom-like structure evolution is almost the same regardless of the polynomial order employed.

Even though the three polynomial orders seem to correctly compute the transitional flow,

a mesh with $N = 7$ (grid B) was chosen to be used for the current research study. This choice is conform with the previous Görtler vortices SEM numerical investigations of Schrader et al. (2011), who used $N = 7$, and of Ducoin et al. (2017), who showed that $N = 7$ is sufficient to get a full DNS resolution and that the increase of this polynomial order does not affect the simulation results.

Chapter 3
Boundary layer transition caused by centrifugal instabilities

3.1 Introduction

The results presented in this chapter were published in the scientific journal *Computers and Fluids* (Méndez et al. 2018). The article cover is presented in the following page.

In this chapter, the laminar-to-turbulent transition process over a concave surface is studied using direct numerical simulations (DNS). It is found that the flow passing over such surface is highly susceptible to develop centrifugal instabilities in the form of Görtler vortices. Transition is triggered by means of wall-roughness elements which also serve to preset the wavelength of the Görtler vortices that remains constant during their streamwise development. This allows to obtain a clear spanwise characterization of the Görtler boundary layer, and its breakdown into turbulence. The different regions encountered in the transition process, *i.e.*, linear, nonlinear, transition and fully turbulent, are identified and characterized. Parametric studies are presented showing that the transition starting point is delayed when the radius of curvature is increased, however, it occurs at the same critical Görtler number. Additionally, an increase of the height of the wall-roughness elements advances the transition onset upstream. Moreover, a linear relation between the critical Görtler number and the Reynolds number based on the wall-roughness streamwise location has been found. Furthermore, it is observed that, compared to a wall-roughness bump element, a bump-dimple geometry is more efficient for exciting the transition process.

The results were obtained with the simulation set-up (i.e. computational domain, boundary conditions, grid refinement and perturbation method) that was described in detail in Section 2.5.2.

Computers and Fluids 171 (2018) 135–153

Contents lists available at ScienceDirect

Computers and Fluids

journal homepage: www.elsevier.com/locate/compfluid

Boundary layer transition over a concave surface caused by centrifugal instabilities

M. Méndez [a], M.S. Shadloo [a,*], A. Hadjadj [a], A. Ducoin [b]

[a] CORIA-UMR 6614 - Normandie Université CNRS-Université et INSA Rouen-Normandie, Rouen 76000, France
[b] LHEEA Laboratory, Ecole Centrale de Nantes (CNRS UMR 6598), Nantes 44300, France

ARTICLE INFO

Article history:
Received 28 March 2018
Revised 25 May 2018
Accepted 14 June 2018
Available online 15 June 2018

Keywords:
Boundary layer transition
Centrifugal instabilities
Görtler vortices
Direct numerical simulation (DNS)

ABSTRACT

The laminar-to-turbulent transition process over a concave surface is studied using direct numerical simulations (DNS). It is found that the flow passing over such surface is highly susceptible to develop centrifugal instabilities in the form of Görtler vortices. Transition is triggered by means of wall-roughness elements which also serve to preset the wavelength of the Görtler vortices that remains constant during their streamwise development. This allows to obtain a clear spanwise characterization of the Görtler boundary layer, and its breakdown into turbulence. The different regions encountered in the transition process, i.e., linear, nonlinear, transition and fully turbulent, are identified and characterized. Parametric studies are presented showing that the transition starting point is delayed when the radius of curvature is increased, however, it occurs at the same critical Görtler number. Additionally, an increase of the height of the wall-roughness elements advances the transition onset upstream. Moreover, a linear relation between the critical Görtler number and the Reynolds number based on the wall-roughness streamwise location has been found. Furthermore, it is observed that, compared to a wall-roughness bump element, a bump-dimple geometry is more efficient for exciting the transition process.

1. Introduction

The development of a boundary layer passing over a concave surface is very different from that of a flat plate. The curved motion of the flow creates a centrifugal force acting in the wall-normal direction that is balanced by a negative pressure gradient generated in the same direction. The resulting force field makes the boundary layer susceptible to develop centrifugal instabilities that can be easily triggered by a radial displacement of the fluid particles caused by different types of perturbations [1], e.g. wall-roughness or free-stream turbulent intensity.

These centrifugal instabilities, that initiate the transition process, have the form of steady streamwise-oriented counter-rotating vortex pairs and are known as Görtler vortices [2]. Their study and characterization is relevant because it can help to improve the performance of many engineering components such as wind turbines [3], turbomachinery blades [4], nozzles [5] and airfoils [6].

It was Görtler [2], in 1941, who proposed a non-dimensional parameter that determines the appearance of the longitudinal vortices in a boundary layer over a concave surface. This parameter, known as the Görtler number G_θ, is defined as:

$$G_\theta = \frac{U_\infty \theta}{\nu}\sqrt{\frac{\theta}{R}}, \tag{1}$$

where U_∞ is the free-stream velocity, θ is the boundary layer momentum thickness based on the laminar Blasius solution, ν is the kinematic viscosity and R is the surface radius of curvature. The Görtler number represents a ratio of the destabilizing inertial and centrifugal forces to the stabilizing viscous forces.

Most of the first theoretical studies of the Görtler vortices were focused in finding the existence of a unique critical Görtler number that would determine their onset. Those analyses were performed using linear stability theory and an extensive review of them can be found in the works of Floryan [7], Saric [8] and Hall [9]. However, Hall [10] determined that the most appropriate method for the Görtler instability analysis is the numerical integration of the governing hydrodynamics equations. The author showed that the position of the neutral stability curve depends on the boundary layer receptivity, i.e., location and character of the initial disturbances; so that the concept of a unique critical number, so familiar in the hydrodynamic-stability theory, is not suitable in the Görtler flow, except for the asymptotically small wavelengths.

Several experimental studies have been performed in order to visualize and characterize the development of the Görtler bound-

* Corresponding author.
E-mail address: msshadloo@coria.fr (M.S. Shadloo).

https://doi.org/10.1016/j.compfluid.2018.06.009
0045-7930/

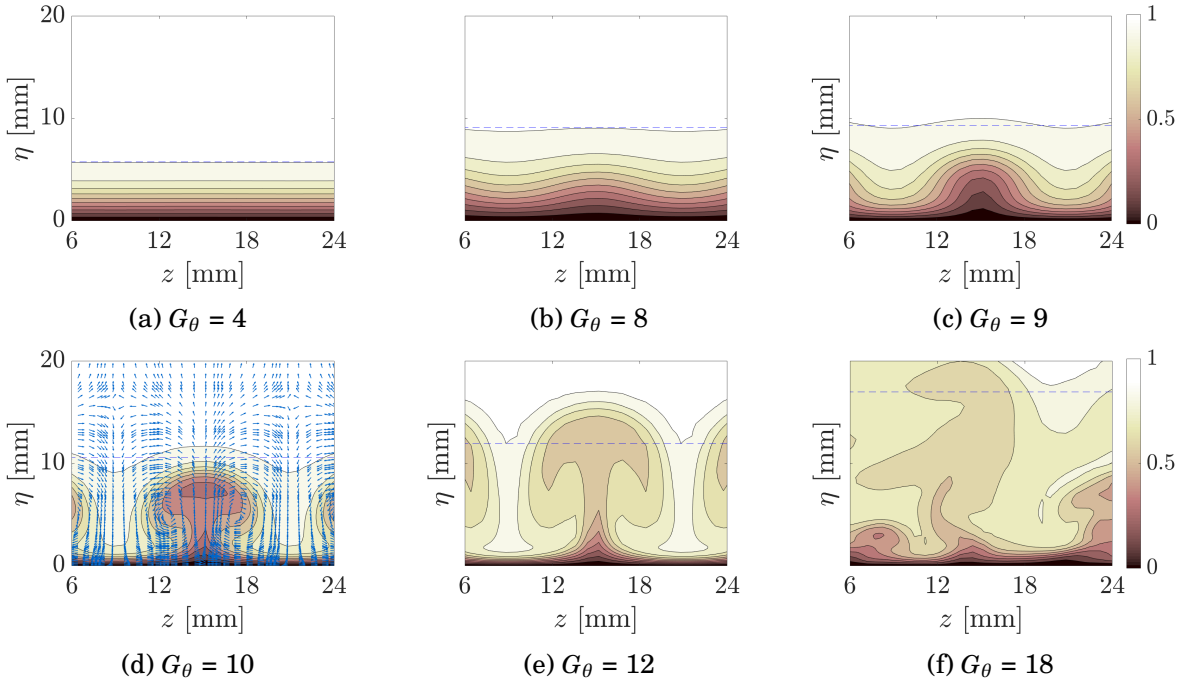

(a) $G_\theta = 4$ (b) $G_\theta = 8$ (c) $G_\theta = 9$

(d) $G_\theta = 10$ (e) $G_\theta = 12$ (f) $G_\theta = 18$

Figure 3.1: Streamwise evolution of U/U_∞. On subfigure (d), the velocity vectors are plotted to appreciate the rotating movement of the Görtler vortices. The Blasius boundary layer thickness, $\delta_{Blasius}$, is plotted for comparison (- - -).

3.2 Boundary layer transition

3.2.1 Base flow modification due to Görtler vortices

The boundary layer transition starts with the inception of the Görtler vortices which modify the original laminar base flow. During their development, the associated rotational movement generates a wavy velocity profile in the spanwise direction, where two regions can be clearly distinguished: upwash and downwash. In the upwash region, the boundary layer is elongated due to the upward movement of the vortices, whereas a compression of the boundary layer, due to the downward movement of the vortices, occurs in the downwash region. In Figure 3.1, the evolution of the instantaneous streamwise velocity component, U, highlights the explained phenomenon. At $G_\theta = 4$, the flow is in the linear region where it follows the laminar Blasius solution and the effect of the Görtler vortices is not noticeable yet. Downstream, the swirl motion of the vortices starts to affect the flow and a wavy shape can start to be appreciated ($G_\theta = 8$). This wavy pattern tends to become more pronounced ($G_\theta = 9$) until a mushroom-like structure, formed of low-momentum flow, emerges from the upwash region ($G_\theta = 10$). This mushroom-like structure is typical in the development of the Görtler vortices and is caused by the strong non-linearities created in the $\eta - z$ plane (Lee & Liu 1992). At $G_\theta = 10$, the velocity vectors are plotted in order to observe the rotational motion

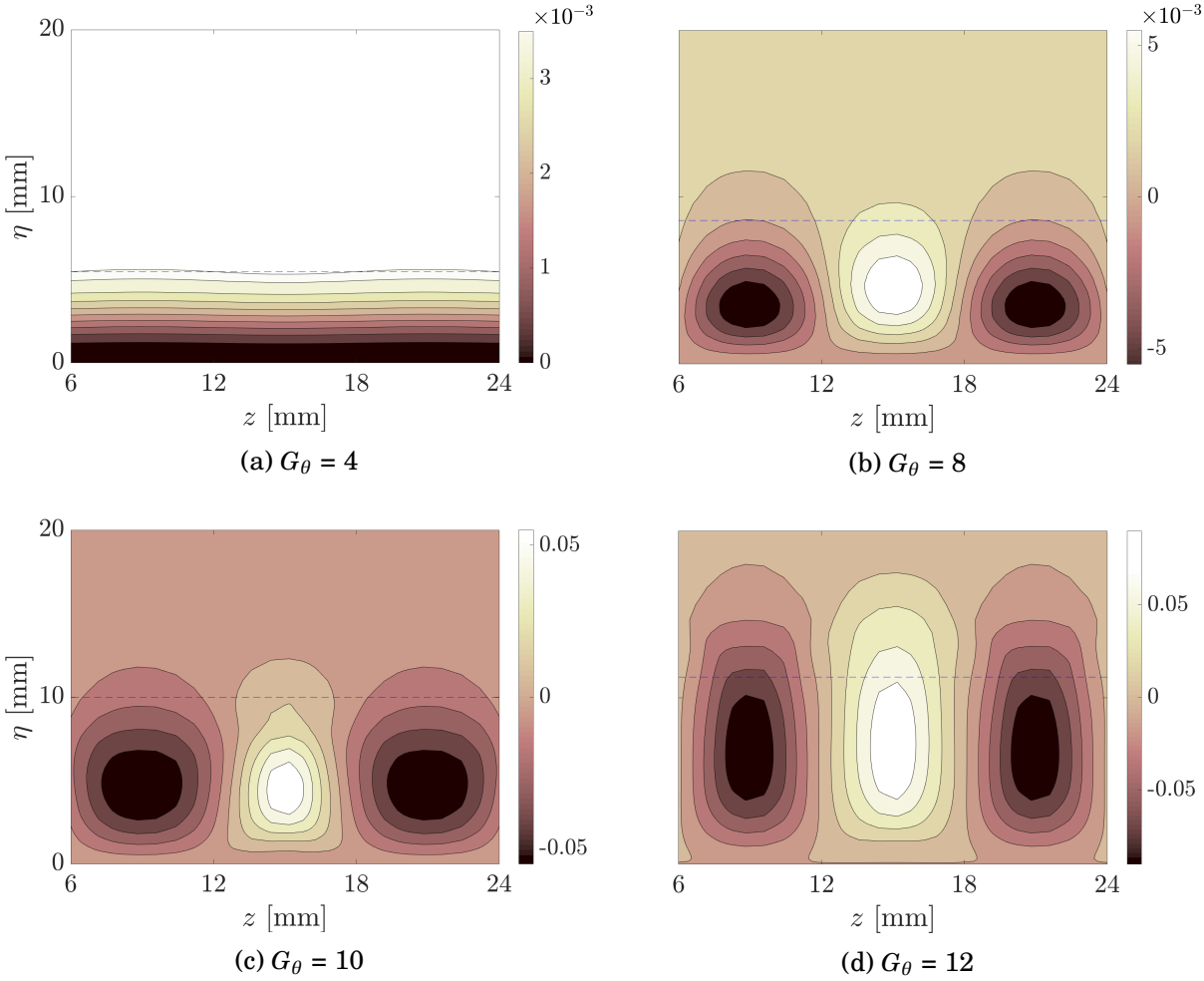

(a) G_θ = 4 (b) G_θ = 8

(c) G_θ = 10 (d) G_θ = 12

Figure 3.2: Streamwise evolution of V/U_∞. (- - -) $\delta_{Blasius}$.

of the Görtler vortices and identify the upwash and downwash regions. As the flow evolves, the mushroom-like structure continues its growth and elongation, clearly surpassing the thickness of the Blasius boundary layer (G_θ = 12). Farther downstream, the flow enters into the transition region and the mushroom-like structure is destroyed due to the inception of the secondary instabilities and the turbulence development ($G_\theta = 18$).

In order to extend the characterization of the streamwise evolution of the Görtler vortices, the two cross velocity components, V and W, the vorticity component in the streamwise direction, ω_ξ, and the pressure coefficient, C_p are plotted in Figures 3.2, 3.3, 3.4 and 3.5, respectively. These quantities are plotted in the linear ($G_\theta = 4,8$) and nonlinear ($G_\theta = 10,12$) regions of the transition process.

Regarding the wall-normal velocity component (Figure 3.2), it is observed that, at $G_\theta = 4$, it still follows the distribution of the Blasius profile. However, downstream, the Görtler

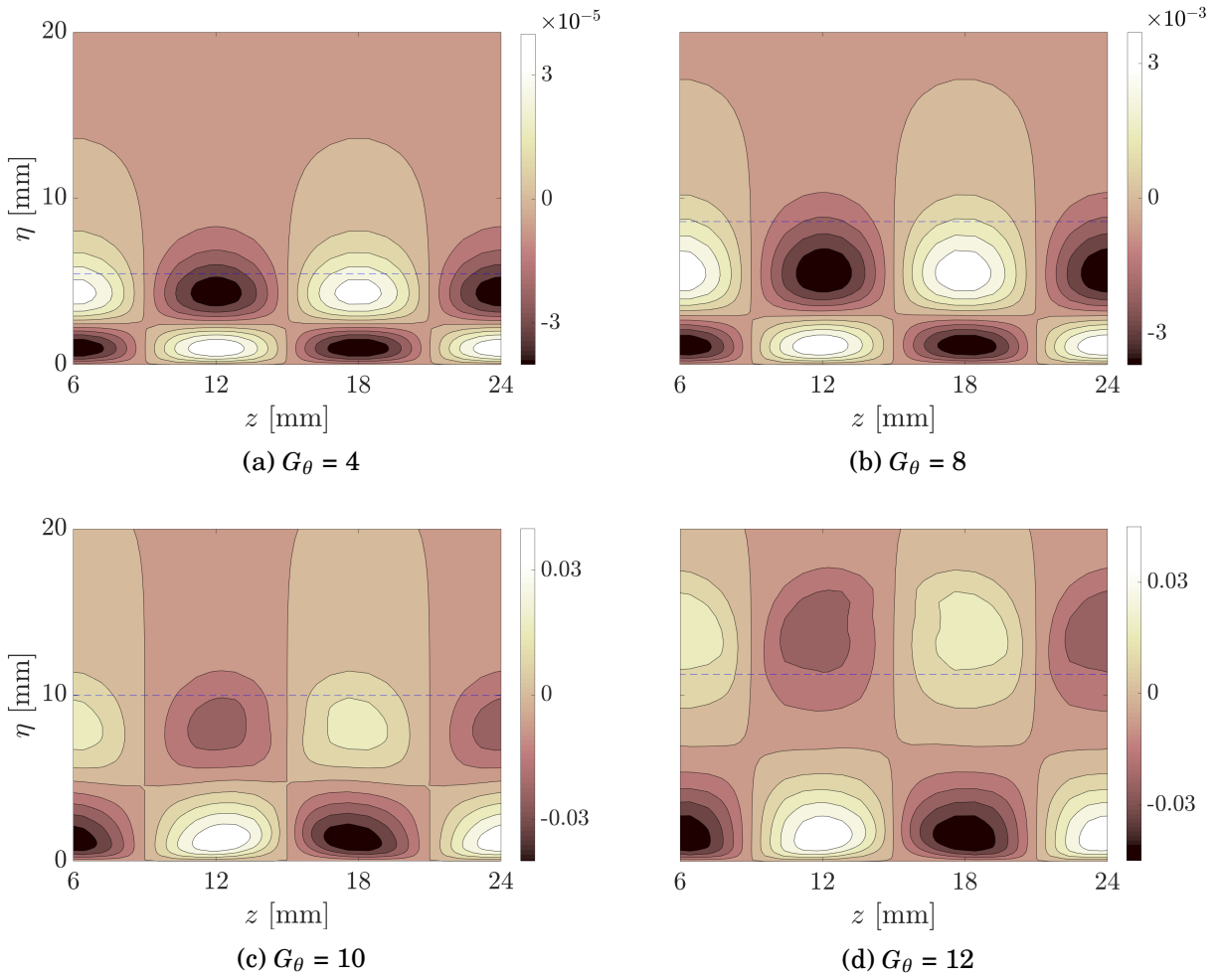

(a) G_θ = 4 (b) G_θ = 8

(c) G_θ = 10 (d) G_θ = 12

Figure 3.3: Streamwise evolution of W/U_∞. (- - -) $\delta_{Blasius}$.

vortices clearly modify this velocity profile and a symmetric distribution, with respect to the upwash location, can be appreciated. This distribution has a local maximum at the upwash location and a local minimum at the downwash location. As the flow continues to evolve, the same distribution is kept but the velocity increases in magnitude; which occurs in accordance with the evolution of v_{rms}^{max} in Figure 2.14a.

With respect to the spanwise velocity component (Figure 3.3), an anti-symmetric distribution with respect to the upwash location is observed. Four points of local maximum and minimum values can be appreciated, with higher values corresponding to the anti-symmetric pair closer to the wall, which indicates a higher rotational speed of the vortices in their lower region (between their center and the wall). The same velocity distribution is maintained as the flow evolves; however, the magnitude of the velocity component increases. It is worth noticing that most of the previous experimental and numerical studies have been

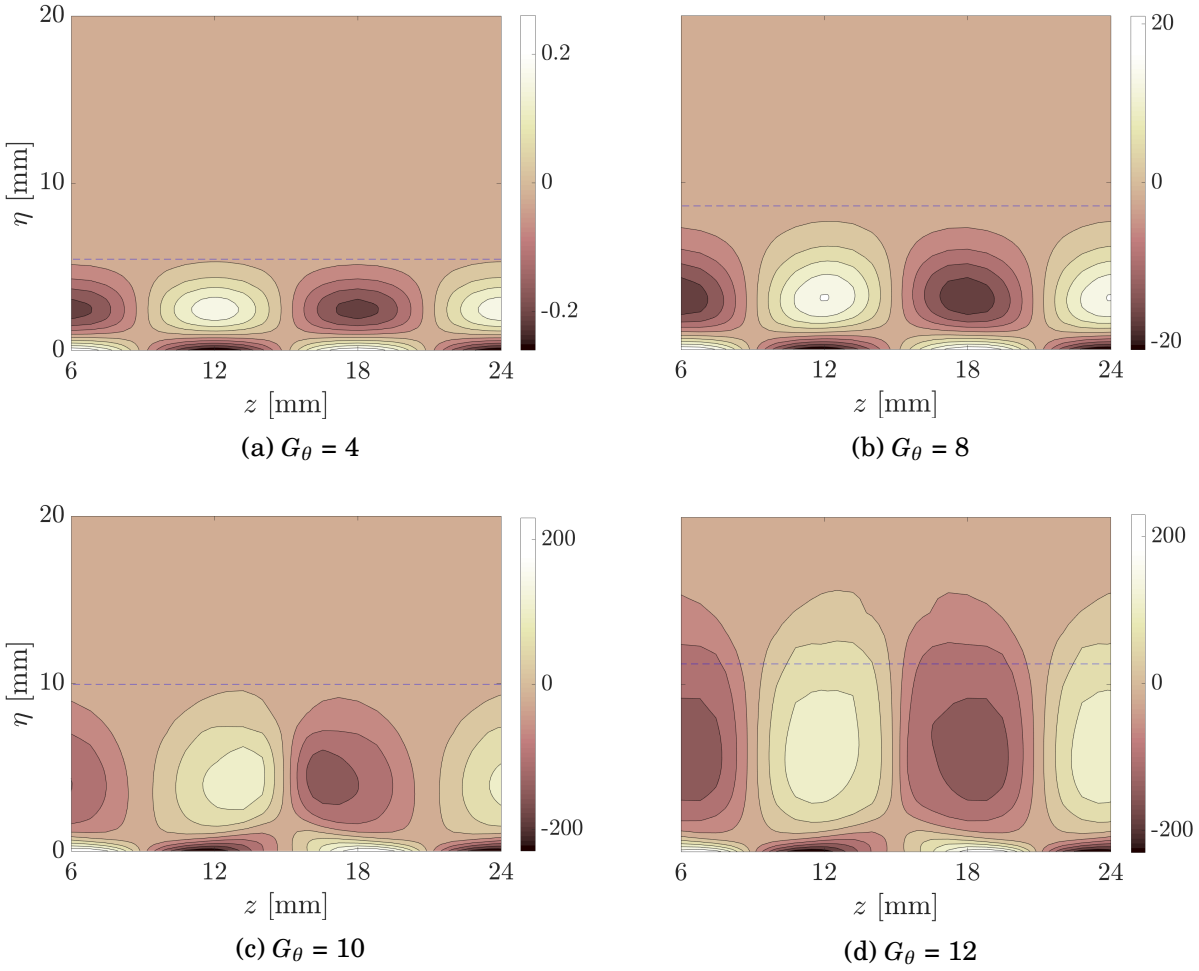

(a) G_θ = 4 (b) G_θ = 8

(c) G_θ = 10 (d) G_θ = 12

Figure 3.4: Streamwise evolution of ω_ξ (units in s^{-1}). (- - -) $\delta_{Blasius}$.

focused in characterizing only the streamwise velocity component of the Görtler vortices. Tandiono et al. (2013), for instance, measured experimentally the spanwise velocity component for the first time. However, a clear characterization could not be obtained because of the difficulties in perfectly aligning the center-line of the wind tunnel with the one of the concave surface test section. As a result, their vortex structures are slightly skewed to the left and the velocity field of W is dominated by regions of negative values.

Regarding the vorticity component in the streamwise direction (Figure 3.4), ω_ξ, it is also distributed anti-symmetrically with respect to the upwash location. An anti-symmetric pair, of local maximum and minimum values, is located near the wall due to the high shears in the wall-normal direction. Besides, a second anti-symmetric pair is located at the center of the Görtler vortices. In accordance with the increase in magnitude of the cross velocity components, V and W, the streamwise vorticity component magnitude also increases as the

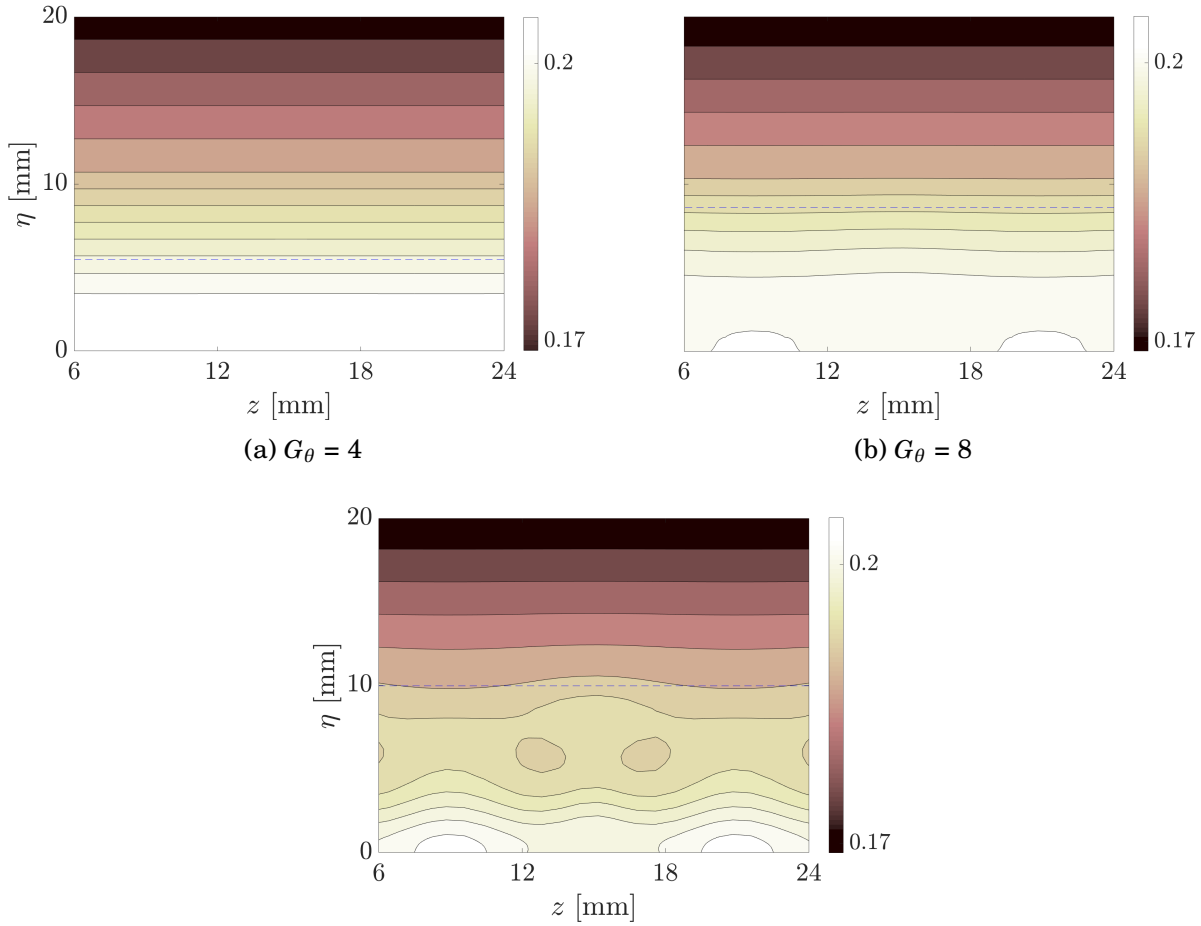

(a) $G_\theta = 4$ (b) $G_\theta = 8$

(c) $G_\theta = 10$

Figure 3.5: Streamwise evolution of C_p. (- - -) $\delta_{Blasius}$.

flow evolves downstream.

The evolution of the pressure coefficient is plotted in Figure 3.5. It is defined as $C_p = (p - p_\infty)/(p_0 - p_\infty)$, where p is the local static pressure, p_∞ is the free-stream static pressure and p_0 is free-stream stagnation pressure. From the contour plots, a clear negative gradient in the radial direction can be observed. This similar radial distribution of C_p is kept during the streamwise development of the flow. However, at $G_\theta = 8$ and 10, two local maxima are noticed in the wall at the downwash regions. These regions of higher pressure occur at the location where the flow impacts the wall guided by the swirl motion of the vortices. Moreover, at $G_\theta = 10$, two local minima, located at $\eta = 5$ mm, can be appreciated. These local minima correspond to the center location of the Görtler vortices.

As it has been shown in this section, the initial Blasius profile is clearly modified once the Görtler vortices appear in the flow. From Figure 3.1, it is seen that on the head of

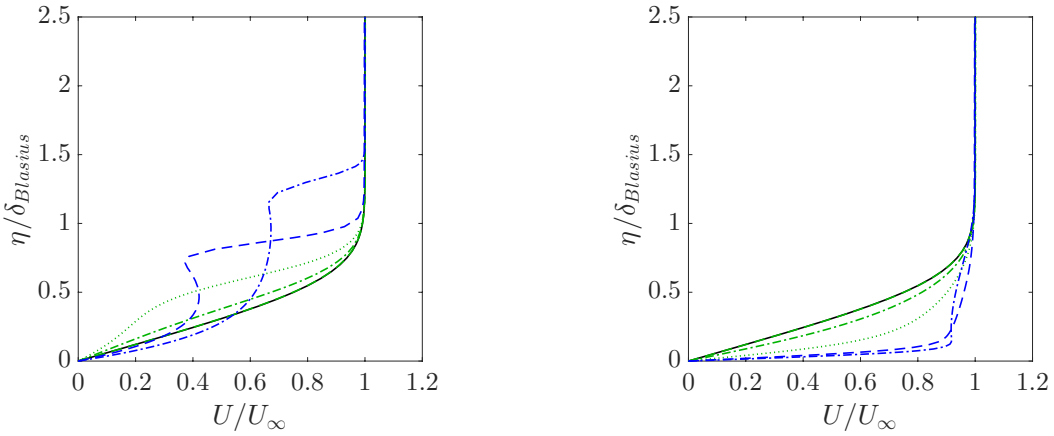

(a) Upwash (b) Downwash

Figure 3.6: Streamwise evolution of the velocity profile U/U_∞ at the upwash and downwash regions. (——) Blasius solution, (- - -) $G_\theta = 4$, (–·–) $G_\theta = 8$, (·····) $G_\theta = 9$, (- - -) $G_\theta = 10$ and (-·-·-) $G_\theta = 12$.

the mushroom-like structure, there is low velocity flow riding over high velocity flow. This behavior causes the appearance of inflection points, which are known to be the main source of instability, in the wall-normal velocity profile. On the other hand, the boundary layer in the downwash region becomes more stable because it is shortened. The streamwise evolution of $U(\eta)$, at upwash and downwash locations, is plotted in Figure 3.6 in order to observe how these instabilities arise. Initially, at $G_\theta = 4$, the velocity profiles, at upwash and downwash regions, fit with the Blasius velocity profile. However, in the upwash location, as the flow develops, the velocity profile departs from the initial solution and tends to get thinner and more elongated ($G_\theta = 8,9$). Further downstream, the upwash velocity profile gets a highly inflectional S-shape form containing inflection points ($G_\theta = 10,12$). From Figure 2.14, it is seen that the S-shape profile arises once the primary instability has saturated. More specifically, this flow feature occurs in the nonlinear region of the transition process. This type of velocity profile is known to be highly unstable and susceptible to develop secondary instabilities (Saric 1994). Regarding the downwash region, it is observed that the boundary layer thickness is shortened which results in a lower deficit velocity profile less susceptible to develop instabilities.

3.2.2 Development of secondary instabilities

It is noted that the temporal velocity fluctuations start to become noticeable in the flow field once the secondary instabilities start to develop, as it will be shown. Thus, recalling Equation (1.11), the instantaneous velocity field, $\mathbf{U} = \overline{\mathbf{U}} + \mathbf{u}'$, is decomposed in a mean (time-averaged) component, indicated by the overline, $\overline{\mathbf{U}}$, and its respective temporal fluctuation, indicated by the prime symbol, $\mathbf{u}'$.

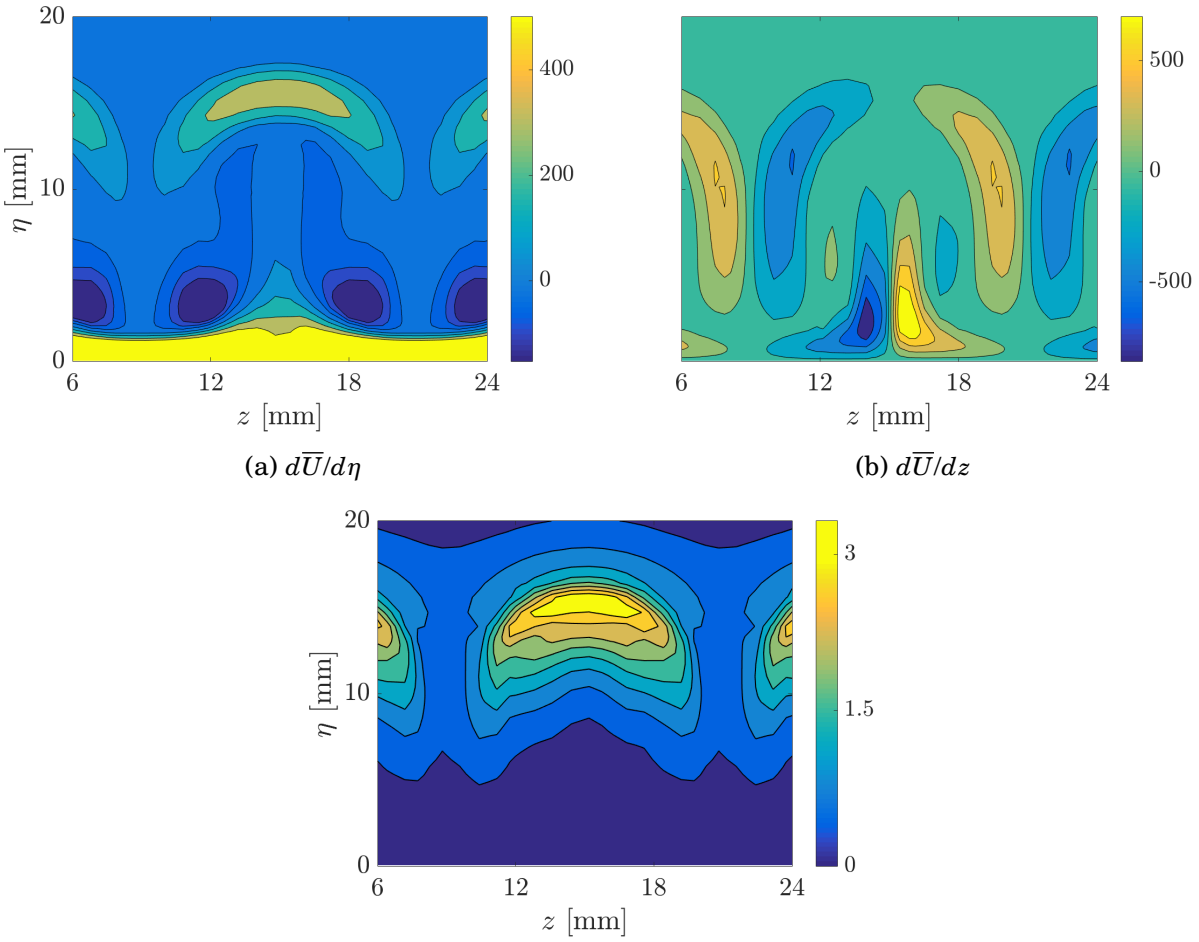

(a) $d\overline{U}/d\eta$ (b) $d\overline{U}/dz$

(c) Tu

Figure 3.7: Iso-shear contours of $d\overline{U}/d\eta$, $d\overline{U}/dz$ (both in s^{-1}) and Tu (in %) at $G_\theta = 12$.

As it has been reported before (Swearingen & Blackwelder 1987), the development of secondary instabilities can be associated to the inflectional velocity profile in the spanwise direction, i.e. $U(z)$, rather than in the wall-normal direction, $U(\eta)$. In fact, the secondary instability of sinuous type is associated with high shears in the spanwise direction, dU/dz, and the varicose type is linked to the high shears in the wall-normal direction, $dU/d\eta$ (Saric 1994, Yu & Liu 1991).

In Figure 3.7, the iso-contours of both $d\overline{U}/d\eta$ and $d\overline{U}/dz$ are plotted at $G_\theta = 12$, which is a location where the primary instability has already evolved and secondary instabilities start to appear. Regarding $d\overline{U}/d\eta$, it is observed that its highest values occur in the near-wall region; a positive maximum can also be observed in the upwash region where the head of the mushroom-like structure is located and corresponds to the upper inflection point of the S-shape profile. Two local negative minimum, located closer to the wall, are also observed

and they correspond to the lower inflection point of the S-shape profile. With respect to $d\overline{U}/dz$, high shear regions, product of the wavy velocity profile in the spanwise direction, can also be observed. The anti-symmetric pair of local maximum and minimum located near the wall corresponds to a region where the Görtler vortices turn towards the boundary layer edge; whereas the second anti-symmetric pair corresponds to the zone where the vortices turn towards the wall. In general, the $d\overline{U}/d\eta$ and $d\overline{U}/dz$ shear distribution obtained in this study matches the experimental distributions previously reported by Tandiono et al. (2008).

The turbulence intensity is defined as

$$Tu = \sqrt{\frac{2k/3}{\overline{U}^2 + \overline{V}^2 + \overline{W}^2}}, \tag{3.1}$$

where k is the turbulence kinetic energy and is defined as $k = (\overline{u'^2} + \overline{v'^2} + \overline{w'^2})/2$. Besides, $\overline{U}$, $\overline{V}$ and $\overline{W}$ are the mean velocity components. Meanwhile, $\overline{u'^2}$, $\overline{v'^2}$ and $\overline{w'^2}$ represent the mean of the instanteneous velocity fluctuations squared. In Figure 3.7c, the contours of Tu are plotted at G_θ = 12. As observed, the region with the highest values of Tu occurs on the head of the mushroom-like structure and it is quite correlated with the region of maximum shear $d\overline{U}/d\eta$. This suggests that the secondary instability is triggered by the inflection point close to the boundary layer edge in the wall-normal boundary layer profile. Thus, as mentioned before, a secondary instability produced by high shears $d\overline{U}/d\eta$ is associated with the varicose mode and with the emergence of horseshoe vortices.

In order to observe the type of secondary instabilities that develop from the Görtler vortices, the vortical coherent structures are shown using the λ_2 vortex criterion (Jeong & Hussain 1995) in Figure 3.8. Only the first half of the domain is depicted, from $\phi_{loc} = 0°$ to 90°, or equivalently, from G_θ = 1.5 to 16.4. Basically, iso-surfaces of $\lambda_2 = -125$ are plotted in order to highlight the development of the primary and the secondary instabilities. At first, the inception of the Görtler vortices is observed, which are identified with the four pairs of elongated streaks in the streamwise direction. As they develop, it is seen how they evolve into secondary instabilities of the varicose type which are identified with horseshoe vortices. In this simulation, only the varicose mode could be observed; the employed parameters (i.e., the chosen wavelength Λ) did not allow to excite the sinuous mode. In fact, Li & Malik (1995) showed that the even mode (varicose) is stronger for large wavelengths while the odd mode (sinuous) is stronger for short wavelengths. Basically, a shorter spanwise wavelength Λ would allow to produce greater spanwise shears which will help to excite the sinuous mode. In Section 3.3.3, a parametric study, where the spanwise wavelength is varied, is performed. It is shown that a smaller wavelength of $\Lambda = 162$ is able to excite the odd mode.

It has been shown that the Görtler vortices are primary instabilities and that they do not directly break down into turbulence, they rather set up an unstable flow field susceptible to develop secondary instabilities. Primary instabilities are steady and they can be associated with a wavy and periodic velocity profile in the spanwise direction. Hence, the disturbance

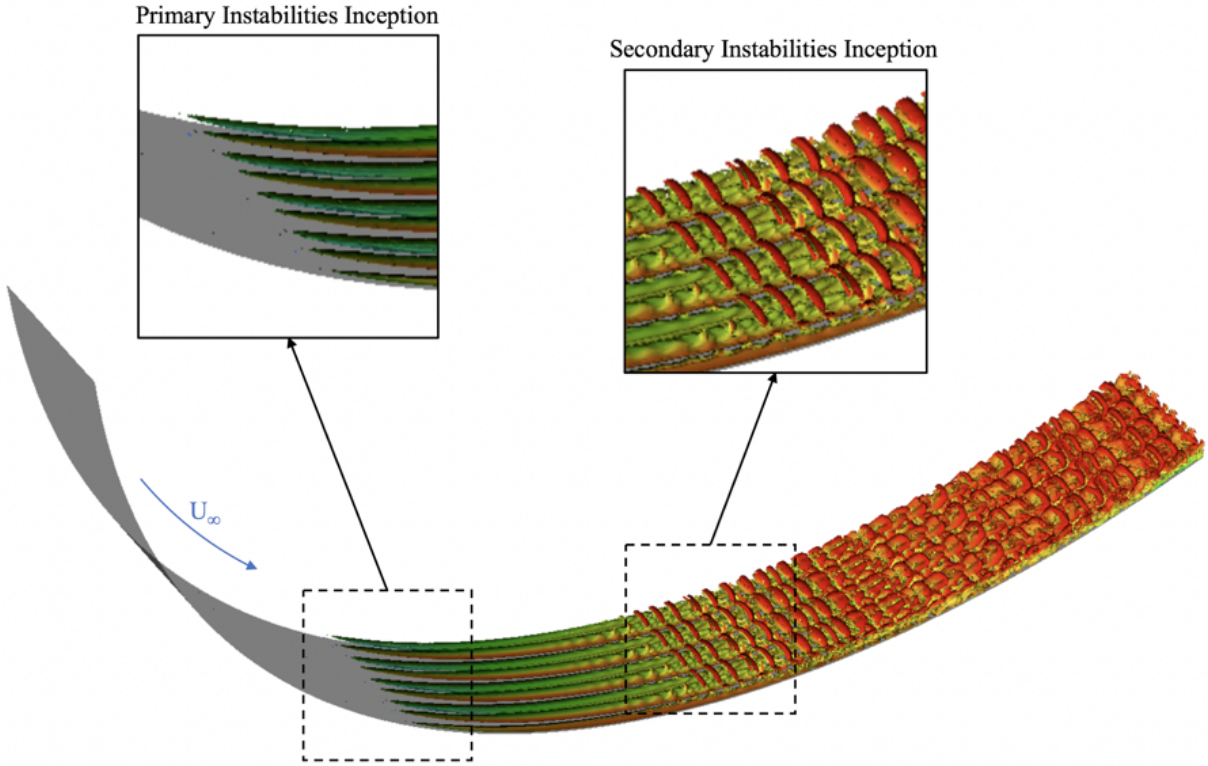

Figure 3.8: Vortical coherent structures obtained with iso-surfaces of $\lambda_2 = -125$. Sub-domain bounded from $\phi_{loc} = 0°$ to 90°.

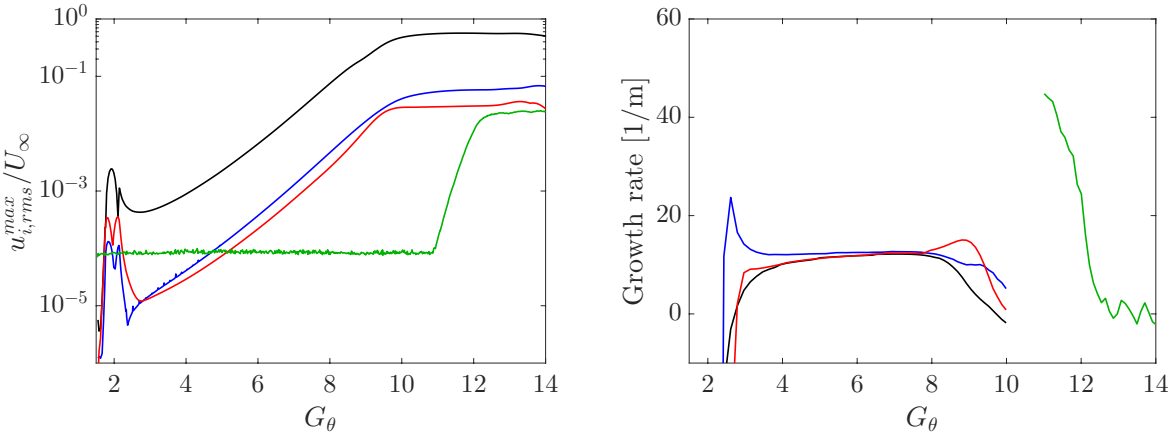

Figure 3.9: (a) Streamwise development of the maximum spatial velocity disturbances, u_{rms}, v_{rms} and w_{rms}, and of the maximum temporal velocity fluctuations, Tu. (—) u_{rms}^{max}, (—) v_{rms}^{max}, (—) w_{rms}^{max} and (—) Tu_{max}. (b) Growth rate, β, of each instability. (—) β_u, (—) β_v, (—) β_w and (—) β_{Tu}.

field is normally related to spatial fluctuations and in the stability analyses is assumed to have the form $\mathbf{u} = \mathbf{u}(\eta)e^{\beta\xi}\cos(\alpha z)$, where β is the streamwise growth rate and α is the spanwise wavenumber ($\alpha = 2\pi/\lambda$) (see Eq. 1.24). With respect to the secondary instabilities, they are unsteady and related to velocity fluctuations that lead to turbulence. Therefore, the turbulence intensity, Tu, can be used to measure the growth of the secondary instabilities as it has been done by Swearingen & Blackwelder (1987).

In Figure 3.9a, $\mathbf{u_{rms}^{max}}$ (see Eq. 2.44) is plotted to observe the growth and saturation of the spatial disturbances. The wall-normal maximum value of the turbulence intensity, Tu_{max}, is also plotted to show the growth and saturation of the temporal velocity fluctuations. The first peaks in the development of the spanwise spatial disturbances correspond to the location of the wall-roughness elements. Then, a growth of the three components can be observed. It corresponds to the linear region of the transition process and it is related to the growth of the primary instability, which, as it is seen, develops in a steady manner (since the levels of turbulence intensity are smaller than 0.01%). The linear development of the primary instability ends with the saturation of the spatial disturbances which occurs at $G_\theta = 9.6$, for the streamwise component and followed shortly after by the other components. After the saturation, the nonlinear region of the transition process is followed, which it is still steady but only at its beginning. During this steady part of the nonlinear region, the mushroom-like structures start to develop in the upwash location as seen in Figure 3.1. Later, the flow field starts to develop unsteady secondary instabilities which can be correlated with the exponential increase of the turbulence intensity that starts at the streamwise position of $G_\theta = 10.9$. From the slope of Tu, it can be seen that the secondary instabilities grow faster than the primary one.

The slope of the curves plotted in Figure 3.9a represents the streamwise growth rate, β, of the primary and secondary instabilities (a positive value indicates their amplification). The value of β at every streamwise position is shown in Figure 3.9b. The primary instability growth rate increases fast at first and then a region with a more moderated increment is reached with a maximum value of 12.2 m^{-1} for the streamwise position of G_θ = 7.1 (for the growth rate measured in the streamwise velocity component u). Regarding the secondary instability, a higher growth rate was measured; its maximum value, β_{Tu} = 44.8m^{-1}, was registered at G_θ = 11.0; downstream, a continuous decrease of its value is observed. It is evident that the secondary instability grows faster compared to the first one. This observation agrees with the experimental results of Swearingen & Blackwelder (1987) and of Bippes (1972). The ratio of the maximum growth rate value of the secondary instability to the one of the first instability is equal to 3.7 (compared to 2.5 which was observed by Swearingen & Blackwelder (1987)).

3.2.3 Streamwise development of the boundary layer thickness and skin friction coefficient

As shown before, the inflow Blasius profile is clearly modified during the laminar-to-turbulent transition process in a concave plate. The Görtler vortices generate a wavy boundary layer in the spanwise direction resulting in thicker velocity profiles at the upwash location and thinner ones at the downwash location. In order to quantify this change in the boundary layer, the displacement thickness, δ^*, as well as the momentum thickness, θ, are plotted in Figure 3.10. A spanwise average value of this parameters is shown, along with the local values at the upwash and downwash regions. Additionally, the theoretical laminar and turbulent solutions of a flat plate are plotted for comparison. The laminar curves show the Blasius solution which is not affected by the surface curvature if $Re \to \infty$ (Floryan & Saric 1982). In fact, simulations without any perturbation were performed and there were only negligible differences between the obtained flow field and the Blasius solution (see Section 2.5.3.2), similar to the findings of Schrader et al. (2011). Regarding the plotted turbulent theoretical solutions of δ^* and θ, they are computed using the Prandtl's one-seventh-power law relationships (Eq. 1.16 and 1.17, respectively).

From Figure 3.10, it is seen that the boundary layer follows the laminar Blasius solution at first. However, as the flow evolves downstream, the Görtler vortices modify the base flow and a departure from the laminar theoretical solution is observed. From $G_\theta \sim 5.5$, a noticeable divergence of δ^* can be seen in such a way that the thickness increases in the upwash region and decreases in the downwash region. Nevertheless, the spanwise average curve follows the Blasius solution for a little longer. Downstream, maximum and minimum values, of δ^* and θ, are reached, which are followed by a convergence behavior of the upwash and downwash curves. A spanwise homogeneous flow is observed from $G_\theta \sim 21$ which can be explained by the increased mixing in the turbulent region. It is noted that the spanwise average curve of δ^* follows closely the turbulent theoretical solution but in the case of θ

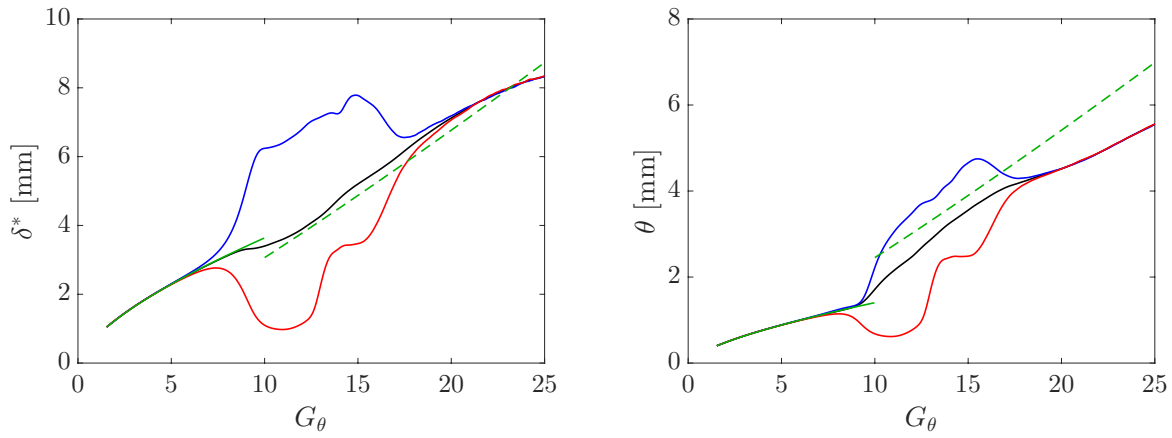

Figure 3.10: (a) Streamwise development of δ^*. (b) Streamwise development of θ. (——) Spanwise average, (——) upwash, (——) downwash, (——) Blasius solution and (- - -) turbulent theoretical solution.

lower values are found, indicating a less momentum boundary layer deficit in the concave surface, compared to the flat plate case. A similar flow behavior of δ^* and θ was observed experimentally by Swearingen & Blackwelder (1987) and Tandiono et al. (2008). However, the spanwise homogeneous region was not reached (just the convergence tendency of the upwash and downwash regions) because the streamwise length of their experiment set up did not allow it.

The local wall shear stresses in the streamwise direction, τ_w, are also a pertinent parameter to understand the transition process. As expected, due to the spanwise variation of the boundary layer thickness, they also vary with maximum and minimum values at the downwash and upwash regions, respectively. In the upwash region, the boundary layer is elongated which relaxes the wall shear stresses. In the downwash region, the flow is pushed towards the wall producing thereby an increase in the wall shear stresses. The non-dimensional parameter for the representation of τ_w is the skin friction coefficient, C_f, which, recalling Eq. (1.9), is expressed as: $C_f = \frac{\tau_w}{0.5\rho {U_\infty}^2}$.

The skin friction coefficient is plotted in Figure 3.11, where it is observed that C_f follows very well the laminar Blasius solution at the beginning (with a small variation at the location of the wall-roughness elements). Later, due to the development of the Görtler vortices, a departure from the laminar theoretical curve becomes noticeable from $G_\theta \sim 5.2$. Nevertheless, the spanwise average curve keeps following the Blasius curve longer after and reaches a minimum value at $G_\theta = 7.8$. After this point, a sudden increase in the wall shear stresses occur, which is correlated with the growth of the mushroom-like structure in the upwash region (Figure 3.1). In fact, it corresponds to the nonlinear region in the transition process (the region that occurs once the primary instability has saturated). The sudden increase culmi-

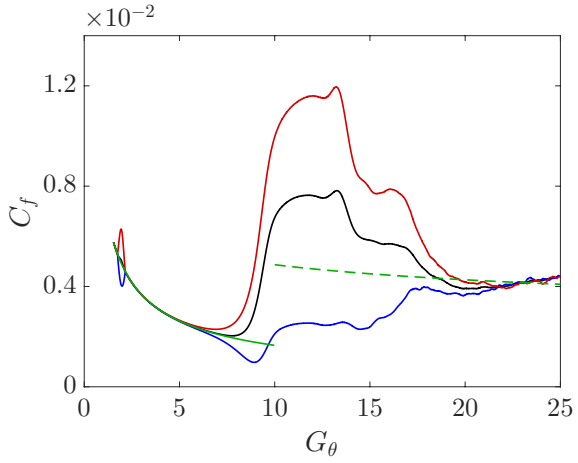

Figure 3.11: Streamwise development of the skin friction coefficient, C_f. (——) Spanwise average, (——) upwash, (——) downwash, (——) Blasius solution and (- - -) turbulent theoretical solution.

nates with a local maximum value of the spanwise average curve occurring at $G_\theta = 11.8$. The region followed after this point, is called the transition region, by Tandiono et al. (2009), and it is a region where the secondary instabilities develop. This region is also characterized by the converging behavior of the upwash and downwash curves towards a spanwise homogeneous turbulent flow, which occurs due to increased mixing taking place once the secondary instabilities break down into turbulence. The convergence point occurs at $G_\theta = 21.8$ and it marks the end of the transition process, and the start of the full turbulent region.

It is also interesting to highlight that the flat plate turbulent values of C_f are clearly surpassed by the spanwise average curve, by up to 70%, during the transition process. This behavior was also observed, both experimentally (Swearingen & Blackwelder 1987, Tandiono et al. 2009) and numerically (Schrader et al. 2011). Girgis & Liu (2006) explain the overshoot of the wall shear stresses by the effects of the unsteady secondary instabilities. In this study, similar to the experimental data of Swearingen & Blackwelder (1987), after the overshoot, the C_f spanwise average curve tends to follow the theoretical flat plate turbulent curve. However, on other studies (Tandiono et al. 2009, Schrader et al. 2011), this behavior could not be observed because the streamwise length of the analyzed concave plate was not long enough.

3.3 Parametric studies

In this section, a set of parametric studies are presented in which the roughness elements height, h, the radius of curvature, R, the streamwise location of the wall-roughness elements, Re_ξ^{rgh}, as well as the spanwise wavelength, Λ, are varied, separately, in order to study their influence on the starting point of the transition process. Moreover, a paramet-

ric study using a wall-roughness bump geometry, instead of a bump-dimple geometry, is presented.

3.3.1 Effect of the wall-roughness elements height

For this parametric study, the height of the wall-roughness elements, h, is varied from $0.01\delta^*$ to $0.2\delta^*$. The streamwise location of the wall-roughness elements center is the same as for the baseline case, i.e., $Re_\xi = 18274$. The computational domain is the same as that used for the baseline simulation which has a radius of curvature $R = 1$ m. For these studies, the starting point of the transition is measured at the location where the spanwise average of the wall shear stresses has its minimum value. This point is called the critical Görtler number, $G_{\theta_{cr}}$, and it occurs just before the sudden increase of C_f that characterizes the nonlinear region of the transition process. In Figure 3.12, it can be observed that the onset of the transition process is highly receptible to the variation of the roughness elements height. Moreover, a clear trend for $G_{\theta_{cr}}$ can be found. The transition starting point is brought forward as the height of the wall-roughness elements is increased, following a power law scale of $G_{\theta_{cr}} \propto (h/\delta^*)^{-0.1095}$. This power law was determined by a least-square fit. The observed trend is in accordance with the receptivity study of Schrader et al. (2011) where it is found that the Görtler mode saturates earlier as the height of their utilized wall-roughness elements is increased.

3.3.2 Effect of the radius of curvature

As a second parametric study, the radius of curvature, R, of the concave surface is varied from 0.75 m to 1.5 m. The transition is triggered by using the baseline wall-roughness elements, which have a height of $h/\delta^* = 0.01$ and their center at $Re_\xi = 18274$, for all the cases. In Figure 3.13, the streamwise development of the skin friction coefficient is plotted for the four cases. In Figure 3.13a, Re_ξ is used in the horizontal axis to show the effect of the radius of curvature on the onset of the transition process; the critical Reynolds number, Re_{cr}, is clearly delayed as R decreases. However, when the Görtler number is used in the horizontal axis (Figure 3.13b), a common transitional point for all cases is observed. In fact, there is a slight increase of $G_{\theta_{cr}}$ as R decreases, going from $G_{\theta_{cr}} = 7.6$ to 7.9, and following a linear behavior. However, more cases would be needed to observe if this linear behavior remains outside the computed range. The development of the local C_f at the upwash and downwash regions is plotted in Figure 3.13c in order to extend the spanwise characterization of the transition process for different R. An interesting trend is that, in the downwash location, the maximum C_f, reached after the sudden increase, decreases as R increases. On the other hand, the lowest C_f in the upwash location, is much less affected by the change in R. The general effect can be seen in the spanwise average of C_f that reach higher values as R decreases. Nevertheless, Figure 3.13a shows that, downstream, C_f tends to have a same magnitude regardless of R.

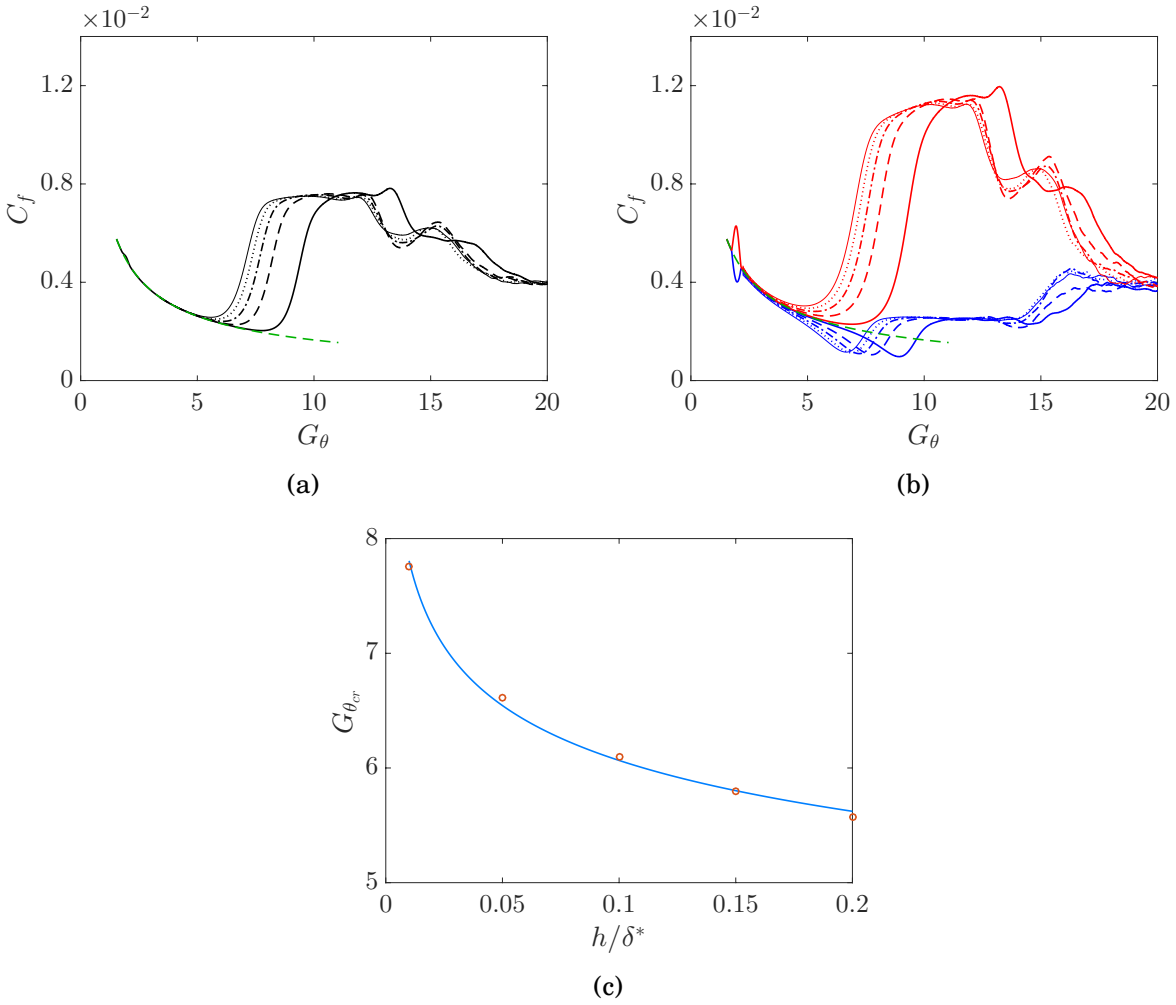

Figure 3.12: Streamwise development of C_f for different h/δ^*. (a) Spanwise-averaged C_f versus G_θ. (——) $h/\delta^* = 0.01$, (- - -) $h/\delta^* = 0.05$, (–·–) $h/\delta^* = 0.10$, (·····) $h/\delta^* = 0.15$, (——) $h/\delta^* = 0.20$ and (- - -) Blasius solution. (b) C_f at upwash and downwash versus G_θ. (——) Downwash curves, (——) upwash curves (c) Critical Görtler number versus roughness elements height, h/δ^*. (∘) $G_{\theta_{cr}}$ at different h/δ^*, (——) $G_{\theta_{cr}} \propto (h/\delta^*)^{-0.1095}$.

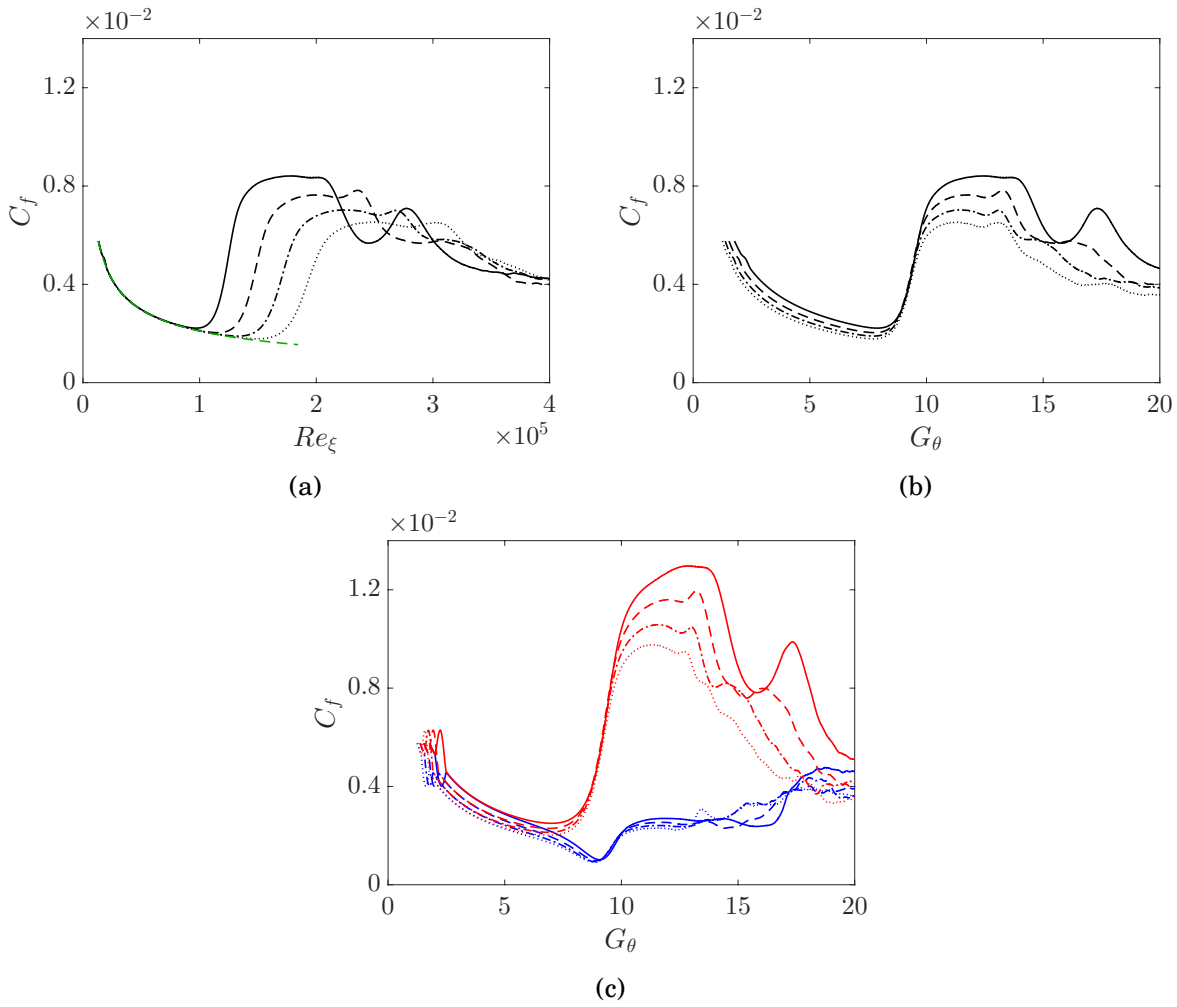

Figure 3.13: Streamwise development of C_f for different R. (a) Spanwise-averaged C_f versus Re_ξ. (——) R = 0.75 m, (- - -) R = 1 m, (–·–) R = 1.25 m, (·····) R = 1.5 m and (- - -) Blasius solution. (b) Spanwise-averaged C_f versus G_θ. (c) C_f at upwash and downwash versus G_θ. (——) Downwash curves, (——) upwash curves.

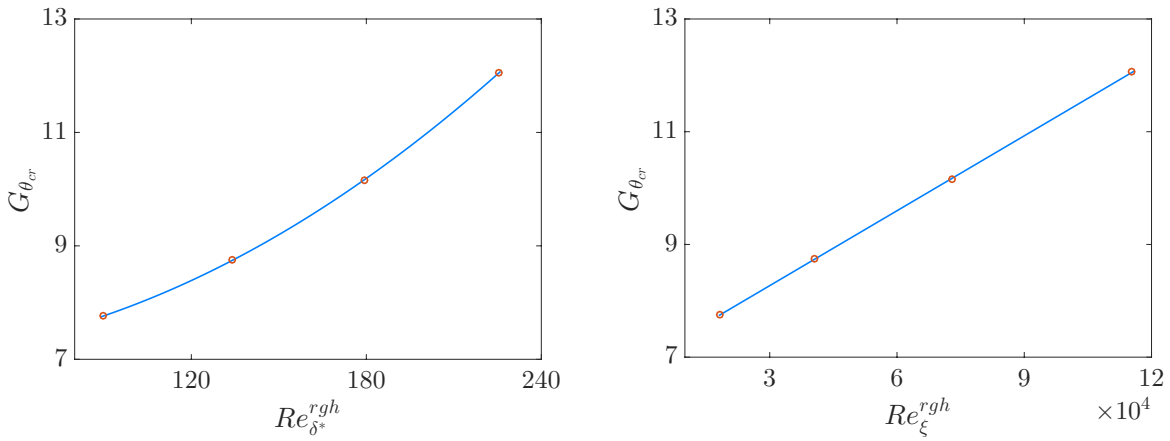

Figure 3.14: $G_{\theta_{cr}}$ as a function of the wall-roughness elements streamwise location. (a) $G_{\theta_{cr}}$ versus $Re^{rgh}_{\delta^*}$. (o) $G_{\theta_{cr}}$ at different $Re^{rgh}_{\delta^*}$, (——) $G_{\theta_{cr}} = 1.03 \times 10^{-4}(Re^{rgh}_{\delta^*})^2 + 8.71 \times 10^{-4}(Re^{rgh}_{\delta^*}) + 7.01$. (b) $G_{\theta_{cr}}$ versus Re^{rgh}_{ξ}. (o) $G_{\theta_{cr}}$ at different Re^{rgh}_{ξ}, (——) $G_{\theta_{cr}} = 4.43 \times 10^{-5}(Re^{rgh}_{\xi}) + 6.94$.

3.3.3 Effect of the wall-roughness elements streamwise location

In this parametric study, the streamwise location of the wall-roughness elements, Re^{rgh}_{ξ}, is varied from 18274 to 115271 in order to observe how the transition starting point is affected. This is equivalent to a variation of the Reynolds number based on δ^*, $Re^{rgh}_{\delta^*}$, from 90 to 225. The height of the wall-roughness elements is equal to $h = 0.01\delta^*$ for all the cases. Moreover, the baseline computational domain is used, which has a radius of curvature $R = 1$ m. In Figure 3.14a, $G_{\theta_{cr}}$ is plotted versus $Re^{rgh}_{\delta^*}$ showing how the transition point is delayed as the location of the wall-roughness elements is moved downstream. A least-square fit determined a second-order polynomial behavior:

$$G_{\theta_{cr}} = 1.03 \times 10^{-4}(Re^{rgh}_{\delta^*})^2 + 8.71 \times 10^{-4}(Re^{rgh}_{\delta^*}) + 7.01. \tag{3.2}$$

However, Figure 3.14b shows that when $G_{\theta_{cr}}$ is plotted against Re^{rgh}_{ξ}, a linear behavior is followed. A least-square fit determined a linear equation:

$$G_{\theta_{cr}} = 4.43 \times 10^{-5}(Re^{rgh}_{\xi}) + 6.94. \tag{3.3}$$

Even though an extrapolation of the results should be done with caution, both obtained equations suggest that, for the utilized bump-dimple geometry with $h = 0.01\delta^*$, the starting point of the transition process will not occur before $G_\theta \cong 7$, *i.e.*, for the limiting case when $Re^{rgh}_{\xi} \to 0$, or $Re^{rgh}_{\delta^*} \to 0$.

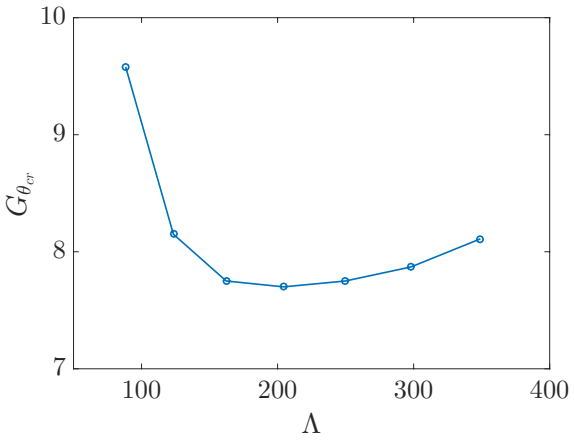

Figure 3.15: Streamwise transition location, $G_{\theta_{cr}}$, for different spanwise wavelengths, Λ.

3.3.4 Effect of the wall-roughness elements spanwise wavelength

Here, the impact of the wall-roughness elements dimensionless wavelength on the transition location is analyzed. The wall-roughness elements wavelength, which presets the Görtler vortices wavelength, is varied from $\Lambda = 88.3$ to 349.1. The computational domain used for each case had a Radius of curvature $R = 1$ m. However, the spanwise length was adapted so that in each case four Görtler vortices could develop. The obtained results are plotted in Figure 3.15. It is observed that transition starts earlier for the cases within the range from $\Lambda = 162$ to 250. These results are in accordance with the ones obtained from linear stability theory where it was found that a maximum growth of the Görtler vortices occurs when Λ is within the range of 200-270 (Floryan 1991, Smith 1955, Meksyn 1950).

Another point to highlight is that the spanwise wavelength of the Görtler vortices has an impact on the type of secondary instability that develops. The baseline case with $\Lambda = 250$ only allowed to excite the varicose mode that is linked to the appearance of horseshoe vortices (see Section 3.2.2). On the other hand, the sinuous mode, linked to the meandering motion of the Görtler vortices, could not be excited. In order to appreciate weather this secondary mode is present or not, the streamwise velocity contours at the wall-normal location $\eta = 0.1\delta_{Blasius}$ are plotted, for two wavelengths, in Figure 3.16. In the baseline case (Figure 3.16a), the sinuous mode is absent and a straight development of the upwash (at $z/\lambda = 0.25$) and downwash regions (at $z/\lambda = 0.75$) is observed. However, by plotting the velocity contours for a case with a smaller wavelength ($\Lambda = 162$), in Figure 3.16b, a clear oscillatory motion can be observed. From $G_\theta = 14.6$, a wavy (or sinuous) motion on the upwash region (mushroom-like structure location) can be appreciated, which indicates the presence of the odd secondary mode. These results are in accordance with the observations of Li & Malik (1995) who measured the growth of the secondary instabilities for three different cases, i.e ., $\Lambda = 159$, 451 and 1275, finding that the shorter wavelength cases have a stronger tendency to develop

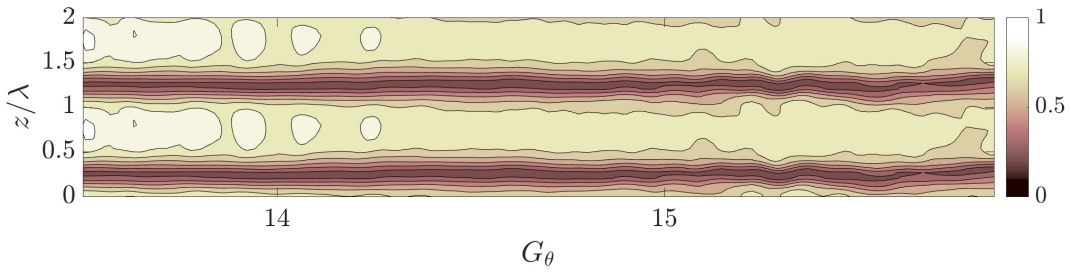

(a) $\Lambda = 250$

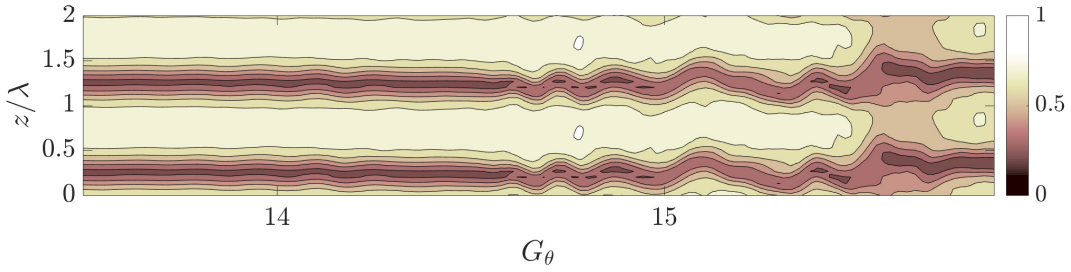

(b) $\Lambda = 162$

Figure 3.16: Streamwise velocity U/U_∞ contours at the wall-normal location $\eta = 0.1\delta_{Blasius}$ showing the presence or absence of the secondary sinuous instability for $\Lambda = 250$ and 162.

odd modes. This behavior being associated to a an increase in the spanwise shear gradients with respect to the wall-normal shear gradients.

3.3.5 Effect of a wall-roughness bump geometry

In this section, in order to investigate the effect of the wall-roughness geometry on the transition location, a bump geometry, instead of a bump-dimple geometry, is utilized for exciting the Görtler vortices. Three different configurations for the sinusoidal bump geometry are utilized. The tested geometries are illustrated in Figure 3.17 in which, for a better appreciation, the complete domain in the spanwise direction is shown. In the first configuration (case-A, see Figure 3.17a), the bump has a spanwise length of 6 mm followed by a flat space of 6 mm. This configuration allowed to have four bumps in the spanwise direction. It is noted that this case is identical to the baseline case with the difference that the dimple is replaced by a flat surface. The second configuration (case-B, see Figure 3.17b) consists in a bump with a spanwise length of 12 mm without any flat space in between the bumps. This configuration also allowed to have four bumps. For case-B, the roughness element wavelength is the same as the one used in the baseline case; only the half-bump/half-dimple geometry is replace by a full length bump geometry. The third configuration (case-C, see Figure 3.17c) consists in a bump with a spanwise length of 12 mm and a flat empty space of 12 mm in between the bumps. This configuration allowed to have two bumps. This third configuration is in between the two previous cases in the sense that while it has a flat space between two

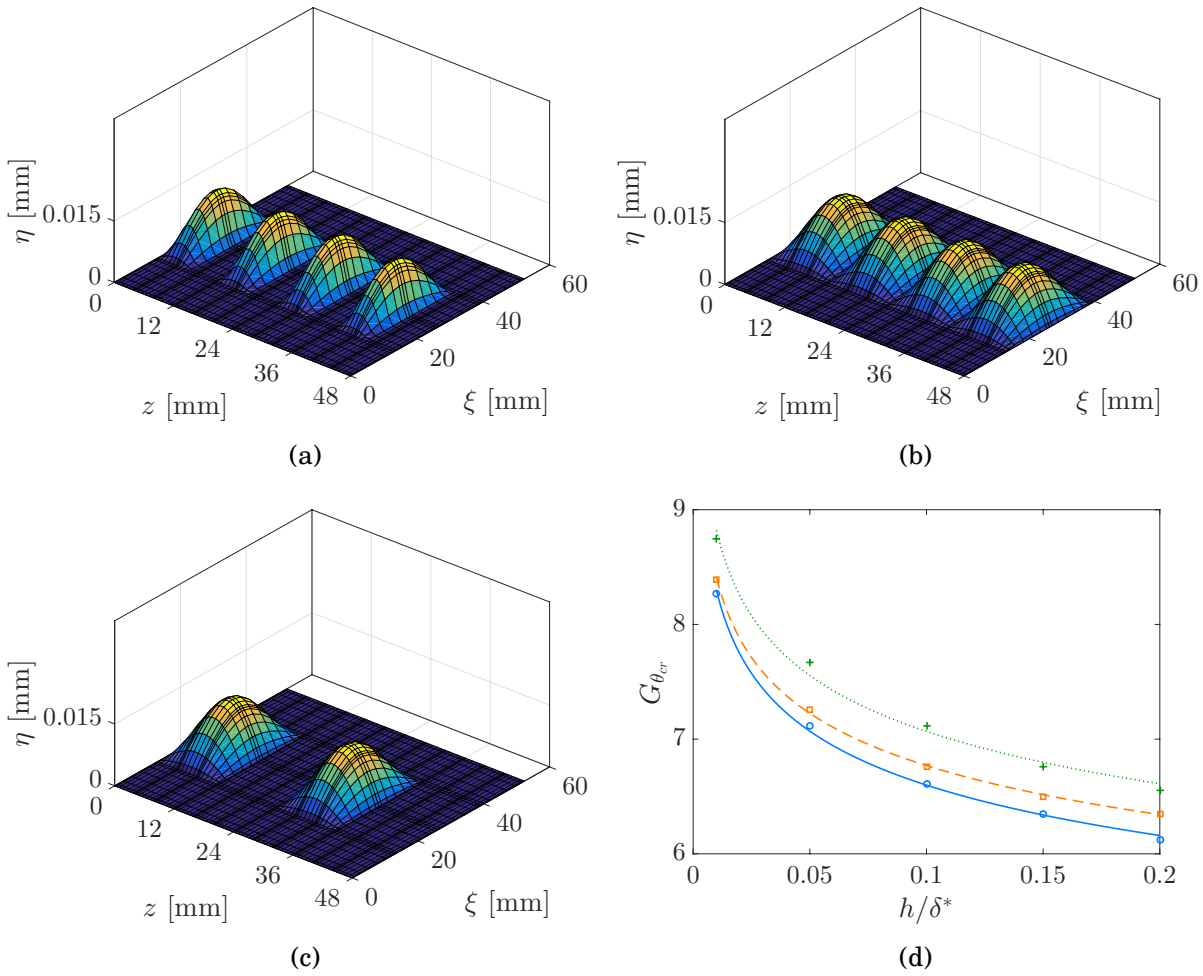

Figure 3.17: $G_{\theta_{cr}}$ vs. h/δ^* for different wall-roughness bump geometries. (a) Geometry case-A. (b) Geometry case-B. (c) Geometry case-C. (d) (∘) Case-A, (——) $G_{\theta_{cr}} \propto (h/\delta^*)^{-0.0993}$, (▫) case-B, (- - -) $G_{\theta_{cr}} \propto (h/\delta^*)^{-0.0941}$, (+) case-C, (·····) $G_{\theta_{cr}} \propto (h/\delta^*)^{-0.0962}$.

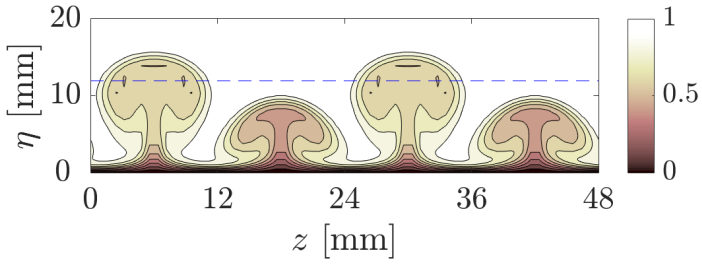

Figure 3.18: Streamwise velocity, U/U_∞, contours at $G_\theta = 12$ for case-C.

bumps (similar to case-A), the bump has a spanwise length of 12 mm (similar to case-B).

In this parametric study, the height of the bumps, h, for the three configurations, is varied from $0.01\delta^*$ to $0.20\delta^*$. Besides, the computational domain is the same as that used for the baseline simulation which has a radius of curvature $R = 1$ m. It is noted that all three configurations allowed to excite four pairs of Görtler vortices. However, in case-C, two mushroom-like structures start to grow later than the other two (see Figure 3.18), delaying the transition starting point location. Meanwhile, in case-A and case-B the four pairs of Görtler vortices grow at the same time (not shown here), similar to the baseline case.

In Figure 3.17d the transition point, $G_{\theta_{cr}}$, is plotted against the bump height, h/δ^*. It is observed that, with the case-A configuration, transition starts earlier. On the other hand, the transition is delayed when the case-C is used. Similar to the bump-dimple geometry, the different cases for the bump geometries also follow power laws, which were determined by a least-square fit. Also, the variation of the transition starting point with the wall-roughness geometry height has the same order of magnitude and it is followed by $G_{\theta_{cr}} \propto (h/\delta^*)^{-0.0993}$, $G_{\theta_{cr}} \propto (h/\delta^*)^{-0.0941}$ and $G_{\theta_{cr}} \propto (h/\delta^*)^{-0.0962}$, for case-A, case-B and case-C, respectively. As it can be seen, although all three cases generate the same flow features, when compared to a bump-dimple geometry, they are less efficient for exciting the transition of the laminar flow.

3.4 Fully turbulent flow

In this section, the fully turbulent region, product of the transition initiated by the Görtler vortices, is analyzed. It is reminded that the baseline case with $R = 1$ m and wall-roughness elements with $h = 0.01\delta^*$ is utilized for the current analysis.

As mentioned before, after the streamwise position $G_\theta = 21.8$ the flow reaches a fully turbulent regime where the upwash and downwash regions are no longer distinguishable and a spanwise homogeneity can be observed. In order to characterize this flow region, in Figure 3.19, the spanwise averaged velocity profile is plotted in wall units at $G_\theta = 23.8$, which corresponds to $Re_\theta = 1006$; where $Re_\theta = U_\infty\theta/\nu$. The wall units are defined as $U^+ = \langle\overline{U}\rangle/u_\tau$ and $y^+ = u_\tau\eta/\nu$; where u_τ is the friction velocity defined as $u_\tau = \sqrt{\langle\tau_w\rangle/\rho}$ (noticing that the brackets $\langle\,\rangle$ represent a spanwise-averaged quantity). In the viscous sublayer, which corresponds to

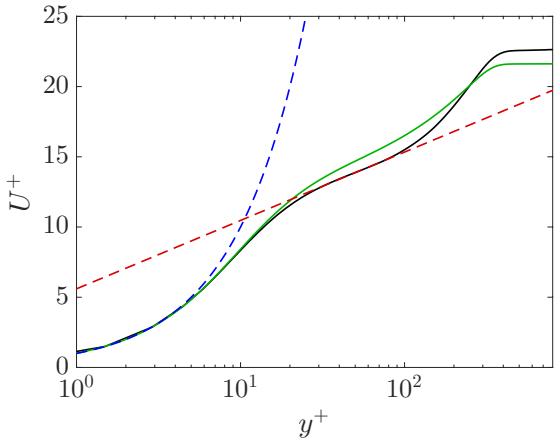

Figure 3.19: U^+ vs. y^+ at $Re_\theta = 1006$. (——) Concave plate, (——) flat plate from Schlatter & Örlü (2010), (- - -) $U^+ = y^+$ and (- - -) $U^+ = \kappa^{-1}\log y^+ + B$; where $\kappa = 0.47$ and $B = 5.6$.

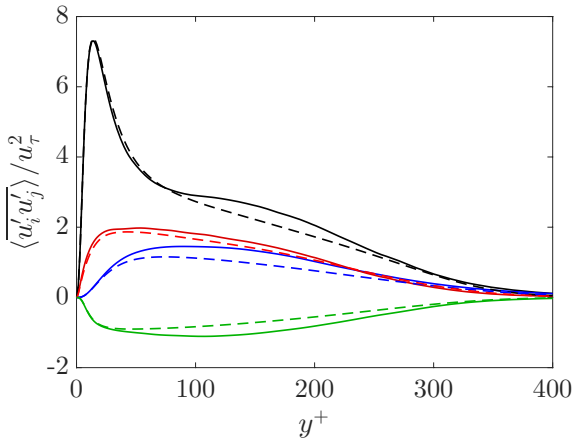

Figure 3.20: Reynolds stresses normalized by the friction velocity at $Re_\theta = 1006$. (——) $\langle \overline{u'^2} \rangle / u_\tau^2$ concave plate, (——) $\langle \overline{v'^2} \rangle / u_\tau^2$ concave plate, (——) $\langle \overline{w'^2} \rangle / u_\tau^2$ concave plate, (——) $\langle \overline{u'v'} \rangle / u_\tau^2$ concave plate, (- - -) $\langle \overline{u'^2} \rangle / u_\tau^2$ from Schlatter & Örlü (2010), (- - -) $\langle \overline{v'^2} \rangle / u_\tau^2$ from Schlatter & Örlü (2010), (- - -) $\langle \overline{w'^2} \rangle / u_\tau^2$ from Schlatter & Örlü (2010) and (- - -) $\langle \overline{u'v'} \rangle / u_\tau^2$ from Schlatter & Örlü (2010).

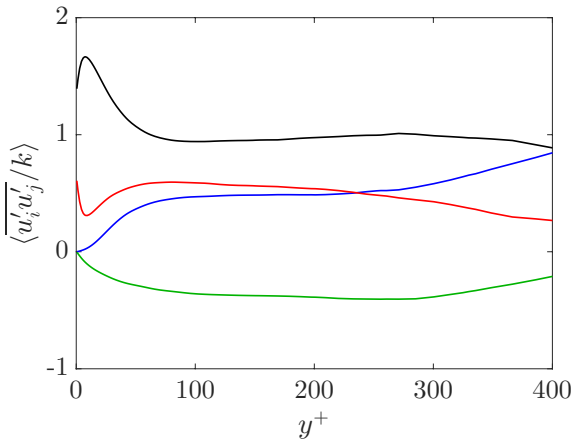

Figure 3.21: Reynolds stresses, normalized by the turbulence kinetic energy, at $Re_\theta = 1006$. (——) $\langle \overline{u'^2}/k \rangle$, (——) $\langle \overline{v'^2}/k \rangle$, (——) $\langle \overline{w'^2}/k \rangle$ and (——) $\langle \overline{u'v'}/k \rangle$.

$y^+ < 5$, the velocity profile follows the linear relation $U^+ = y^+$. The buffer layer situated between the viscous sublayer and the log-law region corresponds to $5 < y^+ < 30$. The log-law region corresponds to $30 < y^+ < 80$; it follows the law $U^+ = \kappa^{-1} \log y^+ + B$ with $\kappa = 0.47$ and $B = 5.6$. The DNS results obtained by Schlatter & Örlü (2010) over a flat plate are also shown for comparison; this data corresponds to the streamwise position $Re_\theta = 1006$, where the flow is in fully turbulent regime. The Reynolds stresses normalized by the friction velocity, at the same streamwise position, are shown in Figure 3.20. The results obtained by Schlatter & Örlü (2010), also at $Re_\theta = 1006$, are shown for comparison. The profiles of the Reynolds stresses normalized by the turbulence kinetic energy, k, are shown in Figure 3.21. It is observed that they are uniform in a great range; their values are given in Table 3.1.

Reynolds stress	Peak $y^+ = 7.9$	Log-law $y^+ = 80$
$\langle \overline{u'^2}/k \rangle$	1.67	0.95
$\langle \overline{v'^2}/k \rangle$	0.02	0.46
$\langle \overline{w'^2}/k \rangle$	0.31	0.59
$\langle \overline{u'v'}/k \rangle$	-0.09	-0.34

Table 3.1: Reynolds stresses statistics at $Re_\theta = 1006$

Finally, in order to highlight the breakdown into turbulence of the secondary instabilities, the vortical coherent structures are depicted in the second half of the domain using the λ_2 criterion in Figure 3.22.

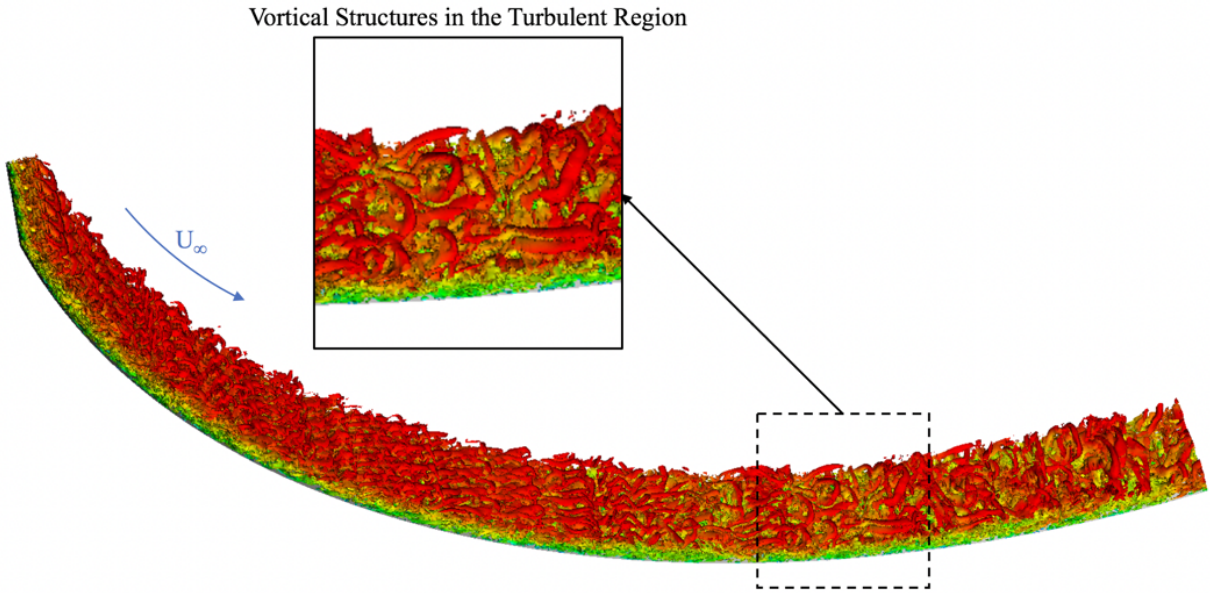

Figure 3.22: Vortical coherent structures obtained with iso-surfaces of $\lambda_2 = -125$. Sub-domain bounded from $\phi_{loc} = 90°$ to 180°.

Chapter 4
Transitional thermal boundary layer and surface heat transfer

4.1 Introduction

The results presented in this chapter have been accepted, with minor revisions, to be published in the scientific journal *Physics of Fluids* (Méndez et al. 2020).

The development of a thermal-boundary layer during the laminar-to-turbulent transition process over a concave surface is studied in this chapter. Direct numerical simulations (DNS) are performed where the temperature variable is treated as a passive scalar. The laminar flow is perturbed with wall-roughness elements that are able to produce centrifugal instabilities in the form of Görtler vortices with maximum growth rate. It is found that Görtler vortices are able to greatly modify the surface heat-transfer by generating a spanwise periodic distribution of the temperature. Similar to the Görtler momentum boundary layer, elongated mushroom-like structures of low-temperature are generated in the upwash region, whereas, in the downwash the thermal boundary layer is compressed. Consequently, temperature gradients are increased and decreased in the downwash and upwash regions, respectively, generating thereby an overall enhancement of the heat-transfer rate of $\sim 400\%$ for the investigated Prandtl numbers ($Pr = 0.72$, $Pr = 1$ and $Pr = 7.07$). This enhancement surpasses the turbulent heat-transfer values during the transitional region, characterized by the development of secondary instabilities. However, downstream, the heat-transfer rate decays to the typical turbulent values. Streamwise evolution of several thermal quantities such as temperature wall-normal distribution, thermal boundary layer thickness and Stanton number are reported in the different regions encountered in the transition process, namely linear, nonlinear, transition and fully turbulent regions. These quantities are reported locally at upwash and downwash regions, where they present minima and maxima, as well as globally as spanwise-averaged quantities. Furthermore, it is found that the Reynolds analogy between streamwise-momentum and heat-transfer holds true throughout the whole transition process for the $Pr = 1$ case. Moreover, the turbulent thermal boundary layer over a concave surface is analysed in detail for the first time. The viscous sub-layer as well as the log-law region are described for each investigated Pr. Besides, the rms (root-mean-squared) temperature fluctuations are computed finding that its wall-normal distribution exhibits a higher peak when Pr is increased.

4.2 Simulation setup

The same numerical approach and computational set-up utilized for the momentum boundary layer analyses presented in Chapter 3 are used here. They were described in Chapter 2. However, some additional considerations have to be taken into account for computing the temperature field, which had not been computed for the previous analyses.

4.2.1 Energy equation

Regarding the fluid dynamics equations that govern the flow motion, as explained in Section 2.1, the incompressible assumption enabled to uncouple the continuity (Eq. 2.1) and momentum (Eq. 2.2) equations from the energy equation (Eq. 4.1). This approach allowed to avoid the computation of the energy equation since its solution was not needed to advance the flow. Nevertheless, for the current thermal analyses, the temperature variable, T, has to be obtained and it is done by treating it as a passive scalar. For that, after obtaining velocity and pressure fields by solving the continuity and momentum equations, the temperature field is computed by solving the energy equation. This equation is recalled here:

$$\rho c_p(\partial_t T + \mathbf{U}\cdot\nabla T) = \nabla\cdot(k_{th}\nabla T) + q_{vol}, \tag{4.1}$$

It is important to mention that on a passive scalar analysis, the species that is transported within the flow, which in this case is the temperature, has no dynamical effect on the fluid motion itself. This approach is valid for small temperature differences throughout the flow whose influence in the flow dynamics is rather weak and can be neglected. The energy conservation equation (4.1) is then considered a convection-diffusion transport equation for the temperature scalar quantity.

4.2.2 Computational setup

Flow properties

As for the fluid properties, as mentioned previously, three different fluid Prandtl numbers are considered, namely $Pr = 0.72$, $Pr = 1$ and $Pr = 7.07$. This non-dimensional number relates the momentum diffusivity (or kinematic viscosity), ν, to the thermal diffusivity, α_{th}, as:

$$Pr = \frac{\nu}{\alpha_{th}} = \frac{\mu/\rho}{k_{th}/\rho c_p} = \frac{c_p\mu}{k_{th}}. \tag{4.2}$$

It is important to point out that one of the main objectives of the current study is to analyse and compare the modification of the thermal boundary suffered by fluids with different thermal properties, i.e. different Pr. This is done with an analysis in which the spatial development of the momentum boundary layer is the same regardless of the fluid Prandtl number. Such analysis is possible to be performed due to the fact that the temperature is

treated as a passive scalar, which means that it does not have any influence in the flow dynamics, as previously explained. However, since the kinematic viscosity, ν, is different for each fluid, the free-stream velocity is changed in order to ensure a mechanical similarity in all the analysed situations (see Table 4.1). This similarity is imposed in such a way that the Reynolds number based in the streamwise position, Re_ξ, varies equally in the three analysed cases. The domain thus goes from $Re_\xi = 1.33 \times 10^4$, at the inlet, to $Re_\xi = 6.1 \times 10^5$, at the outlet, in every case.

Each Prandtl number case is then simulated differently. Table 4.1 summarizes the parameters that were varied for each Pr case. The kinematic viscosity, ν, as well as the thermal diffusivity, α_{th}, are selected according to the standard conditions of the simulated fluid. The $Pr = 0.72$ case simulates air at standard conditions. To notice is that this case matches the numerical conditions of Méndez *et al.* (Méndez et al. 2018) as well as the experimental set up of Tandiono *et al.* (Tandiono et al. 2009). The thermal boundary layer computed in the current study is compared with the momentum boundary layer presented by Méndez *et al.* (Méndez et al. 2018), mainly to verify the Reynolds analogy. Nevertheless, a comparison with the results of Tandiono *et al.* (Tandiono et al. 2009) was not possible due to the fact that in the authors' experiments some free-stream turbulence intensity ($\sim 0.45\%$) was presented and produced an earlier transition. For the $Pr = 1$ case, the same free-stream velocity is utilized ($U_\infty = 2.85$ m/s) . However, in order to have a Prandtl number of unity, it is imposed that $\alpha_{th} = \nu$. Next, the case with $Pr = 7.07$ correspond to the properties of water at standard conditions. Finally, it is reminded that the flow is considered to be incompressible (constant density) in all the cases.

Pr	U_∞ m/s	ν m^2/s	α_{th} m^2/s
0.72	2.85	1.5×10^{-5}	2.1×10^{-5}
1.00	2.85	1.5×10^{-5}	1.5×10^{-5}
7.07	0.21	1.1×10^{-6}	1.6×10^{-7}

Table 4.1: Free-streamwise velocity, U_∞, kinematic viscosity, ν and thermal diffusivity, α_{th}, imposed in each analysed case.

Furthermore, every case is simulated with a free-stream temperature of $T_\infty = 288K$. However, the non-dimensional temperature, θ_{th}:

$$\theta_{th} = \frac{T - T_w}{T_\infty - T_w}, \tag{4.3}$$

will be preferred for the characterization of the temperature field. Hence, the non-dimensional free-stream temperature is $\theta_{th} = 1$.

Boundary and initial conditions

Regarding the boundary conditions, the same ones utilized for the momentum boundary layer are kept (see Figure 2.8). A laminar Blasius profile with $Re_\xi = 1.33 \times 10^4$ is imposed at the inlet. At the outer radius surface, a wall boundary condition is imposed (no slip condition, $\mathbf{U} = 0$), whereas, at the inner radius, a tangential velocity, U, equal to the free-stream velocity, U_∞, is imposed. At the exit, an outflow boundary condition was prescribed, where the normal stresses are zero. Nevertheless, some extra boundary conditions have to imposed for solving the energy equation. The theoretical thermal boundary layer profile for an incompressible steady flow was computed, for each Prandtl number, and imposed at the inlet. At the outer radius surface, a non-dimensional temperature $\theta_{th} = 0$ was imposed; whereas, at the inner radius, $\theta_{th} = 1$ was imposed, which is equal to the free-stream non-dimensional temperature. An outflow boundary condition was imposed at the outlet and periodic boundary conditions were imposed in the lateral surfaces.

Regarding the initial condition ($t = 0$), the two-dimensional (2D) Blasius flow solution is computed and imposed along the concave plate. Furthermore, in a similar fashion, for the temperature, the 2D theoretical thermal boundary layer profile for an incompressible steady flow was also computed and imposed along the computational domain.

Domain, grid and perturbation method

The same computational domain utilized for the momentum boundary layer analyses (see Figure 2.8 and Figure 2.9), that was presented in Section 2.5.2, is utilized for the current thermal studies. Furthermore, the same grid with polynomial order $N = 7$ is utilized as well (see Figure 2.9).

Besides, the same perturbation method, also presented in Section 2.5.2, is utilized. It consist of four wall-roughness elements with a wavelength of $\Lambda = 250$ that allows to trigger the Görtler vortices with maximum growth rate. Regarding the wall-roughness elements height, h, the baseline case ($h = 0.01\delta^*$) is utilized for the current thermal studies (see Figure 2.10).

4.3 Validation of the results

As shown in Section 2.5.1, the NEK5000 DNS solver has been largely validated for transitional and turbulent flows. Moreover, in Section 2.5.3, the correctness of the employed computational setup (grid, domain and boundary conditions) was verified. The correct computation of the perturbation-free base flow (i.e. laminar) was performed by comparing the solver results with the Blasius theoretical solution. Besides, the transitional flow was also validated by comparing the boundary layer response to localized wall-roughness with previous numerical studies. Furthermore, those validation studies allowed to conclude that a grid with $N = 7$ was sufficient to get a full DNS resolution of the transitional flow and that

the increase of this polynomial order does not affect the simulation results.

However, since the previously performed validation studies did not include the energy equation, the temperature field was not computed and its correct computation could not be validated. Therefore, a validation study of the thermal problem is performed in order to ensure the correct computation of the temperature field. For that, a perturbation-free flow, similar to the one analyzed in Section 2.5.3, is computed in order to analyse a laminar flow over a concave plate and compare the obtained results with the theoretical thermal boundary layer. Moreover, for this thermal validation test, the three different Prandtl numbers ($Pr = 1$, $Pr = 0.72$ and $Pr = 7.07$) are considered. Figure 4.1a shows the wall-normal profile of the non-dimensional temperature, θ_{th}, at $G_\theta = 20$, which corresponds to a Reynolds number based on the streamwise location of $Re_\xi = 4.07 \times 10^5$. To note is that the wall-normal coordinate, η, is non-dimensionalized with the theoretical thermal boundary layer thickness of a flow with $Pr = 1$, $\delta_{th,Pr=1}$. As seen, the obtained temperature profiles perfectly match the theoretical ones for the three Prandtl number cases. Furthermore, it is observed that the thermal boundary layer thickness is shortened with the increase of Pr; which results from the thermal diffusivity decrease. In Figure 4.1b, the streamwise development of the thermal boundary layer thickness, δ_{th}, along the concave plate is plotted and compared with the theoretical laminar values. It is shown that the computed results match the theoretical ones for the three cases. Moreover, the thickness of the theoretical thermal boundary layer behave as $\delta_{th} = \delta Pr^{-1/3}$; which indicates a similarity between δ_{th} and δ when $Pr = 1$. It is interesting to point out that these results allow to conclude that the centrifugal effects does not affect the laminar thermal boundary layer development; which is similar to the laminar momentum boundary layer over a concave wall that follows the Blasius solution as $Re_\xi \to \infty$ (Floryan & Saric 1982).

Next, the Stanton number, St, is plotted. This non-dimensional number measures the ratio of the heat transferred into the fluid to the thermal capacity of the fluid; and it is used to characterize heat transfer in forced convection flows. It is defined as:

$$St = \frac{h_{conv}}{\rho c_p U_\infty}, \tag{4.4}$$

where h_{conv} is the convection heat transfer coefficient. h_{conv} can be computed by assuming that the heat transfer at the surface occurs due to conduction, which leads to:

$$Q_w = h_{conv}(T_w - T_\infty) = k_{th} \left.\frac{\partial T}{\partial \eta}\right|_{\eta=0}, \tag{4.5}$$

where Q_w is the heat transfer from the wall with units of energy per unit area per unit time. The streamwise evolution of the Stanton number is then plotted in Figure 4.1c for the three cases. As it is seen, the computed heat transfer perfectly matches the one predicted theoretically. Moreover, it is seen that the heat transfer increases as the fluid Prandtl number decreases. This increase occurs due to a better thermal conductivity, k_{th}, of the fluid, which

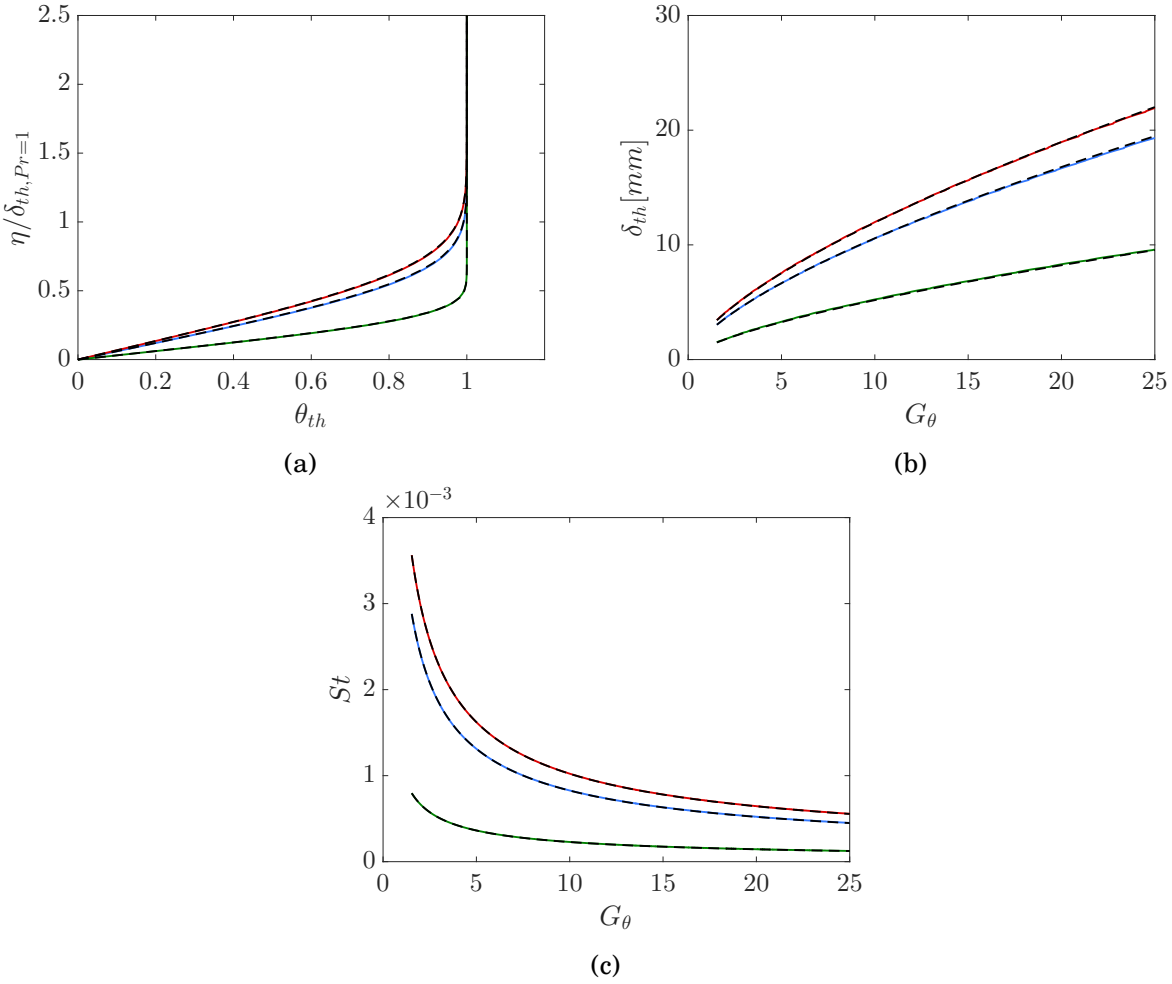

Figure 4.1: Comparison of the computed thermal laminar boundary layer developing over a concave surface with the theoretical solution. Three cases are shown: $Pr = 0.72$, $Pr = 1$ and $Pr = 7.07$. (a) Wall-normal profile of the non-dimensional temperature, θ_{th}, at $G_\theta = 20$. (b) Streamwise development of the thermal boundary layer thickness, δ_{th}. (c) Streamwise development of the Stanton number, St. (——) $Pr = 0.72$, (——) $Pr = 1$, (——) $Pr = 7.07$, and (- - -) theoretical thermal laminar boundary layer.

directly enhances the convection heat transfer coefficient, h_{conv}. Moreover, it can be noticed that the similarity between heat and streamwise-momentum, for the case $Pr = 1$, occurs since $St = C_f/2$.

In general, these results are able to validate the correct computation of a laminar and transitional boundary layer developing over a concave plate. Furthermore, the computed temperature field was validated for the laminar condition. The thermal behavior under transitional conditions can be considered to be validated by comparing the temperature field with the streamwise-velocity one for the case with $Pr = 1$ and showing that an analogy (i.e. equality) exists between these fields. This is done in the following section.

4.4 Thermal behavior of a transitional boundary layer

4.4.1 Temperature distribution

As mentioned, the flow is disturbed with wall-roughness elements that trigger the inception of four pairs of Görtler vortices. These primary instabilities clearly modify the original laminar Blasius flow by means of their rotating motion that creates a wavy velocity profile in the spanwise direction, where two regions are distinguished: upwash and downwash. Apart from modifying the velocity field, the vortex motion is also able to modify the temperature field (i.e. the original thermal laminar boundary layer) in the same fashion. In the upwash, thermal and momentum boundary layers are elongated due to the upward movement of the vortices; on the other hand, in the downwash, both boundary layers are compressed due to the vortices downward movement. The development of the thermal boundary layer for the three Prandtl number cases ($Pr = 1$, $Pr = 0.72$ and $Pr = 7.07$) is shown in Figures 4.2, 4.3 and 4.4, respectively. For that, contour plots of the non-dimensional temperature (contours from $\theta_{th} = 0.1$ to 0.9 with a step of 0.1) are shown for the streamwise positions $G_\theta = 8$, 9, 10 and 12. This positions correspond to the non-linear region of the transition process (primary instability growth and saturation). Furthermore, the theoretical thermal boundary layer thickness of a fluid with $Pr = 1$, $\delta_{th,Pr=1}$, is plotted in all charts for comparison. The first case to analyze is the one with $Pr = 1$, which is shown in Figure 4.2. As mentioned, this case is particularly relevant because of the analogy between non-dimensional temperature, θ_{th}, and non-dimensional streamwise velocity, U/U_∞. The depicted temperature distribution can be then compared with the velocity contours previously obtained (see Figure 3.1) in order to realize that both distributions are completely the same. This means that a mushroom-like structure, formed of low θ_{th}, also appears in the temperature field as the flow enters to the non-linear region. Furthermore, it is seen that this mushroom-like structure, located at the upwash, clearly surpasses the theoretical thermal laminar boundary layer thickness ($G_\theta = 12$); whereas, at the downwash, a reduction of δ_{th} is clearly noticed. The same behavior of the non-dimensional temperature distribution for $Pr = 1$ has also been observed by Liu & Lee (1995), who computed θ_{th} using a marching solution method and compared their results

with the velocity contours obtained experimentally by Swearingen & Blackwelder (1987).

With respect to the case with $Pr = 0.72$, which simulates air at standard conditions, it can be seen that a very similar development of the temperature distribution occurs (Figure 4.3). A spanwise wavy distribution is first noticed ($G_\theta = 8,9$) which is then followed by the development of a mushroom-like structure that also surpasses the theoretical thermal boundary layer thickness ($G_\theta = 10,12$). However, comparing the two cases, it is observed that the mushroom-like structures of the $Pr = 1$ case are less diffused. The same behavior was also observed by Liu & Lee (1995). The case with $Pr = 7.07$, which simulates water at standard conditions, is depicted in Figure 4.4. Here, the temperature wavy pattern is also observed ($G_\theta = 8$); however, the upwash growing structure is concentrated near the wall and, compared to the other cases, δ_{th} is clearly smaller. Downstream, in the non-linear region, at $G_\theta = 10$, the mushroom-like structure evolves into a thermal thin structure with a particular shape, different from the two previous cases, that presents two low-temperature regions "hanging" from the mushroom head at each extremity. Finally, a palm tree-like structure (as described by Liu & Lee (1995)) is observed at $G_\theta = 12$ with two regions of low temperature ($\theta_{th} = 0.9$ to 0.7) at its sides. The effect of a lower thermal diffusivity then results in lower-height palm tree-like structures. Nevertheless, it should be reminded that the momentum boundary layer is the same for the three cases (which is equal to the thermal one with $Pr = 1$).

In order to observe the growth and evolution of the mushroom-like structure, Figure 4.5 depicts the streamwise development of the non-dimensional temperature field, θ_{th}, in the non-linear transition region for the three Pr cases. Basically, equidistant contour plots of θ_{th} are shown at different streamwise positions ($G_\theta = 7.6, 8.5, 9.3, 10, 10.8, 11.5, 12.3$) together with an iso-surface, in yellow, with value of $\theta_{th} = 0.9$.

As explained, in the three cases the Görtler vortices swirl motion causes the appearance of a mushroom-like structure of low θ_{th} that is pushed from the surface. This phenomenon occurs at the upwash location. Then, in order to better appreciate the vortex effect at upwash and downwash locations during the non-linear region of the transition process, the evolution of the thermal boundary layer profile is shown in Figure 4.6 (locations at $G_\theta = 4$, 8, 9, 10 and 12 are plotted). For the case with $Pr = 1$, which is plotted in Figure 4.6a and Figure 4.6b, the non-dimensional temperature profiles have exactly the same shape as the streamwise velocity profiles that were previously computed (see Figure 3.6). As explained, the profiles match due to the Reynolds analogy. Moreover, for the three cases, at the first streamwise position that is plotted ($G_\theta = 4$), the Görtler vortices are not yet capable of modifying the temperature profile and it thus keeps the same shape as the theoretical profile, at both upwash and downwash locations. Nevertheless, in the upwash location, as the flow develops, the temperature profile departs from the initial solution and tends to become thinner and more elongated ($G_\theta = 8,9$). Further downstream, similar to the streamwise velocity profile (Figure 3.6), the upwash temperature profile also gets a highly inflectional S-shape form ($G_\theta = 10,12$). However, some differences can be noticed among the three cases. For

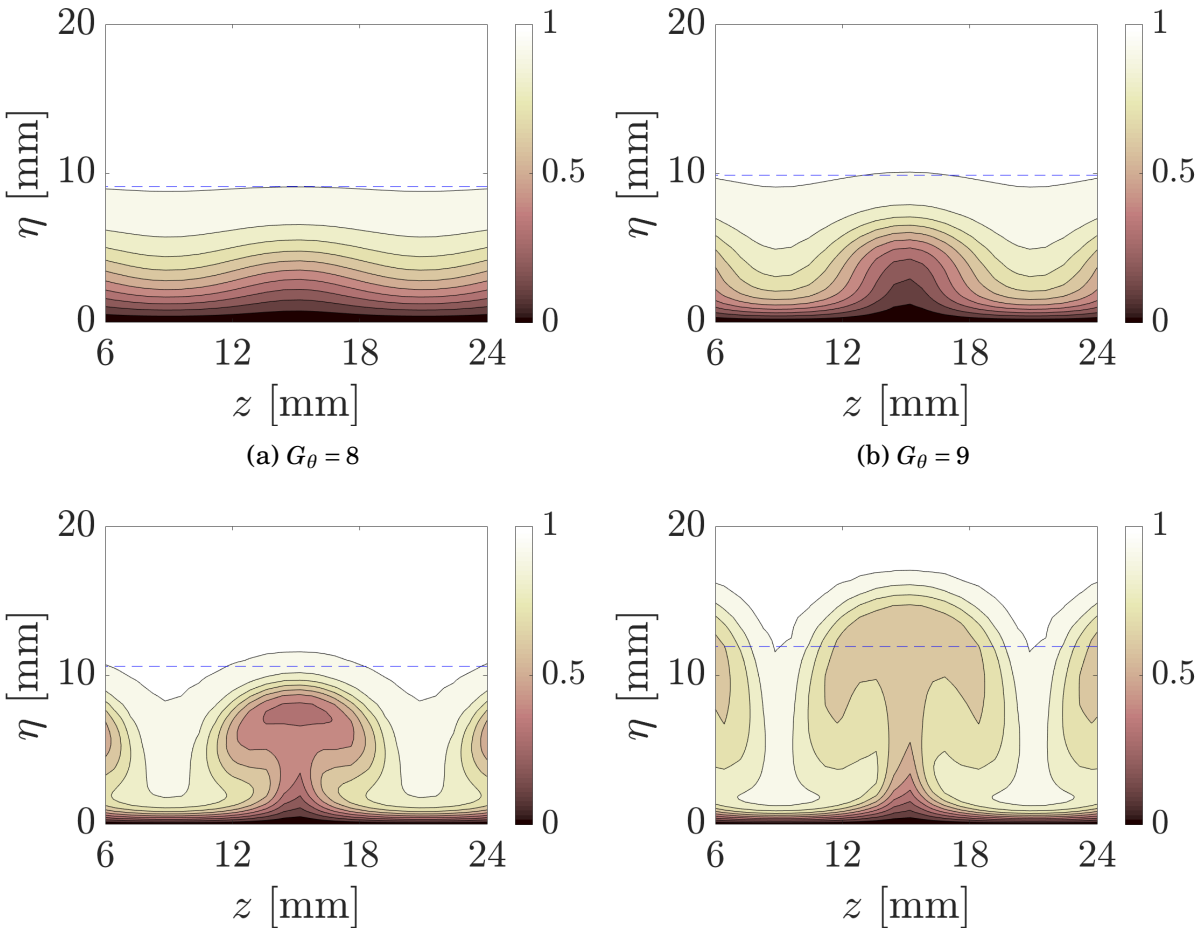

(a) $G_\theta = 8$ (b) $G_\theta = 9$

(c) $G_\theta = 10$ (d) $G_\theta = 12$

Figure 4.2: Streamwise development of θ_{th} for the case with $Pr = 1$. Contours for $\theta_{th} = 0.1$ to 0.9 with a step of 0.1. (- - -) Theoretical thermal boundary layer thickness of a fluid with $Pr = 1$, $\delta_{th,Pr=1}$.

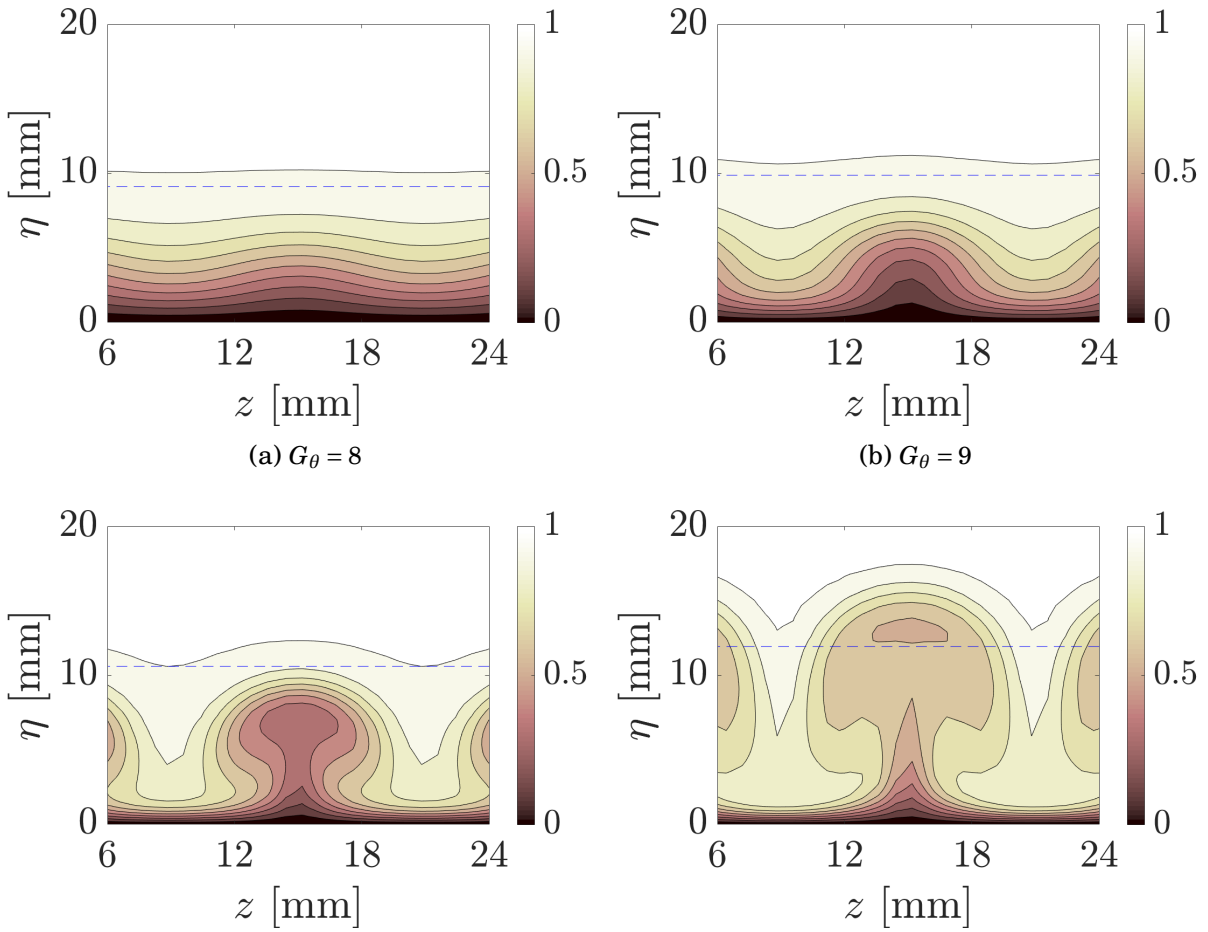

(a) $G_\theta = 8$ (b) $G_\theta = 9$

(c) $G_\theta = 10$ (d) $G_\theta = 12$

Figure 4.3: Streamwise development of θ_{th} for the case with $Pr = 0.72$. Contours for $\theta_{th} = 0.1$ to 0.9 with a step of 0.1. (- - -) Theoretical thermal boundary layer thickness of a fluid with $Pr = 1$, $\delta_{th,Pr=1}$.

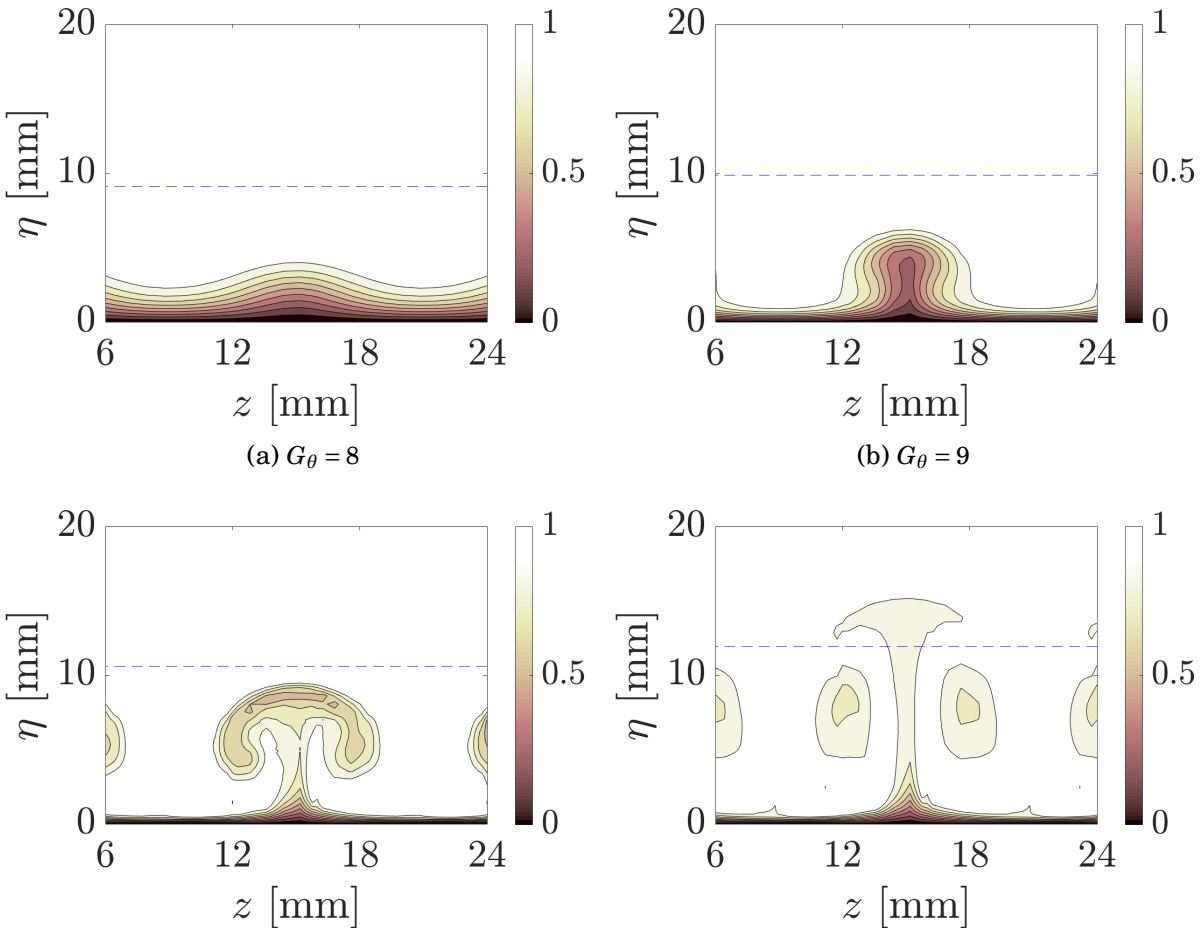

(a) $G_\theta = 8$ (b) $G_\theta = 9$

(c) $G_\theta = 10$ (d) $G_\theta = 12$

Figure 4.4: Streamwise development of θ_{th} for the case with $Pr = 7.07$. Contours for $\theta_{th} = 0.1$ to 0.9 with a step of 0.1. (- - -) Theoretical thermal boundary layer thickness of a fluid with $Pr = 1$, $\delta_{th,Pr=1}$.

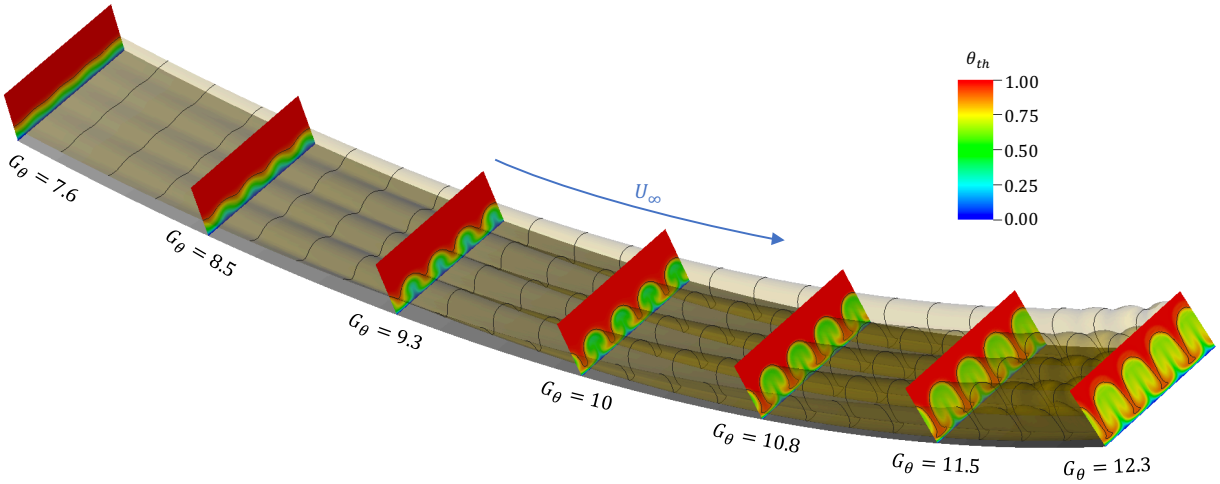

(a)

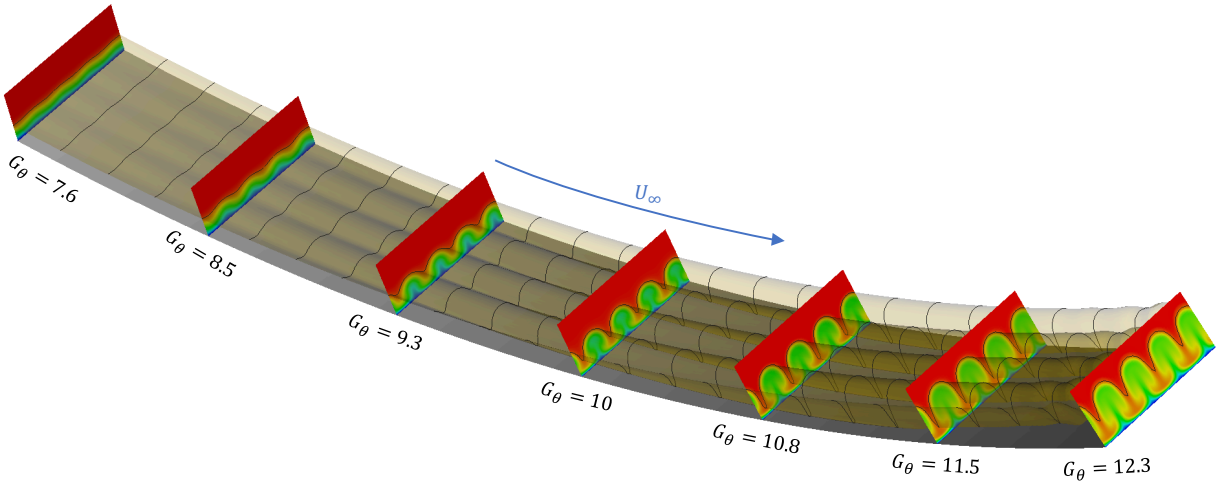

(b)

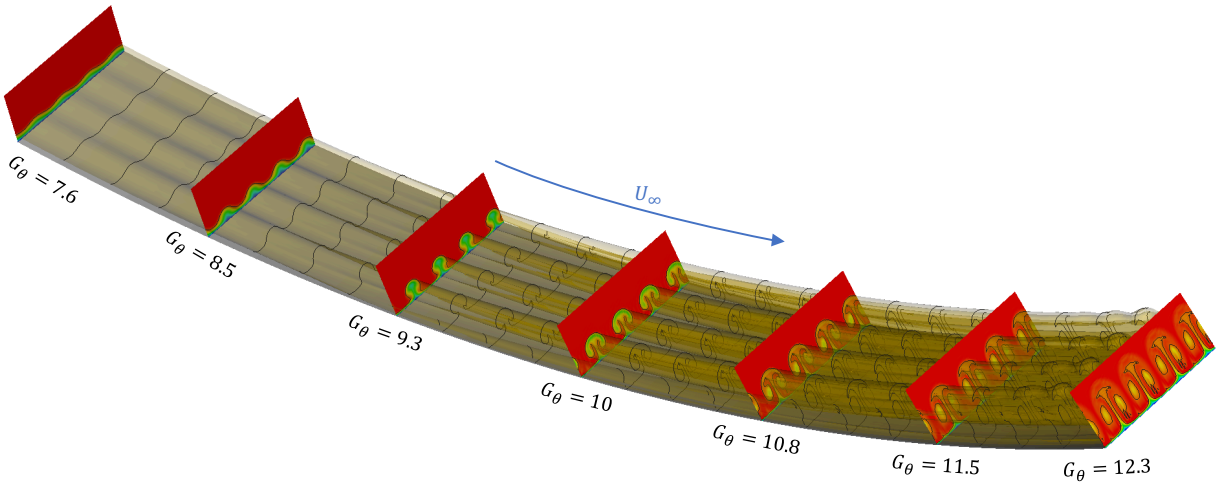

(c)

Figure 4.5: Streamwise evolution of the temperature field, θ_{th}, in the non-linear region showing the growth of the mushroom-like structure for the three Prandtl number cases. Contour plots at different streamwise positions are shown together with an iso-surface (in yellow) with value of $\theta_{th} = 0.9$. (a) $Pr = 1$. (b) $Pr = 0.72$. (c) $Pr = 7.07$.

the case with the smallest thermal diffusivity ($Pr = 7.07$), it is noticed that the inflectional S-shape thermal profile starts to appear before since at $G_\theta = 9$ it can be already noticed. Furthermore, the early appearance of the inflectional profile produces a more accentuated S-shape which can be appreciated at $G_\theta = 10$. It indicates that there is a low-temperature region ridding over a high-temperature one. Another difference in the upwash profile, is the higher boundary layer thickness for smaller Prandtl numbers which had been already mentioned. With respect to the downwash location, it is observed that, in all the cases, the thermal boundary layer is shortened due to the downward vortex movement which occurs in the same fashion as for the momentum boundary layer. The Prandtl number also affects the thermal boundary layer in the downwash location and a smaller thickness is observed for larger values of Pr.

4.4.2 Streamwise development of the thermal boundary layer thickness and Stanton number

As shown before, the original laminar flow (thermal and momentum boundary layers) is clearly modified during the laminar-to-turbulent transition process over a concave plate. The Görtler vortices modify the thermal boundary layer profile in such a way that it becomes thicker at the upwash and thinner at the downwash. In order to quantify this change in the boundary layer, the streamwise evolution of the thermal boundary layer thickness, δ_{th}, is plotted in Figure 4.7. The three different cases are plotted separately. For each case, a spanwise-averaged value of δ_{th} is shown along with the local values at the upwash and downwash locations. Additionally, the theoretical laminar value is plotted for comparison. As already shown in Figure 4.1, in the absence of any flow perturbation, this theoretical laminar solution is not affected by the surface curvature.

By comparing the three cases, it can be seen that δ_{th} becomes smaller as the Prandtl number is increased. As explained, this occurs due to the fact that the thermal diffusivity decreases as the Prandtl number increases. Despite this difference, a similar behavior can be observed, for the three cases, with respect to the streamwise evolution of δ_{th} at upwash and downwash locations. It is shown that, initially, the three cases perfectly follow the theoretical laminar solution at every spanwise location (upwash, downwash and spanwised-averaged curves collapse). However, as the flow enters into the non-linear region, a departure from the laminar solution is observed. Interesting is to notice that this departure initially occurs at upwash and downwash location, but the spanwise-averaged curve is able to follow the theoretical solution for a longer distance; which means that upwash and downwash effects are counteracted for a short length after the divergence point. The point where this divergence can be perceived occurs at $G_\theta \sim 7.5$ for the case with $Pr = 1$; and it occurs slightly downstream, $G_\theta \sim 7.8$, for the case with $Pr = 0.72$. However, for the case with $Pr = 7.07$, a clear earlier divergence can be noticed starting at $G_\theta \sim 5.9$. This early divergence comes along with a higher difference of δ_{th} at upwash and downwash locations in the non-linear region. At the downwash point where δ_{th} is the shortest, δ_{th} is 82% smaller compared

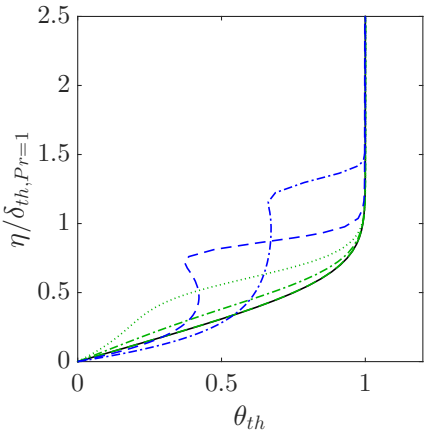

(a) Upwash. $Pr = 1$.

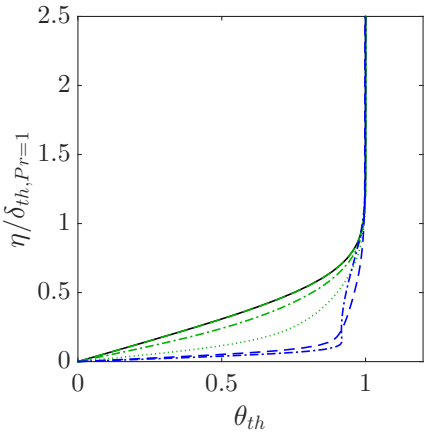

(b) Downwash. $Pr = 1$.

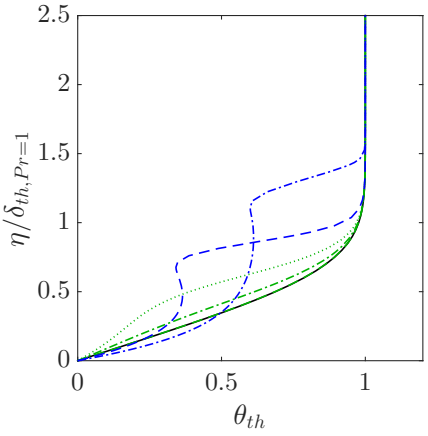

(c) Upwash. $Pr = 0.72$.

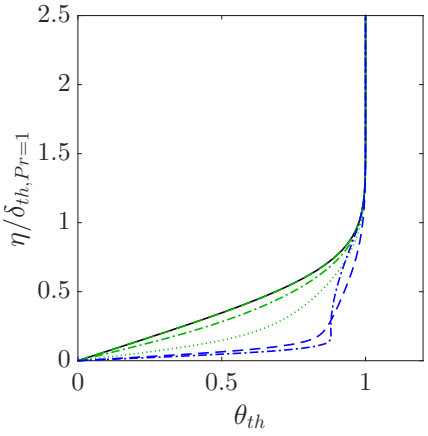

(d) Downwash. $Pr = 0.72$.

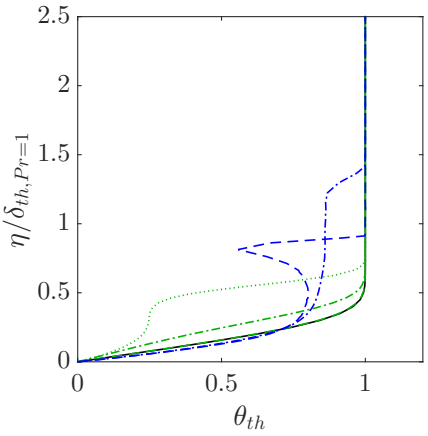

(e) Upwash. $Pr = 7.07$.

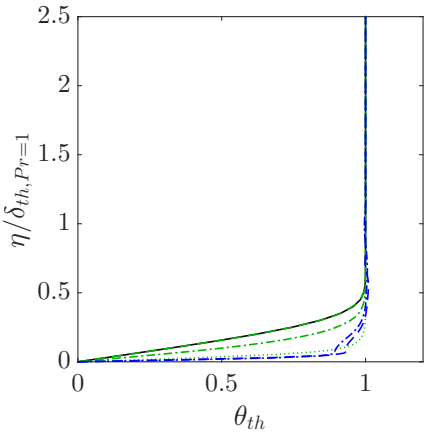

(f) Downwash. $Pr = 7.07$.

Figure 4.6: Streamwise evolution of the non-dimensional temperature profile, θ_{th}, at the upwash and downwash locations for the three cases ($Pr = 1$, $Pr = 0.72$ and $Pr = 7.07$). (——) Theoretical solution, (- - -) $G_\theta = 4$, (–·–) $G_\theta = 8$, (·····) $G_\theta = 9$, (- - -) $G_\theta = 10$ and (-·-·-) $G_\theta = 12$.

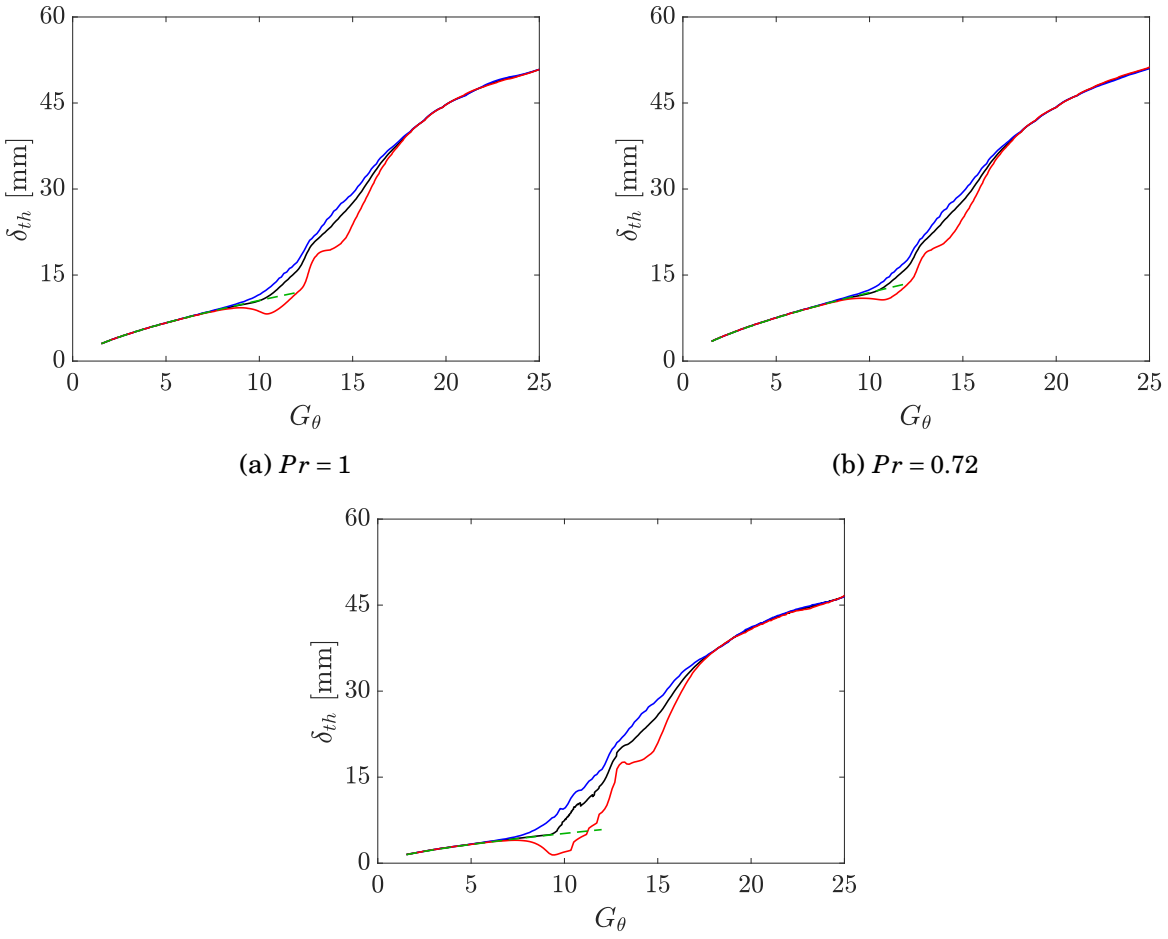

(a) $Pr = 1$

(b) $Pr = 0.72$

(c) $Pr = 7.07$

Figure 4.7: Streamwise development of the thermal boundary layer thickness, δ_{th}, for the three analyzed cases. (——) Spanwise average, (——) upwash, (——) downwash and (- - -) laminar theoretical solution.

to the upwash value. However, for the $Pr = 1$ case, at the downwash lowest δ_{th} point, δ_{th} is only 33% shorter compared to the upwash value at the same location.

Another interesting location to characterize is the convergence point where the δ_{th} value is the same again along the spanwise direction (upwash, downwash and spanwise-averaged curves collapse again). This point is related to the culmination of the transition process because it shows that the thermal field is homogeneous in the spanwise direction due to an intense turbulent mixing that does not allow to distinguish upwash and downwash locations anymore. For the three cases, this point occurs at $G_\theta \sim 18.2$; which means that the spanwise homogeneity of the turbulent thermal field occurs at the same streamwise location regardless of the Prandtl number. The same behavior of the momentum boundary layer (upwash and downwash locations as well as spanwise-average) has been observed numerically in the

Görtler vortices studies of Méndez et al. (2018) who computed the streamwise development of the boundary layer displacement and momentum thicknesses. Nonetheless, to the author's knowledge, there are no previous DNS studies showing the behavior of a transitional thermal boundary layer over a concave surface.

Another pertinent parameter for characterizing the boundary layer thermal behavior, and more specifically the surface heat transfer in forced convection flows, is the Stanton number, St. As expected, due to the spanwise variation of the thermal boundary layer thickness, St also varies with maximum and minimum values at downwash and upwash locations, respectively. Basically, in the upwash, the thermal boundary layer is elongated which relaxes the temperature gradient at the wall, and, subsequently, the convection heat transfer is decreased. On the other hand, the inverse effect occurs in the downwash, where the thermal boundary layer is compressed producing thereby an increase in the surface heat transfer. The streamwise development of the Stanton number, for the case with $Pr = 1$, is plotted in Figure 4.8. Local values, at upwash and downwash locations, as well as spanwise-averaged values are shown. A particularity of this case, is the fact that the analogy between the Stanton number and the skin-friction coefficient, C_f, can be verified. As it has been demonstrated before Liu & Sabry (1991), Liu (2008, 2007), the same behaviour is followed by these two quantities, C_f and St; and a relationship can be established: $St = C_f/2$. Hence, in order to verify this similarity, $C_f/2$ curves are also included in the chart. The first remark to point out is the fact that the surface heat transfer curves, indeed, match the ones of the wall-shear stresses. Only some negligible differences can be observed after the point where St is the highest and before the region where the spanwise homogeneity occurs. As explained by Méndez et al. (2018), this is the region where the secondary instabilities are broke-down by the increased turbulence mixing. Nonetheless, downstream, in the fully turbulence region, these negligible differences are no longer noticeable.

Regarding the surface heat transfer behavior in the laminar-to-turbulence transition process, which is also shown in Figure 4.8, it can be seen that, initially, the St is the same along the spanwise direction when the flow is laminar. As seen, in this laminar region, the surface heat transfer is also rather low. As the flow evolves, the primary instabilities produce the divergence of the surface heat transfer in such a way that it is enhanced in the downwash location but diminished in the upwash. Nevertheless, the spanwise-averaged curve follows the theoretical laminar solution for a longer distance until it reaches a minimum value at $G_\theta = 7.8$. Later on, the flow enters into the non-linear region, which is also characterized by the growth of the mushroom-like structures (Figure 4.2) and by the primary instability saturation (Figure 2.14), and a sudden increase of the spanwise-averaged Stanton number is observed. This sudden heat transfer enhancement occurs due to the downward movement of the vortices that compress the thermal boundary layer at the downwash location which causes an increase of the temperature gradient ($\partial T/\partial \eta$) at the next-to-the-wall region. Besides, the decrease of this temperature gradient at the upwash region is not that high that it is not able to counteract the downward movement effect and an overall enhancement of the

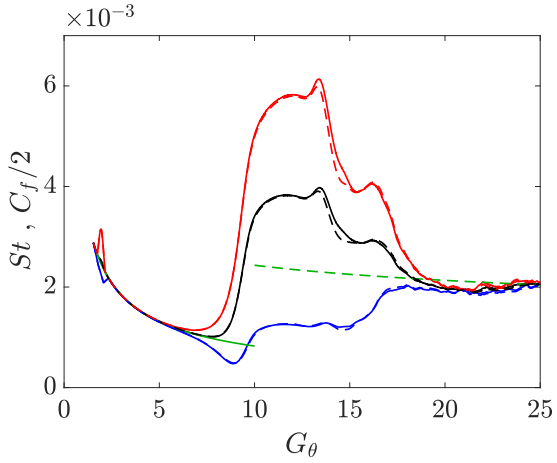

Figure 4.8: Streamwise development of the Stanton number, St, for the case with $Pr = 1$. The streamwise evolution of the skin-friction coefficient, C_f, is also included in the graph. Curves for St: (——) Spanwise average, (——) upwash, (——) downwash, (——) laminar theoretical solution and (- - -) turbulent theoretical solution. Curves for $C_f/2$: (- - -) Spanwise average, (- - -) upwash and (- - -) downwash. To notice is that theoretical solutions are valid for St as well as for $C_f/2$.

heat transfer occurs. Crane & Sabzvari (1989) related this heat transfer enhancement to the fact that the downwash region occupies a greater part of the span in the nonlinear phase. As seen from the temperature contours graphs (Figure 4.2), the downwash indeed occupies a greater section of the span whereas the mushroom-like structure occupies a smaller region. This nonlinear region of the transition process culminates with a local maximum value on the spanwise-averaged curve occurring at $G_\theta = 11.8$. After this point, the flow reaches the transition region (Méndez et al. 2018), which is characterized by the development of secondary instabilities and also by their breakdown into turbulence. As seen, in this region, upwash and downwash curves have a converging behavior which ends at $G_\theta = 21.8$, where upwash, downwash and spanwise-averaged collapse. After this point, the flow is spanwise homogeneous and it is considered that it has entered into the fully turbulent region.

It can be seen that, with the sudden increase of the Stanton number, the spanwised-averaged surface heat transfer is increased by a factor of 3.8 (compared to the minimum laminar value). Furthermore, it is interesting to point out that theoretical turbulent values of the Stanton number are clearly surpassed by the spanwise average curve by up to 70% during the transition process. This behavior was also observed by Malatesta et al. (2013, 2015) who concluded that that the primary instability increases the spanwise average heat transfer to values above the turbulent ones. Besides, similar to the present results, the heat transfer high rates were kept only in a short region before they decayed to the turbulent values downstream; which occurred due to the development of secondary instabilities. Furthermore, Liu (2008, 2007) studied theoretically the overshoot of the Stanton number concluding that the nonlinear steady Görtler flow can nearly bridge the laminar St values with

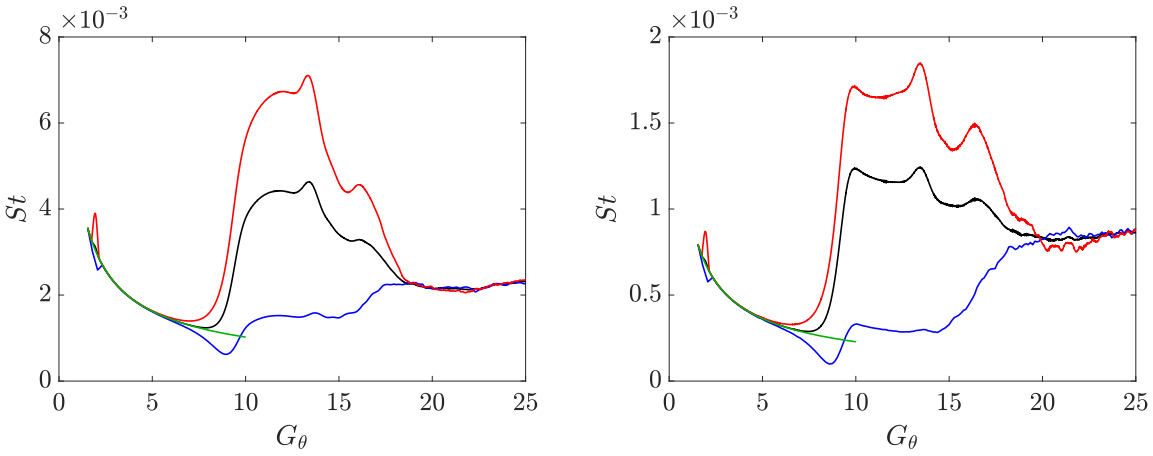

(a) $Pr = 0.72$ (b) $Pr = 7.07$

Figure 4.9: Streamwise development of the Stanton number, St, for the cases with $Pr = 0.72$ and $Pr = 7.07$. (——) Spanwise average, (——) upwash, (——) downwash and (- - -) laminar theoretical solution.

the higher turbulent ones. However, the overshoot beyond the turbulent St values occurs due to an intensified heat transfer coming from the eddy heat flux effect of the secondary instabilities.

The local, at upwash and downwash, and spanwise-averaged evolution of the Stanton number is also plotted for the other two cases in Figure 4.9. As expected, a similar behavior occurs locally as well as for the spanwise-average. The main difference being the value of the Stanton number which is higher for the fluids with lower Prandtl numbers. This occurs due to a better thermal conductivity, k_{th}, of the fluid, which enhances the convection heat transfer. Furthermore, the sudden increase of the spanwise-averaged Stanton number can be quantified for each case: for the $Pr = 0.72$ case, the heat transfer is enhanced by a factor of 3.9, whereas for the $Pr = 7.07$ the enhancement has a factor of 4.4. Similar values of heat transfer rates enhancement were found by Liu & Lee (1995) who found a 400% increase for the $Pr = 7.07$ and 340% for the $Pr = 0.72$ case.

Finally, it is also important to mention that, for the three Pr cases, the point at which the transition process starts (critical Görtler number) and the point where it ends completely depends on the receptivity. For this problem, wall-roughness elements are utilized to excite the transition process; however, it has been demonstrated, by Méndez et al. (2018), that many parameters could affect these locations. Hence, the location where the thermal boundary layer deviates from its laminar solution depends on the wall-roughness elements height, their streamwise location as well as their shape. Other parameters that can modify the transition process are the surface radius of curvature and the spanwise-wavelength of the vortices, which can be preset by the wall-roughness elements. The effect that such parameters have on the surface heat transfer are out of the scope of this study; however, some

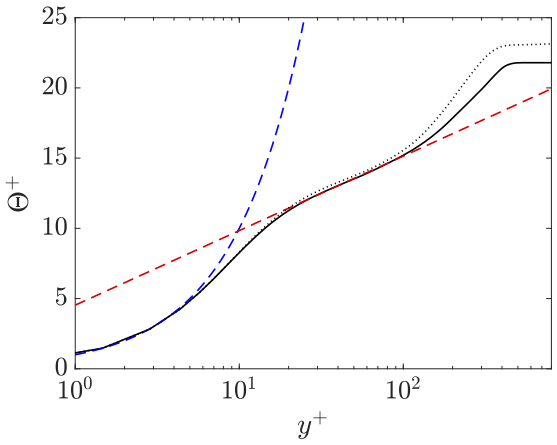

Figure 4.10: Temperature profile in the turbulent regime in viscous units, Θ^+ vs. y^+, at $Re_\theta = 1006$; for the case $Pr = 1$. (——) Temperature in wall-units, (·····) velocity in wall units U^+ from Méndez et al. (2018), (- - -) $\Theta^+ = y^+$, (- - -) $\Theta^+ = \kappa^{-1}\log y^+ + B$; where $\kappa = 0.43$ and $B = 4.5$.

effects can be inferred from the parametric studies of Méndez et al. (2018), where the evolution of the skin friction coefficient, which is analogous to the Stanton number, was studied by varying these parameters. It is, for instance, expected that a higher curvature (smaller radius) will increase the heat transfer rate in the non-linear region because a higher St peak is expected. Also, that the transition process will start earlier, and the surface heat transfer enhancement that comes with it as well, when the Görtler vortices wavelength is in the range of maximum growth ($\Lambda = 200 - 270$).

4.5 Thermal boundary layer in fully turbulent regime

In this section, the thermal boundary layer in the fully turbulent regime is analyzed. According to the author's knowledge, this is the first time that a Direct Numerical Simulation of a turbulent thermal boundary layer over a concave plate is reported in the literature. Results for three different Prandtl numbers are presented: $Pr = 1$, $Pr = 0.72$ and $Pr = 7.07$. Besides, for this turbulence analysis, the instantaneous temperature field, $\theta_{th} = \overline{\theta_{th}} + \theta'_{th}$, is decomposed in a mean (time-averaged) component, indicated by the overline, $\overline{\theta_{th}}$, and its respective temporal fluctuation, indicated by the prime symbol, θ'_{th}.

As mentioned, according to the transition analysis based on the Stanton number development, the flow reaches the fully turbulent regime after the streamwise position $G_\theta = 21.8$, where a spanwise homogeneity is observed. In order to characterize the thermal boundary layer in the turbulent regime, the spanwise-averaged temperature profile is plotted in Figure 4.10 and Figure 4.11 in viscous units at $G_\theta = 23.8$, which corresponds to $Re_\theta = 1006$. The temperature in wall units is defined as $\Theta^+ = (\langle\overline{T}\rangle - T_w)/\theta_\tau$, where θ_τ is the friction temperature (noticing that the brackets $\langle\rangle$ represent a spanwise-averaged quantity). The friction

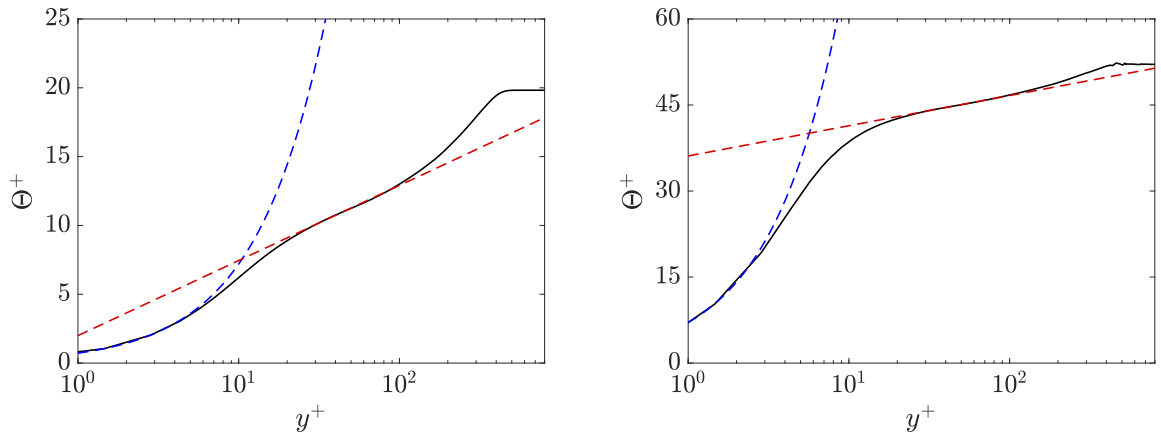

(a) $Pr = 0.72$ (b) $Pr = 7.07$

Figure 4.11: Turbulent temperature profile for the cases $Pr = 0.72$ and $Pr = 7.07$, at $Re_\theta = 1006$. (——) Temperature in wall-units, (- - -) $\Theta^+ = Pry^+$, (- - -) $\Theta^+ = \kappa^{-1}\log y^+ + B$. The log-law constants for the case with $Pr = 0.72$ are $\kappa = 0.42$ and $B = 1.99$; whereas, for the case with $Pr = 7.07$ they are $\kappa = 0.44$ and $B = 36.12$.

temperature, which is analogous to the friction velocity, u_τ, is defined as $\theta_\tau = Q_w/\rho c_p u_\tau$.

Figure 4.10 shows the turbulent temperature profile in wall units for the case with $Pr = 1$. It can be seen, that similar to the velocity profile, different regions, that are in accordance with the universal law of the wall, can be distinguished. First, the viscous sublayer, which is the region located next to the wall, can be observed which follows the law $\Theta^+ = y^+$. This region covers the range $y^+ \leq 5$. Next, the buffer region is followed, which is a transition region between the viscosity-dominated flow and the turbulence-dominated flow. This region covers the range $5 < y^+ \leq 30$. Finally, we can observed the log-law region which corresponds to the range $30 < y^+ \leq 100$. It follows the law $\Theta^+ = \kappa^{-1}\log y^+ + B$ with constants $\kappa = 0.43$ and $B = 4.5$. Since the analogy between the streamwise-momentum and the heat is expected to hold in the turbulent boundary layer, the velocity profile in wall units, U^+, from the studies of Méndez et al. (2018) is also plotted for comparison. This velocity profile of a boundary layer developing on a concave surface was also obtained in the fully turbulent region at the position $Re_\theta = 1006$. As seen, temperature and velocity profiles collapse and they have the same previously mentioned law-of-the-wall regions.

The temperature profiles in the fully turbulent regime for the cases with $Pr = 0.72$ and $Pr = 7.07$ are shown in Figure 4.11a and Figure 4.11b, respectively. The three law-of-the-wall regions are also observed. It is seen that the viscous sublayer region follows the law $\Theta^+ = Pry^+$ for both cases. Regarding the log-law region, the law $\Theta^+ = \kappa^{-1}\log y^+ + B$ is also followed. However, the log-law constants are different for each case. For the case with $Pr = 0.72$, they are $\kappa = 0.42$ and $B = 1.99$; whereas, for the case with $Pr = 7.07$ they are $\kappa = 0.44$ and $B = 36.12$.

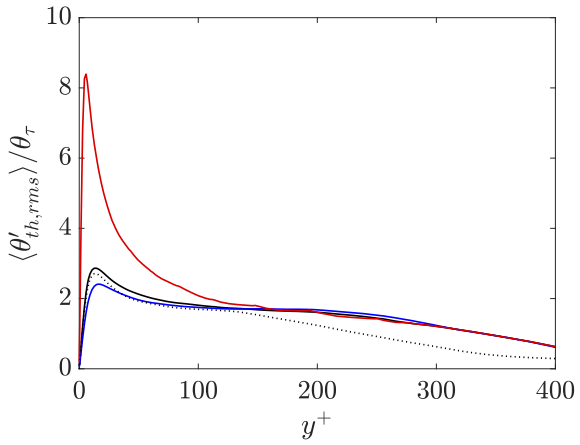

Figure 4.12: Second order temperature statistics, $\langle\theta'_{th,rms}\rangle/\theta_\tau$, as a function of y^+ for the different Prandtl number cases. (——) $Pr = 1$, (——) $Pr = 0.72$, (——) $Pr = 7.07$ and (·····) $\langle u'_{rms}\rangle/u_\tau$ from Méndez et al. (2018).

Finally, in order to characterize the second order temperature statistics, the wall-normal profiles of the rms (root-mean squared) temperature fluctuations, $\theta'_{th,rms}$, are plotted in Figure 4.12 for the different Prandtl number cases at the location $Re_\theta = 1006$. The rms velocity fluctuation u'_{rms}, from Méndez et al. (2018), are also plotted for comparing with the $Pr = 1$ case. As seen, the Reynolds analogy holds between temperature and velocity fluctuations in the near-to-the-wall region but in the outer layer ($y^+ > 100$) a departure is noticed with higher values for $\theta'_{th,rms}$. Besides, a higher peak can be observed for $Pr = 1$. It is located at $y^+ = 14.3$ and it has the value of 2.86. A higher peak for the rms temperature fluctuations, compared to the one of the streamwise velocity, was also observed in the DNS studies of Wu & Moin (2010) who simulated an incompressible turbulent boundary layer over a flat plate. With respect to the other cases, a lower peak occurs for the $Pr = 0.72$ case with value of 2.41; whereas, for the $Pr = 7.07$, a higher peak occurs with a value of 8.39. The differences are partially related to the variation of the friction temperature which increases as the Prandtl number decreases. It is also interesting to point out that the three cases tend to collapse in the outer layer, $y^+ > 100$.

Chapter 5
Conclusions and perspectives

5.1 Conclusion

This research work was performed with the objective of characterizing and analyzing the laminar-to-turbulence transition of a boundary layer transition passing over a concave surface. The outcome of this work is expected to be utilized for many engineering applications where this type of geometry can be found. With respect to the renewable energy field, it was described in Chapter 1 that a concave surface can be found in the Savonius-style VAWT blades. Therefore, the obtained results are certainly relevant for their design and development. Furthermore, in the aerospace sector, as explained, the studied transition scenario has also an impact on the performance of several components where it has been observed, such as aircraft wings, turbomachinery blades and nozzles. It is thus also expected that the outcome of this PhD thesis can be used for a better design and performance improvement of these engineering components.

From the literature review, which was performed in Chapter 1, it can be concluded that the flow physics of a boundary layer over a concave surface is quite different from that of a boundary layer developing over a flat plate, that has been largely investigated. The main difference coming from the fact that the flow passing over a concave surface is naturally unstable to the developed wall-normal pressure gradient, which is absent in a flat-plate flow. Therefore, any perturbation introduced to the boundary layer capable of producing a radial particle displacement (e.g. wall-roughness or free-stream turbulence intensity), will trigger the transition phenomenon which starts with the development of the Görtler vortices. This leads to conclude that the behavior of a boundary layer over a a concave geometry is quite unique and therefore an extensive analysis and characterization is needed by means of high-fidelity tools such as DNS.

Moreover, also during the literature review, it was explained that the concept of a unique critical number, so familiar in hydrodynamic-stability theory, is not suitable in the Görtler flow, except for asymptotically small wavelengths. This is because the position of the neutral stability curve depends on the boundary layer receptivity, i.e., the location and character of the initial disturbances (Hall 1982, 1983). Therefore, it was concluded that the most appropriate approach for solving the Görtler instability analysis is the numerical integration of the governing hydrodynamic equations, rather than using linear stability theory. This numerical integration can be done by solving the Navier-Stokes equations by means of DNS.

In Chapter 2, the utilized numerical method, i.e. the spectral element method, was extensively described. It was seen that the SEM is an advantageous numerical method because it can benefit from the geometrical flexibility of the FEM as well as from the high accuracy

and exponential convergence of the spectral methods. It was also shown that NEK5000, the utilized DNS solver, has been largely validated for transitional and fully-turbulent flow on the canonical flow cases (i.e. flat plate, channel and pipe flows) by several authors that compared the solver results with previous experimental and numerical data. This leads to conclude that the solver, NEK5000, is perfectly capable of computing accurately the laminar-to-turbulent transition phenomenon. Moreover, a validation and a mesh convergence study was performed in order to verify whether the utilized simulation set-up (i.e. computational domain, boundary conditions, grid refinement and perturbation method) is capable of computing correctly the flow over a concave surface. For that, the computed results were compared with the theoretical Blasius solution and with the DNS reference data of Schrader et al. (2011). It was shown that the base flow (laminar flow without perturbation) and the perturbed flow (boundary layer response to wall-roughness) match the laminar theoretical solution and the DNS reference data, respectively, for three polynomial orders that were used ($N = 5$, 7 and 9). This led to conclude that the utilized numerical set-up can be used for the boundary layer transition analysis.

In Chapter 3, a spatially evolving boundary layer over a concave plate with $R = 1$ m was investigated by means of Direct Numerical Simulations. Four wall-roughness elements, equally distributed in the spanwise direction, were used to trigger the transition of the flow. Their wavelength, $\Lambda = 250$, was chosen such as it matches previous numerical and experimental studies (Tandiono et al. 2008, Schrader et al. 2011, Tandiono et al. 2013). As shown by linear stability analysis, the selected dimensionless parameter produced the most amplified Görtler vortices (Floryan 1991, Smith 1955, Meksyn 1950). Moreover, the utilized excitation method allowed to preset the wavelength of the Görtler vortices that emerged as primary instabilities in the laminar-to-turbulent transition process. Unlike the free-stream turbulence imposed at the inlet, where Görtler vortices of several wavelengths develop and merge among each other during the transition process (Ducoin et al. 2017, Schrader et al. 2011), the wall-roughness elements allowed to obtain a clear spanwise characterization of the streamwise streaks development and their breakdown into turbulence.

A wavy flow field in the spanwise direction was characterized, where the upwash and downwash regions have been clearly identified. The growth of a mushroom-like structure, typical of the Görtler flow, was observed in the upwash region. This structure appears and grows in the nonlinear region of the transition process; once the primary stability has saturated. The analysis of V and W velocity contours helped to extend the characterization of the Görtler vortices. These quantities, being one order of magnitude lower than the streamwise velocity component, are usually not captured or measured in the experimental studies (only W has been reported (Tandiono et al. 2013)).

As it had been reported experimentally (Swearingen & Blackwelder 1987), the development of the secondary instabilities can be correlated with high shear regions dU/dz and $dU/d\eta$. High dU/dz regions trigger the sinuous mode, while high $dU/d\eta$ regions trigger the varicose mode. For the baseline case with $\Lambda = 250$, only the varicose mode could be excited. It

was observed that the high dU/dz regions correlate quite well with high regions of Tu; which at same time correlate with one of the inflection points of the $U(\eta)$ profile (the one closer to the boundary layer edge). In order to observe the primary and secondary instabilities, the vortical coherent structures have been extracted using the λ_2 criterion. They highlight the Görtler vortices as well as the horseshoe vortices.

It was shown that the primary instability can be associated with spatial disturbances in the spanwise direction, while the secondary instability can be related to temporal fluctuations. The secondary instability grows faster than the primary one with a ratio of 3.7 to 1.

The streamwise development of the boundary layer during the transition process was also quantified through the measurement of the main parameters of the boundary layer, such as δ^*, θ and C_f. Local measurements at the upwash and downwash locations using DNS computations were reported for the first time. Moreover, a spanwise average of those quantities was also included. The different regions of the transition process could be clearly identified. In the linear region, the Blasius theoretical solution is followed very well until the presence of the Görtler vortices starts to affect the base flow. Basically, δ^* and θ decrease at the downwash region and increase at the upwash region. Regarding C_f, the inverse behavior was noticed. The nonlinear region could be identified with the departure from the Blasius solution and with the sudden increase of C_f, which reaches higher values compared to the turbulent ones (by up to 70%). The transition region is characterized by the development of secondary instabilities that eventually break down into turbulence. Finally, the increased mixing generates a flow field where upwash and downwash regions are no longer noticed and a spanwise homogeneous turbulent flow is reached.

Some parametric studies were also presented in order to analyze the effect of the surface radius, R, the wall-roughness elements height, h, the wall-roughness elements streamwise location, Re_{ξ}^{rgh}, the spanwise wavelength, Λ, and the wall-roughness geometry, on the critical Görtler number, $G_{\theta_{cr}}$. It was shown that a higher radius of curvature, R, delays the transition starting point. However, when the streamwise direction is non-dimensionalized, it occurred at a very similar $G_{\theta_{cr}}$ ($G_{\theta_{cr}} \cong 7.75$, for the baseline case with $h = 0.01\delta^*$). The wall-roughness elements height, h, was also varied and it was found that when it increases, the transition starting point occurs earlier, following a power law of $G_{\theta_{cr}} \propto (h/\delta^*)^{-0.1095}$. Furthermore, a linear relation between the critical Görtler number and the Reynolds number based on the wall-roughness streamwise location was found. This relation suggests that, for the baseline case with $h = 0.01\delta^*$, transition will not start before $G_{\theta_{cr}} \cong 7$ (for the limiting case when $Re_{\xi}^{rgh} \to 0$). Besides, the variation of the Görtler vortices wavelength showed that transition starts earlier when Λ is within the range $\Lambda = 162$ to 250. Moreover, it was shown that, with a bump geometry, a power law between $G_{\theta_{cr}}$ and h is also followed. It is observed that the variation of $G_{\theta_{cr}}$ with h has the same order of magnitude for all the utilized wall-roughness geometries. However, compared with the baseline bump-dimple geometry, transition is delayed when using a bump geometry.

In Chapter 4, the spatial evolution of a thermal boundary layer during the laminar-to-turbulent transition process over a concave plate was investigated. Three different Prandtl numbers were utilized: (i) $Pr = 1$, in order to verify the Reynolds analogy between heat and streamwise-velocity, (ii) $Pr = 0.72$, which corresponds to air at standard conditions, and (iii) $Pr = 7.07$, which corresponds to water at standard conditions. Furthermore, the temperature variable was treated as a passive scalar, which means that it has no dynamical effect on the fluid motion. This approach allows to create an analogy between the obtained thermal results and the flow species transport through the Schmidt and Prandtl numbers.

During the validation study, it was verified that the disturbance-free laminar flow over a concave plate is able to follow perfectly the theoretical laminar solution of a flat plate thermal boundary layer for the three Pr cases. For that, temperature wall-normal distribution, thermal boundary layer thickness evolution and surface heat transfer evolution were computed and compared. It could then be concluded that the centrifugal effects does not affect the laminar thermal boundary layer. This test case also allowed to find that, similar to the flat plate, the theoretical thermal boundary layer over a concave wall behave as $\delta_{th} = \delta Pr^{-1/3}$ in laminar conditions.

Similar to the momentum problem, it was observed that mushroom-like structures of low-temperature develop in the non-linear region of the transition process. For the $Pr = 1$ case, a perfect match between the computed temperature distribution and the streamwise velocity contours was obtained; which allowed to corroborate the analogy between heat and streamwise momentum. Furthermore, the $Pr = 0.72$ case produced a very similar development of the temperature distribution. However, slightly more diffused mushroom-like structures were produced. With respect to the $Pr = 7.07$ case, thermal thin structures with two low-temperature regions hanging from the mushroom head at each extremity were observed (called palm tree-like structures). Same observations for the $Pr = 0.72$ and $Pr = 7.07$ cases were reported by Lee & Liu (1992) whose results were obtained through marching-solution computations. Furthermore, similar to the momentum boundary layer, temperature profiles plotted at the upwash region presented elongated forms which evolved into S-shape profiles.

The thermal development during the laminar-to-turbulent transition process was characterized by quantifying the evolution of δ_{th} and St. This allowed to identify the different transition regions. For the three cases, in the linear region, the laminar theoretical solution is perfectly followed until the Görtler vortices effect starts to be noticed. They produce an increase of St in the downwash and a decrease in the upwash. This means that the surface heat transfer is enhanced due to to the downward vortex movement that compresses the thermal boundary layer (which produces higher temperature gradients $\partial T/\partial \eta$). This departure from the theoretical solution is followed by the non-linear region where a sudden increase of the spanwise-averaged St occurs. Transition can thus increase the spanwise-averaged heat transfer by a factor of 3.9 for the case of $Pr = 1$, of 3.8 for $Pr = 0.72$ and of 4.4 for $Pr = 7.07$ (to note that the computed heat transfer rates enhancement factors agree with the ones observed by Liu & Lee (1995)). Downstream, secondary instabilities develop in the

transition region which increase the flow mixing. This results in a homogeneous flow where St tends to a same value at upwash and downwash locations. When this convergence point is reached, the flows enters into the fully turbulent region where a decrease of St occurs (but still higher that laminar values).

Another important result from this study is the corroboration of the Reynolds analogy between the heat and the momentum problem for the case with $Pr = 1$. When the computed non-dimensional temperature field, θ_{th}, is compared with the non-dimensional streamwise velocity field, U/U_∞, no differences could be noticed (as it was shown in the temperature contours and profiles that were plotted). This analogy was reflected when the streamwise development of the Stanton number was compared with the one of the skin-friction coefficient. A perfect match of the analogy $St = C_f/2$ was found throughout the complete laminar-to-turbulence transition process.

Finally, the thermal boundary layer in fully turbulent regime over a concave surface was characterized by the first time by means of DNS. It was concluded that in the viscous sublayer the law $\Theta^+ = Pry^+$ is followed for the three Pr cases. With respect to the log-law region, a match for the temperature profile with $Pr = 1$ and the momentum boundary layer profile occurs. Also, the log-law constant B increases as Pr increases. Finally, the rms temperature fluctuations, $\theta'_{th,rms}$ were computed finding that they have a higher peak as Pr increases; however, the three Pr cases collapse in the outer layer.

5.2 Perspectives

The characterization and analysis presented in this PhD thesis undoubtedly enhanced our knowledge on the laminar-to-turbulent transition phenomenon over a concave surface. Moreover, the implication of the physical and geometrical parameters, that play a role on the triggering of the transitional phenomenon as well as on the behavior and the topology of the flow, was extensively investigated.

Nevertheless, there are still many open questions and relevant investigations that should be addressed on the topic. Therefore, the future works in continuation of the present research study could focus on the following points:

- The characterization of the turbulent boundary layer over a concave surface can be looked deeper in details. The centrifugal effects on the turbulence structure (log-law constants, Reynolds stresses, TKE budget, etc.) and higher order statistics can be studied by means of DNS. Moreover, parametric studies of the turbulence structure change as a function of R and G_θ should be included.
- The surface heat transfer phenomenon can be studied with more complete DNS models where the temperature is treated as an active scalar. That way, unlike to the presented passive scalar analysis, the temperature would be able to modify the flow physical properties such as density and viscosity according to its local concentration. Such approach would allow to study the wall heating/cooling effect on the transition process,

as it has been shown theoretically, through LST, that the Görtler vortices growth can be accelerated or slowed down (Garg & DiPrima 1984).

- The effects of wall heating on the turbulence structure of a fully turbulent boundary layer developing on a concave plate have also not been studied numerically. An active scalar approach could also be used for such investigation. Lee et al. (2013) performed a DNS study on a turbulent boundary layer passing over a heated flat plate. They found that a significant reduction of the skin friction coefficient can be achieved by heating the plate. Regarding the turbulence structure, on the heated plate case the log-law region of the mean streamwise velocity was shifted upward whereas the turbulence intensity and the Reynolds shear stresses were decreased. The TKE budget terms (production and dissipation) were also affected. It is thus propose to study if similar effects can occur on a fully turbulent boundary layer developing over a heated concave surface.
- As mentioned during the literature review, very little attention has been given to the development of Görtler vortices over convex geometries. Wall-jet profiles are naturally unstable and prone to trigger this type of centrifugal instabilities over convex surfaces, as it has been shown through LST (Floryan 1986) and also observed experimentally (Matsson 1998). Therefore, an extensive characterization and analysis can be done due to the great number of engineering devices where this type of geometry can be found.
- Regarding the engineering applications, DNS can be performed using geometries and conditions that reassemble more to the engineering components and to their physical environment. For the Savonius-style VAWT, simulations including the rotational effect are suggested by using a rotating frame of reference that takes into account the additional rotating speed.

Bibliography

Aihara, Y., Tomita, Y. & Ito, A. (1985), Generation, development and distortion of longitudinal vortices in boundary layers along concave and flat plates, *in* 'Laminar-Turbulent Transition', Springer, pp. 447–454. (Cited on pages xii, 28 & 30).

Arolla, S. K. & Durbin, P. A. (2015), 'LES of spatially developing turbulent boundary layer over a concave surface', *Journal of Turbulence* **16**(1), 81–99. (Cited on page 36).

Barlow, R. & Johnston, J. (1985), Roll-cell structure in a concave turbulent boundary layer, *in* '23rd Aerospace Sciences Meeting', p. 297. (Cited on page 35).

Barlow, R. S. & Johnston, J. P. (1988), 'Structure of a turbulent boundary layer on a concave surface', *Journal of Fluid Mechanics* **191**, 137–176. (Cited on pages xiii, 34, 35 & 36).

Bassom, A. P. & Hall, P. (1994), 'The receptivity problem for O(1) wavelength Görtler vortices', *Proceedings of the Royal Society of London. Series A: Mathematical and Physical Sciences* **446**(1928), 499–516. (Cited on page 23).

Bassom, A. P. & Seddougui, S. O. (1995), 'Receptivity mechanisms for Görtler vortex modes', *Theoretical and Computational Fluid Dynamics* **7**(5), 317–339. (Cited on page 23).

Beckwith, I. E. & Holley, B. B. (1981), 'Gortler vortices and transition in wall boundary layers of two Mach 5 nozzles'. (Cited on pages 2 & 15).

Belligoli, Z., Dwight, R., Kok, G. & Lucas, P. (2017), 'A Bayesian study of uncertainty in ultrasonic flow meters under non-ideal flow conditions', *Metrologia* **54**(4), 584. (Cited on pages xii & 17).

Benmalek, A. & Saric, W. S. (1994), 'Effects of curvature variations on the nonlinear evolution of Görtler vortices', *Physics of Fluids* **6**(10), 3353–3367. (Cited on pages xii, 26 & 27).

Bertolotti, F. & Kendall, J. (1997), Response of the Blasius boundary layer to controlled free-stream vortices of axial form, *in* '28th Fluid Dynamics Conference', p. 2018. (Cited on page 53).

Bippes, H. (1972), 'Experimental study of the laminar-turbulent transition of a concave wall in a parallel flow'. (Cited on pages xii, 20, 21, 28, 29 & 77).

Bippes, H. & Görtler, H. (1972), 'Dreidimensionale Störungen in der Grenzschicht an einer konkaven Wand', *Acta Mechanica* **14**(4), 251–267. (Cited on page 21).

Blasius, H. (1907), *Grenzschichten in Flüssigkeiten mit kleiner Reibung*, Druck von BG Teubner. (Cited on page 3).

Boiko, A., Ivanov, A., Kachanov, Y. S. & Mischenko, D. (2010), 'Steady and unsteady Görtler boundary-layer instability on concave wall', *European Journal of Mechanics-B/Fluids* **29**(2), 61–83. (Cited on page 32).

Bortolini, M., Gamberi, M., Graziani, A., Manzini, R. & Pilati, F. (2014), 'Performance and viability analysis of small wind turbines in the European Union', *Renewable Energy* **62**, 629–639. (Cited on page 1).

Bottaro, A. & Klingmann, B. G. B. (1996), 'On the linear breakdown of Gortler vortices', *European Journal of Mechanics, B/Fluids* **15**(3), 301–330. (Cited on page 29).

Bottaro, A. & Luchini, P. (1999), 'Görtler vortices: are they amenable to local eigenvalue analysis?', *European Journal of Mechanics-B/Fluids* **18**(1), 47–65. (Cited on page 21).

Bottaro, A. & Zebib, A. (1997), 'Görtler vortices promoted by wall roughness', *Fluid dynamics research* **19**(6), 343–362. (Cited on page 23).

Chen, F.-J., Malik, M. & Beckwith, I. (1985), Instabilities and transition in the wall boundary layers of low-disturbance supersonic nozzles, *in* '18th Fluid Dynamics and Plasmadynamics and Lasers Conference', p. 1573. (Cited on page 15).

Chen, F.-J., Malik, M. & Beckwith, I. (1990), Advanced Mach 3.5 axisymmetric quiet nozzle, *in* '21st Fluid Dynamics, Plasma Dynamics and Lasers Conference', p. 1592. (Cited on page 16).

Chen, F.-J., Malik, M. R. & Beckwith, I. E. (1992), 'Gortler instability and supersonic quiet nozzle design', *AIAA journal* **30**(8), 2093–2094. (Cited on page 16).

Chen, F.-J., Wilkinson, S. P. & Beckwith, I. E. (1993), 'Görtler instability and hypersonic quiet nozzle design', *Journal of Spacecraft and Rockets* **30**(2), 170–175. (Cited on pages 2 & 16).

Crane, R. & Sabzvari, J. (1989), 'Heat transfer visualization and measurement in unstable concave-wall laminar boundary layers', *Journal of Turbomachinery* **111**(1), 51–56. (Cited on pages 37 & 107).

Cui, J., Rao, V. N. & Tucker, P. (2016), 'Numerical investigation of contrasting flow physics in different zones of a high-lift low-pressure turbine blade', *Journal of Turbomachinery* **138**(1), 011003. (Cited on page 15).

Dagenhart, J. & Mangalam, S. (1986), Disturbance functions of the Görtler instability on an airfoil, *in* '4th Joint Fluid Mechanics, Plasma Dynamics and Lasers Conference', p. 1048. (Cited on page 2).

Day, H., Herbert, T. & Saric, W. (1990), 'Comparing local and marching analyses of Görtler instability', *AIAA journal* **28**(6), 1010–1015. (Cited on page 20).

Dean, W. (1928), 'Fluid motion in a curved channel', *Proceedings of the Royal Society of London. Series A, Containing Papers of a Mathematical and Physical Character* **121**(787), 402–420. (Cited on page 17).

Denier, J. P., Hall, P. & Seddougui, S. O. (1991), 'On the receptivity problem for Görtler vortices: vortex motions induced by wall roughness', *Philosophical Transactions of the Royal Society of London. Series A: Physical and Engineering Sciences* **335**(1636), 51–85. (Cited on page 23).

Deville, M. O., Fischer, P. F., Fischer, P. F., Mund, E. et al. (2002), *High-order methods for incompressible fluid flow*, Vol. 9, Cambridge university press. (Cited on page 50).

Duck, P., Ruban, A. & Zhikharev, C. (1996), 'The generation of Tollmien-Schlichting waves by free-stream turbulence', *Journal of Fluid Mechanics* **312**, 341–371. (Cited on page 11).

Ducoin, A., Roy, S. & Safdari Shadloo, M. (2016), Direct numerical simulation of nonlinear secondary instabilities on the pressure side of a savonius style wind turbine, *in* 'ASME 2016 Fluids Engineering Division Summer Meeting collocated with the ASME 2016 Heat Transfer Summer Conference and the ASME 2016 14th International Conference on Nanochannels, Microchannels, and Minichannels', American Society of Mechanical Engineers Digital Collection. (Cited on pages 2 & 14).

Ducoin, A., Shadloo, M. & Roy, S. (2017), 'Direct Numerical Simulation of flow instabilities over Savonius style wind turbine blades', *Renewable energy* **105**, 374–385. (Cited on pages xiii, 1, 2, 14, 32, 33, 55, 64 & 113).

El Khoury, G. K., Schlatter, P., Noorani, A., Fischer, P. F., Brethouwer, G. & Johansson, A. V. (2013), 'Direct numerical simulation of turbulent pipe flow at moderately high Reynolds numbers', *Flow, turbulence and combustion* **91**(3), 475–495. (Cited on pages xiii, 54 & 55).

Emmons, H. (1951), 'The laminar-turbulent transition in a boundary layer-Part I', *Journal of the Aeronautical Sciences* **18**(7), 490–498. (Cited on page 12).

Feng, H. & Mavriplis, C. (2002), 'Adaptive spectral element simulations of thin premixed flame sheet deformations', *Journal of scientific computing* **17**(1-4), 385–395. (Cited on page 43).

Finnis, M. & Brown, A. (1989), 'Stability of a laminar boundary layer flowing along a concave surface', *Journal of Turbomachinery* **111**(4), 376–386. (Cited on page 26).

Finnis, M. & Brown, A. (1997), 'The linear growth of Görtler vortices', *International Journal of Heat and Fluid Flow* **18**(4), 389–399. (Cited on pages xii, 26 & 27).

Fischer, P. & Choudhari, M. (2004), Numerical simulation of roughness-induced transient growth in a laminar boundary layer, *in* '34th AIAA Fluid Dynamics Conference and Exhibit', p. 2539. (Cited on pages xiii, 52 & 53).

Fischer, P., Kruse, J., Mullen, J., Tufo, H., Lottes, J. & Kerkemeier, S. (2008), 'Nek5000: Open source spectral element CFD solver', *Argonne National Laboratory, Mathematics and Computer Science Division, Argonne, IL, see https://nek5000.mcs.anl.gov/* . (Cited on pages 42, 44, 50 & 52).

Floryan, J. (1986), 'Görtler instability of boundary layers over concave and convex walls', *The Physics of fluids* **29**(8), 2380–2387. (Cited on pages 17, 18 & 117).

Floryan, J. (1991), 'On the Görtler instability of boundary layers', *Progress in Aerospace Sciences* **28**(3), 235–271. (Cited on pages 18, 20, 28, 34, 84 & 113).

Floryan, J. M. & Saric, W. S. (1982), 'Stability of Gortler vortices in boundary layers', *AIAA journal* **20**(3), 316–324. (Cited on pages xii, 19, 20, 61, 77 & 95).

Floryan, J. M. & Saric, W. S. (1984), 'Wavelength selection and growth of Görtler vortices', *AIAA journal* **22**(11), 1529–1538. (Cited on pages 19 & 23).

Garg, V. K. & DiPrima, R. (1984), 'The effect of heating on the stability of flow over concave walls', *The Physics of fluids* **27**(4), 812–820. (Cited on pages 36 & 117).

Giannetti, F. & Luchini, P. (2006), 'Leading-edge receptivity by adjoint methods', *Journal of Fluid Mechanics* **547**, 21–53. (Cited on page 53).

Girgis, I. & Liu, J. (2006), 'Nonlinear mechanics of wavy instability of steady longitudinal vortices and its effect on skin friction rise in boundary layer flow', *Physics of Fluids* **18**(2), 024102. (Cited on pages 31, 37 & 79).

Görtler, H. (1940), 'Uber eine dreidimensionale instabilität laminarer grenzschichten an konkaven wänden', *Nachr. Ges. Wiss. Göttingen, NF* **2**(1), 1–26. (Cited on pages 2, 17 & 18).

Gourdain, N., Gicquel, L. Y., Gomar, A., Fransen, R., Collado, E. & Arts, T. (2011), 'Application of RANS and LES to the prediction of complex flows in gas turbine components', *Proceedings of 46th Symposium of Applied Aerodynamics* . (Cited on page 15).

Grieser, B., Sunak, Y. & Madlener, R. (2015), 'Economics of small wind turbines in urban settings: An empirical investigation for Germany', *Renewable Energy* **78**, 334–350. (Cited on page 1).

Guo, Y. & Finlay, W. (1994), 'Wavenumber selection and irregularity of spatially developing nonlinear Dean and Görtler vortices', *Journal of Fluid Mechanics* **264**, 1–40. (Cited on page 23).

Guo, Y., Kleiser, L. & Adams, N. (1994), A comparison study of an improved temporal DNS and spatial DNS of compressible boundary layer transition, *in* 'Fluid Dynamics Conference', p. 2371. (Cited on page 31).

Hall, P. (1982), 'Taylor-Gortler vortices in fully developed or boundary-layer flows: linear theory', *Journal of Fluid Mechanics* **124**, 475–494. (Cited on pages 20, 36 & 112).

Hall, P. (1983), 'The linear development of Görtler vortices in growing boundary layers', *Journal of Fluid Mechanics* **130**, 41–58. (Cited on pages 20, 21, 22 & 112).

Hall, P. (1988), 'The nonlinear development of Görtler vortices in growing boundary layers', *Journal of Fluid Mechanics* **193**, 243–266. (Cited on page 26).

Hall, P. (1990), 'Görtler vortices in growing boundary layers: the leading edge receptivity problem, linear growth and the nonlinear breakdown stage', *Mathematika* **37**(2), 151–189. (Cited on pages 18 & 20).

Hall, P. & Horseman, N. J. (1991), 'The linear inviscid secondary instability of longitudinal vortex structures in boundary layers', *Journal of Fluid Mechanics* **232**, 357–375. (Cited on page 28).

Han, L. S. & Cox, W. (1982), A visual study of turbine blade pressure-side boundary layers, *in* 'ASME 1982 International Gas Turbine Conference and Exhibit', American Society of Mechanical Engineers. (Cited on pages 2 & 15).

Herbert, T. (1988), 'Secondary instability of boundary layers', *Annual review of fluid mechanics* **20**(1), 487–526. (Cited on page 12).

Hoffmann, P., Muck, K. & Bradshaw, P. (1985), 'The effect of concave surface curvature on turbulent boundary layers', *Journal of Fluid mechanics* **161**, 371–403. (Cited on page 35).

Hopfinger, E. J., Kurniawan, A., Graf, W. & Lemmin, U. (2004), 'Sediment erosion by Görtler vortices: the scour-hole problem', *Journal of Fluid Mechanics* **520**, 327–342. (Cited on page 2).

Ito, A. (1980), 'The generation and breakdown of longitudinal vortices along a concave wall', *J. Japan Soc. Aero. Space Sci* **28**, 327–333. (Cited on page 25).

Ito, A. (1987), Visualization of boundary layer transition along a concave wall, *in* 'Flow Visualization IV', pp. 339–344. (Cited on page 25).

Jacobs, R. & Durbin, P. (2001), 'Simulations of bypass transition', *Journal of Fluid Mechanics* **428**, 185–212. (Cited on page 12).

Jeans, A. H. & Johnston, J. (1983), The effects of concave curvature on turbulent boundary layer structure, *in* 'Structure of Complex Turbulent Shear Flow', Springer, pp. 89–99. (Cited on page 34).

Jeong, J. & Hussain, F. (1995), 'On the identification of a vortex', *Journal of fluid mechanics* **285**, 69–94. (Cited on page 74).

Kahawita, R. (1975), 'Instability of laminar wall jets along curved surfaces', *AIAA Journal* **13**(11), 1517–1518. (Cited on page 18).

Kamotani, Y., Lin, J. & Ostrach, S. (1985), 'Effect of destabilizing heating on Görtler vortices', *Journal of heat transfer* **107**(4), 877–882. (Cited on page 37).

Kieffer, S. W. & Sturtevant, B. (1988), 'Erosional furrows formed during the lateral blast at Mount St. Helens, May 18, 1980', *Journal of Geophysical Research: Solid Earth* **93**(B12), 14793–14816. (Cited on page 2).

Kim, J., Moin, P. & Moser, R. (1987), 'Turbulence statistics in fully developed channel flow at low Reynolds number', *Journal of fluid mechanics* **177**, 133–166. (Cited on page 53).

Klebanoff, P. S., Tidstrom, K. & Sargent, L. (1962), 'The three-dimensional nature of boundary-layer instability', *Journal of Fluid Mechanics* **12**(1), 1–34. (Cited on page 12).

Kottke, V. (1988), On the instability of laminar boundary layers along concave walls towards Görtler vortices, *in* 'Propagation in Systems Far from Equilibrium', Springer, pp. 390–398. (Cited on pages 23 & 24).

Le Cunff, C. & Zebib, A. (1996), 'Nonlinear spatially developing Görtler vortices in curved wall jet flow', *Physics of Fluids* **8**(9), 2375–2384. (Cited on page 18).

Lee, J., Jung, S. Y., Sung, H. J. & Zaki, T. A. (2013), 'Effect of wall heating on turbulent boundary layers with temperature-dependent viscosity', *Journal of Fluid Mechanics* **726**, 196–225. (Cited on page 117).

Lee, K. & Liu, J. T. (1992), 'On the growth of mushroomlike structures in nonlinear spatially developing Goertler vortex flow', *Physics of Fluids A: Fluid Dynamics* **4**(1), 95–103. (Cited on pages 25, 67 & 115).

Lenaers, P., Li, Q., Brethouwer, G., Schlatter, P. & Örlü, R. (2012), 'Rare backflow and extreme wall-normal velocity fluctuations in near-wall turbulence', *Physics of fluids* **24**(3), 035110. (Cited on pages xiii, 54 & 55).

Li, F. & Malik, M. R. (1995), 'Fundamental and subharmonic secondary instabilities of Görtler vortices', *Journal of Fluid Mechanics* **297**, 77–100. (Cited on pages 29, 74 & 84).

Liu, J. (2007), 'An extended Reynolds analogy for excited wavy instabilities of developing streamwise vortices with applications to scalar mixing intensification', *Proceedings of the Royal Society A: Mathematical, Physical and Engineering Sciences* **463**(2083), 1791–1813. (Cited on pages 37, 106 & 107).

Liu, J. (2008), 'Nonlinear instability of developing streamwise vortices with applications to boundary layer heat transfer intensification through an extended Reynolds analogy', *Philosophical Transactions of the Royal Society A: Mathematical, Physical and Engineering Sciences* **366**(1876), 2699–2716. (Cited on pages 37, 106 & 107).

Liu, J. & Sabry, A. (1991), 'Concentration and heat transfer in nonlinear Gortler vortex flow and the analogy with longitudinal momentum transfer', *Proceedings of the Royal Society of London. Series A: Mathematical and Physical Sciences* **432**(1884), 1–12. (Cited on pages 37 & 106).

Liu, J. T. & Lee, K. (1995), 'Heat transfer in a strongly nonlinear spatially developing longitudinal vorticity system', *Physics of Fluids* **7**(3), 559–599. (Cited on pages 37, 97, 98, 108 & 115).

Liu, W. & Domaradzki, J. A. (1993), 'Direct numerical simulation of transition to turbulence in Görtler flow', *Journal of Fluid Mechanics* **246**, 267–299. (Cited on page 32).

Luchini, P. & Bottaro, A. (1998), 'Görtler vortices: a backward-in-time approach to the receptivity problem', *Journal of Fluid Mechanics* **363**, 1–23. (Cited on page 23).

Lueptow, R. (2009), 'Taylor-couette flow', *Scholarpedia* **4**(11), 6389. (Cited on pages xii & 17).

Lund, T. S. & Moin, P. (1996), 'Large-eddy simulation of a concave wall boundary layer', *International journal of heat and fluid flow* **17**(3), 290–295. (Cited on page 36).

Maday, Y. & Patera, A. T. (1989), Spectral element methods for the incompressible Navier-Stokes equations, *in* 'State-of-the-art surveys on computational mechanics (A90-47176 21-64). New York, American Society of Mechanical Engineers, 1989, p. 71-143. Research supported by DARPA.', pp. 71–143. (Cited on page 43).

Malatesta, V., Souza, L. F. d. & Liu, J. T. (2013), 'Influence of Görtler vortices spanwise wavelength on heat transfer rates', *Computational Thermal Sciences: An International Journal* **5**(5). (Cited on pages 33, 38 & 107).

Malatesta, V., Souza, L. F., Liu, J. T. & Kloker, M. J. (2015), 'Heat transfer analysis in a flow over concave wall with primary and secondary instabilities', *Procedia IUTAM* **14**, 487–495. (Cited on pages 33, 38 & 107).

Mangalam, S., Dagenhart, J. & Kalburgi, V. (1987), Influence of suction and curvature on the growth of Görtler vortices on an airfoil, *in* '25th AIAA Aerospace Sciences Meeting', p. 481. (Cited on page 13).

Mangalam, S., Dagenhart, J., Meyers, J. & Hepner, T. (1985), The Görtler instability on an airfoil, *in* '23rd Aerospace Sciences Meeting', p. 491. (Cited on pages xii, 2, 13, 15 & 21).

Matsson, O. J. E. (1998), 'Görtler vortices in wall jet flow on a rotating cylinder', *Physics of Fluids* **10**(9), 2238–2248. (Cited on pages 18 & 117).

McCormack, P. D., Welker, H. & Kelleher, M. (1970), 'Taylor-Görtler vortices and their effect on heat transfer', *Journal of Heat Transfer* **92**(1), 101–112. (Cited on pages 2 & 37).

Meksyn, D. (1950), 'Stability of viscous flow over concave cylindrical surfaces', *Proceedings of the Royal Society of London. Series A. Mathematical and Physical Sciences* **203**(1073), 253–265. (Cited on pages 84 & 113).

Méndez, M., Shadloo, M. S. & Hadjadj, A. (2020), 'Heat-transfer analysis of a transitional boundary layer over a concave surface with Görtler vortices by means of direct numerical simulation', *Physics of Fluids* (Accepted with minor revision). (Cited on page 91).

Méndez, M., Shadloo, M. S., Hadjadj, A. & Ducoin, A. (2018), 'Boundary layer transition over a concave surface caused by centrifugal instabilities', *Computers & Fluids* **171**, 135–153. (Cited on pages xvi, 40, 65, 93, 106, 107, 108, 109, 110 & 111).

Meroney, R. & Bradshaw, P. (1975), 'Turbulent boundary-layer growth over a longitudinally curved surface', *AIAA Journal* **13**(11), 1448–1453. (Cited on page 35).

Mitsudharmadi, H., Winoto, S. & Shah, D. (2004), 'Development of boundary-layer flow in the presence of forced wavelength Görtler vortices', *Physics of Fluids* **16**(11), 3983–3996. (Cited on pages xii, 24, 26, 27 & 57).

Mitsudharmadi, H., Winoto, S. & Shah, D. (2005), 'Secondary instability in forced wavelength Görtler vortices', *Physics of Fluids* **17**(7), 074104. (Cited on page 28).

Mohr, B. & Frings, W. (2010), 'Jülich Blue Gene/P extreme scaling workshop 2010'. (Cited on pages xiii & 42).

Momayez, L., Dupont, P., Delacourt, G., Lottin, O. & Peerhossaini, H. (2009), 'Genetic algorithm based correlations for heat transfer calculation on concave surfaces', *Applied Thermal Engineering* **29**(17-18), 3476–3481. (Cited on page 38).

Momayez, L., Dupont, P. & Peerhossaini, H. (2004*a*), 'Effects of vortex organization on heat transfer enhancement by Görtler instability', *International Journal of Thermal Sciences* **43**(8), 753–760. (Cited on page 38).

Momayez, L., Dupont, P. & Peerhossaini, H. (2004*b*), 'Some unexpected effects of wavelength and perturbation strength on heat transfer enhancement by görtler instability', *International Journal of Heat and Mass Transfer* **47**(17-18), 3783–3795. (Cited on page 38).

Morata, E. C., Gourdain, N., Duchaine, F. & Gicquel, L. (2012), 'Effects of free-stream turbulence on high pressure turbine blade heat transfer predicted by structured and unstructured LES', *International Journal of Heat and Mass Transfer* **55**(21-22), 5754–5768. (Cited on page 15).

Morkovin, M. (1994), 'Transition in open flow systems-a reassessment', *Bull. Am. Phys. Soc.* **39**, 1882. (Cited on pages xii & 9).

Morkovin, M. V. (1969), On the many faces of transition, *in* 'Viscous drag reduction', Springer, pp. 1–31. (Cited on page 9).

Morkovin, M. V. (1993), Bypass-transition research: issues and philosophy, *in* 'Instabilities and Turbulence in Engineering Flows', Springer, pp. 3–30. (Cited on page 10).

Moser, R. D., Kim, J. & Mansour, N. N. (1999), 'Direct numerical simulation of turbulent channel flow up to $Re_\tau = 590$', *Physics of fluids* **11**(4), 943–945. (Cited on pages xiii, 54 & 55).

Moser, R. D. & Moin, P. (1987), 'The effects of curvature in wall-bounded turbulent flows', *Journal of Fluid Mechanics* **175**, 479–510. (Cited on page 36).

Murdock, J. W. (1980), 'The generation of a Tollmien-Schlichting wave by a sound wave', *Proceedings of the Royal Society of London. A. Mathematical and Physical Sciences* **372**(1751), 517–534. (Cited on page 53).

Ohlsson, J., Schlatter, P., Mavriplis, C. & Henningson, D. S. (2011), The spectral-element and pseudo-spectral methods: A comparative study, *in* 'Spectral and High Order Methods for Partial Differential Equations', Springer, pp. 459–467. (Cited on page 55).

Patera, A. T. (1984), 'A spectral element method for fluid dynamics: laminar flow in a channel expansion', *Journal of computational Physics* **54**(3), 468–488. (Cited on page 43).

Peerhossaini, H. & Bahri, F. (1998), 'On the spectral distribution of the modes in nonlinear Görtler instability', *Experimental Thermal and Fluid Science* **16**(3), 195–208. (Cited on page 27).

Peerhossaini, H. & Wesfreid, J. (1988*a*), 'Les tourbillons de Görtler et leurs influence sur les turbines à gaz', *Bull Assoc. Tech. Maritime Aéronaut* **88**, 361–381. (Cited on page 2).

Peerhossaini, H. & Wesfreid, J. (1988*b*), 'On the inner structure of streamwise Görtler rolls', *International journal of heat and fluid flow* **9**(1), 12–18. (Cited on pages xii & 22).

Peerhossaini, H. & Wesfreid, J. E. (1988*c*), Experimental study of the Taylor-Görtler instability, *in* 'Propagation in Systems far from Equilibrium', Springer, pp. 399–412. (Cited on page 22).

Petitjeans, P., Peerhossaini, H. & Wesfreid, J. (1990), 'Nonlinear investigation of the Taylor-Görtler vortices', *Abstract in Coll. Görtler Vortex Flow, Euromech* **271**. (Cited on page 26).

Petitjeans, P. & Westfried, J.-E. (1996), 'Spatial evolution of Görtler instability in a curved duct of high curvature', *AIAA journal* **34**(9), 1793–1800. (Cited on page 17).

Pfenninger, W., Reed, H. L. & Dagenhart, J. (1980), 'Design considerations of advanced supercritical low drag suction airfoils'. (Cited on page 14).

Piquet, J. (2013), *Turbulent flows: models and physics*, Springer Science & Business Media. (Cited on page 34).

Pope, S. B. (2000), *Turbulent Flows*, Cambridge University Press. (Cited on pages 6, 7 & 8).

Prandtl, L. (1904), 'Über Flussigkeitsbewegung bei sehr kleiner Reibung', *Verhandl. III, Internat. Math.-Kong., Heidelberg, Teubner, Leipzig, 1904* pp. 484–491. (Cited on page 2).

Prandtl, L. (1925), '7. Bericht über Untersuchungen zur ausgebildeten Turbulenz', *ZAMM-Journal of Applied Mathematics and Mechanics/Zeitschrift für Angewandte Mathematik und Mechanik* **5**(2), 136–139. (Cited on page 6).

Prandtl, L. (1927), 'Über den Reibungswiderstand strömender Luft. Ergebnisse der Aerodynamischen Versuchsanstalt in Göttingen, iii. Lieferung, 1–5'. (Cited on page 7).

Rayleigh, L. (1917), 'On the dynamics of revolving fluids', *Proceedings of the Royal Society of London. Series A, Containing Papers of a Mathematical and Physical Character* **93**(648), 148–154. (Cited on pages 2 & 16).

Reed, H. L., Saric, W. S. & Arnal, D. (1996), 'Linear stability theory applied to boundary layers', *Annual review of fluid mechanics* **28**(1), 389–428. (Cited on page 9).

Reed, H. & Saric, W. (2008), Transition mechanisms for transport aircraft, *in* '38th Fluid Dynamics Conference and Exhibit', p. 3743. (Cited on page 14).

Reynolds, O. (1883), 'XXIX. An experimental investigation of the circumstances which determine whether the motion of water shall be direct or sinuous, and of the law of resistance in parallel channels', *Philosophical Transactions of the Royal society of London* (174), 935–982. (Cited on pages 3 & 8).

Roy, S. & Saha, U. K. (2013), 'Review on the numerical investigations into the design and development of Savonius wind rotors', *Renewable and Sustainable Energy Reviews* **24**, 73–83. (Cited on page 1).

Saric, W. S. (1994), 'Görtler vortices', *Annual Review of Fluid Mechanics* **26**(1), 379–409. (Cited on pages xii, 13, 18, 19, 72 & 73).

Saric, W. S., Reed, H. L. & Kerschen, E. J. (2002), 'Boundary-layer receptivity to freestream disturbances', *Annual review of fluid mechanics* **34**(1), 291–319. (Cited on pages 9 & 10).

Saric, W. & Thomas, A. (1984), Experiments on the subharmonic route to turbulence in boundary layers, *in* 'Turbulence and chaotic phenomena in fluids', pp. 117–122. (Cited on page 11).

Sayadi, T., Hamman, C. W. & Moin, P. (2013), 'Direct numerical simulation of complete H-type and K-type transitions with implications for the dynamics of turbulent boundary layers', *Journal of Fluid Mechanics* **724**, 480–509. (Cited on pages xii, 11 & 12).

Schlatter, P. & Örlü, R. (2010), 'Assessment of direct numerical simulation data of turbulent boundary layers', *Journal of Fluid Mechanics* **659**, 116–126. (Cited on pages xiii, xv, 54, 55, 88 & 89).

Schlatter, P., Örlü, R., Li, Q., Brethouwer, G., Fransson, J. H., Johansson, A. V., Alfredsson, P. H. & Henningson, D. S. (2009), 'Turbulent boundary layers up to Reθ= 2500 studied through simulation and experiment', *Physics of fluids* **21**(5), 051702. (Cited on pages xii, 6 & 7).

Schlichting, H. (1933), 'Zur enststehung der turbulenz bei der platenstromung nachr', *Ges. Wiss. Gottingen Math. Phys. Klasse* **182**. (Cited on page 11).

Schlichting, H. & Gersten, K. (2017), *Boundary-layer theory*, Springer. (Cited on pages 8 & 10).

Schrader, L.-U., Brandt, L., Mavriplis, C. & Henningson, D. S. (2010), 'Receptivity to free-stream vorticity of flow past a flat plate with elliptic leading edge', *Journal of Fluid Mechanics* **653**, 245–271. (Cited on page 53).

Schrader, L.-U., Brandt, L. & Zaki, T. A. (2011), 'Receptivity, instability and breakdown of Görtler flow', *Journal of Fluid Mechanics* **682**, 362–396. (Cited on pages xiv, 24, 32, 55, 57, 58, 59, 60, 61, 62, 63, 64, 77, 79, 80 & 113).

Schubauer, G. B. & Skramstad, H. K. (1948), Laminar-boundary-layer oscillations and transition on a flat plate, Technical report, National Aeronautics and Space Administration Washington DC. (Cited on page 11).

SEGOB (2013), 'DECRETO por el que se reforman y adicionan diversas disposiciones de la Constitución Política de los Estados Unidos Mexicanos, en Materia de Energía', *Diario Oficial de la Federación de México 20/12/2013* . (Cited on page 1).

Sescu, A. & Thompson, D. (2015), 'On the excitation of Görtler vortices by distributed roughness elements', *Theoretical and Computational Fluid Dynamics* **29**(1-2), 67–92. (Cited on page 24).

Shahriari, N., Bodony, D. J., Hanifi, A. & Henningson, D. S. (2016), 'Acoustic receptivity simulations of flow past a flat plate with elliptic leading edge', *Journal of Fluid Mechanics* **800**. (Cited on page 53).

Sharma, S. & Ducoin, A. (2018), 'Direct numerical simulation of the effect of inlet isotropic turbulence on centrifugal instabilities over a curved wall', *Computers & Fluids* **174**, 1–13. (Cited on pages 33 & 55).

Smith, A. (1955), 'On the growth of Taylor-Görtler vortices along highly concave walls', *Quarterly of Applied Mathematics* **13**(3), 233–262. (Cited on pages 84 & 113).

Souza, L. F. (2017), 'On the odd and even secondary instabilities of Görtler vortices', *Theoretical and Computational Fluid Dynamics* **31**(4), 405–425. (Cited on page 32).

Sprague, M., Churchfield, M., Purkayastha, A., Moriarty, P. & Lee, S. (2010), A comparison of Nek5000 and OpenFOAM for the DNS of turbulent channel flow, *in* 'Presentation at Nek5000 Users Meeting'. (Cited on pages xiii, 53 & 54).

Swearingen, J. D. & Blackwelder, R. F. (1987), 'The growth and breakdown of streamwise vortices in the presence of a wall', *Journal of Fluid Mechanics* **182**, 255–290. (Cited on pages 28, 30, 32, 73, 76, 77, 78, 79, 98 & 113).

Tandiono, T., Winoto, S. & Shah, D. (2013), 'Spanwise velocity component in nonlinear region of Görtler vortices', *Physics of Fluids* **25**(10), 104104. (Cited on pages 70 & 113).

Tandiono, Winoto, S. & Shah, D. (2008), 'On the linear and nonlinear development of Görtler vortices', *Physics of Fluids* **20**(9), 094103. (Cited on pages xii, 26, 27, 57, 74, 78 & 113).

Tandiono, Winoto & Shah, D. (2009), 'Wall shear stress in Görtler vortex boundary layer flow', *Physics of Fluids* **21**(8). (Cited on pages xii, 30, 31, 55, 57, 79 & 93).

Tani, I. (1962), 'Production of longitudinal vortices in the boundary layer along a concave wall', *Journal of Geophysical Research* **67**(8), 3075–3080. (Cited on page 21).

Tani, I. & Sakagami, J. (1962), Boundary-layer instability at subsonic speeds, *in* 'Proc. ICAS, Third Congress, Stockholm', pp. 391–403. (Cited on pages xii & 20).

Taylor, G. I. (1923), 'VIII. Stability of a viscous liquid contained between two rotating cylinders', *Philosophical Transactions of the Royal Society of London. Series A, Containing Papers of a Mathematical or Physical Character* **223**(605-615), 289–343. (Cited on page 17).

Toe, R., Ajakh, A. & Peerhossaini, H. (2002), 'Heat transfer enhancement by Görtler instability', *International journal of heat and fluid flow* **23**(2), 194–204. (Cited on pages 2 & 37).

Tollmien (1931), The production of turbulence, Technical report, National Advisory Committee for Aeronautics Langley Field VA Langley Aeronautical Laboratory. (Cited on page 11).

Tollmien, W. (1935), *Ein allgemeines Kriterium der Instabilität laminarer Geschwindigkeitsverteilungen*, Vandenhoeck & Ruprecht. (Cited on page 25).

Tufo, H. M. & Fischer, P. F. (1999), Terascale spectral element algorithms and implementations, *in* 'SC'99: Proceedings of the 1999 ACM/IEEE Conference on Supercomputing', IEEE, pp. 68–68. (Cited on page 43).

Turner, M. (2012), 'Tollmien–Schlichting wave amplitudes on a semi-infinite flat plate and a parabolic body: comparison of a parabolized stability equation method and direct numerical simulations', *Quarterly journal of mechanics and applied mathematics* **65**(2), 183–210. (Cited on page 53).

von Helmholtz, H. (1868), *über discontinuirliche Flüssigkeits-Bewegungen*, Akademie der Wissenschaften zu Berlin. (Cited on page 25).

von Kármán, T. (1930), 'Mechanische änlichkeit und turbulenz', *Nachrichten von der Gesellschaft der Wissenschaften zu Göttingen, Mathematisch-Physikalische Klasse* **1930**, 58–76. (Cited on page 7).

Wadey, P. (1992), 'On the development of Görtler vortices in wall jet flow', *Journal of engineering mathematics* **26**(2), 297–313. (Cited on page 18).

Wang, H., Goldstein, R. & Olson, S. (1999), 'Effect of high free-stream turbulence with large length scale on blade heat/mass transfer', *Journal of Turbomachinery* **121**(2), 217–224. (Cited on page 15).

Wang, H., Olson, S. & Goldstein, R. J. (2005), 'Development of Taylor-Görtler vortices over the pressure surface of a turbine blade', *Journal of heat transfer* **127**(5), 540–543. (Cited on pages 2 & 15).

White, E. & Ergin, F. G. (2003), Receptivity and transient growth of roughness-induced disturbances, *in* '33rd AIAA Fluid Dynamics Conference and Exhibit', p. 4243. (Cited on page 53).

White, F. M. (1991), *Viscous Fluid Flows*, McGraw-Hill Inc. (Cited on pages xii, 7, 8 & 10).

Winoto, S., Mitsudharmadi, H. & Shah, D. A. (2005), 'Visualizing Görtler vortices', *Journal of Visualization* **8**(4), 315–322. (Cited on pages xii, 24 & 25).

Wu, X. & Moin, P. (2009), 'Direct numerical simulation of turbulence in a nominally zero-pressure-gradient flat-plate boundary layer', *Journal of Fluid Mechanics* **630**, 5–41. (Cited on page 12).

Wu, X. & Moin, P. (2010), 'Transitional and turbulent boundary layer with heat transfer', *Physics of Fluids* **22**(8), 085105. (Cited on page 111).

Wu, X., Zhao, D. & Luo, J. (2011), 'Excitation of steady and unsteady Görtler vortices by free-stream vortical disturbances', *Journal of Fluid Mechanics* **682**, 66–100. (Cited on page 24).

Yu, X. & Liu, J. (1991), 'The secondary instability in Görtler flow', *Physics of Fluids A: Fluid Dynamics* **3**(8), 1845–1847. (Cited on pages 28 & 73).

Yu, X. & Liu, J. T. (1994), 'On the mechanism of sinuous and varicose modes in three-dimensional viscous secondary instability of nonlinear Görtler rolls', *Physics of Fluids* **6**(2), 736–750. (Cited on page 28).